ASME DISTRICT F EARLY CAREER TECHNICAL JOURNAL

Volume 8

ASME District F
Early Career Technical Conference (ECTC)
University of Alabama
Tuscaloosa, Alabama, USA
October 2-3, 2009

ASME District F encompasses the states of Alabama, Delaware, District of Columbia, Florida, Georgia, Maryland, Mississippi, North Carolina, South Carolina, Tennessee and Virginia. For more information go to http://districts.asme.org/DistrictF.htm.

ISBN 978-1-4507-9221-9

ASME EARLY CAREER TECHNICAL JOURNAL

Volume 8, Number 1

Presented at
ASME Early Career Technical Conference
Tuscaloosa, Alabama
October 2-3, 2009

Sponsored by

The ASME Old Guard
University of Alabama
HOLTEC International
Unified Brands
Florida International University
Mississippi Section
Birmingham Section
ASME District F

Editor and Chair of Technical Committee
Dr. Robert P. Taylor

Chair of Coordinating Committee
Dr. K. R. Rao

For more information about ECTC 2009 visit: http://districts.asme.org/DISTRICTF/ECTC/2009ECTC/

THE AMERICAN SOCIETY OF MECHANCIAL ENGINEERS SOUTHEAST DISTRICT F
THREE PARK AVENUE, NEW YORK, NY 10016

ASME ECTC 2009: ASME Early Career Technical Conference
October 2-3, 2009 Tuscaloosa, Alabama
The Ninth Annual Technical Conference
Sponsored by UA, FIU, ASME Old Guard, ASME Mississippi and Birmingham Sections and ASME District F
http://districts.asme.org/DISTRICTF/ECTC/2009ECTC/

The ASME Early Career Technical Conference Coordinating Committee and Technical Journal Editorial Board Express their Gratitude for the Continuing Grant Support to

THE ASME OLD GUARD

For the 'HONORARIUMS' awarded to the ECTC Conference Presenters during the past several years as well as for the 2009 ECTC Conference.

The ASME Early Career Technical Conference Coordinating Committee and Technical Journal Editorial Board Express their Appreciation to the Following Sponsors for Supporting ECTC 2009:

FOREWORD
Journal of ASME Early Career Technical Conference
October 2nd – 3rd, 2009

One of the primary objectives of American Society of Mechanical Engineers (ASME) is the dissemination of technical information. Pursuant to this goal of ASME Southeastern Region (Region XI) had initiated the Technical Conference (RTC) that was in fact in the earlier years the Graduate Technical Conferences when Dr. Lee Durbetaki was the Vice President of Region XI. In 2001 Regional Vice President Dr. K. R. Rao had with the help of Region XI Operating Board approved the creation of the Region XI Technical Conference (RTC).

The first RTC was held on April 6, 2002, in Jackson Mississippi with the participation of students across all five states (Florida, Georgia, Alabama, Tennessee and Mississippi) of the former ASME Region XI. The quality of the reviewed papers, published in the four volumes of the Regional Technical Journal from 2002 through 2006 called for this Conference to be renamed in 2006 the Conference as the Early Career Technical Conference (ECTC) indicating the changing demands of the times. On October 6 and 7, 2007 ECTC was held, in Jackson, MS with a robust support of Entergy Operations. Inc.

In 2007, for the first time, ECTC was held in a University, Florida International University (FIU), in Miami, Florida. Invitations were extended to seventy eight universities and companies comprising of fourteen states to participate in this conference. These included the states within the ASME International Southeast District F - Alabama, Delaware, District of Columbia, Florida, Georgia, Maryland, Mississippi, North Carolina, South Carolina, Tennessee, Virginia. In addition ECTC extended invitations to Louisiana, Arkansas and Texas of the ASME International Southwest Rocky Mountain District E. ECTC 2008 was also held at FIU, Florida with invitations being extended to all of the Universities invited for ECTC 2007. Dr. Yong Tao was the Chair, Technical Committee and Editor for ECTC 2007 and Dr. Sabri Tosunoglu for ECTC 2008. The generous financial support of ASME Old Guard funded the registration and even offset a part of their commutation expenses of the paper presenters to attend these conferences.

The success of the preceding ASME District F Early Career Technical Conferences prompted the organizers to look beyond the frontiers of the District. For the current ECTC 2009 invitations had been sent to *all of the universities affiliated with all of the ASME Districts A to J, that were even beyond USA.* It is gratifying to mention that we reached the cap of 35 paper presenter entries that we targeted. Of these we have 14 submittals from outside USA. Thus, the theme for this Conference we had *"ECTC 2009 Opens the Window to Outside USA"* had been amply demonstrated!

The Editor of the ECTC 2009 Journal established an elaborate review process similar to the process used by ASME Technical Divisions. Papers were distributed to Associate Editors of the Editorial Board based on their areas of expertise and they obtained three reviews for each paper by expert reviewers in the field. Once again this year, the Editorial Board made a significant effort to ensure the review process for each paper followed the criteria and deadlines so that this Journal could be published prior to the conference. Because of this rigorous requirement, the papers submitted were accepted as either for presentation only at the conference, or for both presentation and journal publication. Authors whose papers were rated acceptable for publication in the Technical Journal were required to make corrections and enhancements, based on reviewers' comments.

This journal is a compilation of thirty five (35) accepted technical papers from USA, Europe and Asia, presented at the ECTC 2009.

Robert P. Taylor, Ph.D., Fellow ASME
Editor, Early Career Technical Journal
Chair, ECTC Technical Committee

K. R. Rao, Ph. D., PE., Fellow ASME, FIE, CE
Chair
ECTC Coordinating Committee

ACKNOWLEDGEMENTS
ASME Early Career Technical Journal
October, 2009

Many individuals contributed to the success of this Early Career Technical Conference and this ECTC 2009 Journal.

The Coordinating Committee express gratitude and appreciation to Dr. K R. Rao, Chair of the Conference Coordinating Committee, and Dr. Robert P. Taylor, Editor of the Technical Journal and Chair of Technical Committee for their tireless and dedicated efforts in organizing the conference, directing the review process and overseeing the presentations. Their hard work has made this journal possible. In addition we thank all the members of the Editorial Board and invited reviewers, who spent countless hours of their own time reviewing and critiquing the papers to ensure a quality publication.

ECTC 2009 Journal Editorial Board comprises of the Editor, Robert P. Taylor, Co-Editors Yong X. Tao, Sabri Tosunoglu and Dr. Joseph Rencis (MEDH, University of Arkansas). The advice and guidance of Dr. Yong for ECTC 2009 is much appreciated. Dr. Tosunoglu was the web master for ASME ECTC 2009, whose help is very much recognized.

Unlike the previous years ECTC 2009 has separate tiers of Associate Editors from the Faculty and from the Professionals. The Associate Editors from Faculty are Dr. P. Raju Mantena, Dr. Beth Todd, Dr. Bob Pitz, Dr. Autar Kaw, Dr. Ram A. Goel, Dr. Shuh Jing (Ben) Ying, Dr. Zhanke Liu, Dr. Yuebin Guo. Associate Editors from Professionals are Dr. Lee Durbetaki, Richard Bunce, Bryan Eldridge, Lee Crawford , Dr. Gerald Jones, Dr. D. Sriram, William Adkins, Brian C. Gray, Dr. Ming Feng, Deepak Negandhi, and William Long. The associated editors took upon the responsibility of not only reviewing by themselves and often due to the large number of submittals recruiting credible and competent reviewers.

All of the names, contact details, bios and pictures of each of the above reviewers are posted on the ASME ECTC website http://districts.asme.org/DISTRICTF/ECTC/2009ECTC/. ASME District F ECTC Editorial Board and the Coordinating Committee thank each of the above reviewers for assuring a high standard of papers are accepted for presentation at the conference publication in this journal.

ASME District F and the Coordinating Committee congratulate all of the authors who demonstrated a high degree of professionalism in producing an excellent collection of papers.

ASME District F and the Coordinating Committee thank ASME staff, Burt Dicht Managing Director and his staff for the administrative support to the success of the conference and the publication of this journal.

Finally, we owe our gratitude to our principal sponsors to the ASME Old Guard, HOLTEC International, Unified Brands, University of Alabama, ASME MS and Birmingham Sections for their monetary contributions and Faculty Support to University of Alabama and Florida International University. Our thanks are to Dr. Lee Durbetaki, Dr. K. P. Singh and Mr.Eric Walzer who helped arrange significant contributions from the ASME Old Guard, HOLTEC International and Unified Brands respectively.

Once again we thank Dr. Robert P. Taylor, Head of Mechanical Engineering at University of Alabama for the steering through this ASME ECTC 2009.

-- 2009 ASME ECTC Coordinating Committee

Table of Contents

ASME Early Career Technical Journal
2009 ASME Early Career Technical Conference, ASME ECTC
October 2-3, 2009, Tuscaloosa, Alabama, USA

A STEREO-VIDEOGRAMMETRY SYSTEM FOR MONITORING WIND TURBINE BLADE SURFACES DURING STRUCTURAL TESTING

Jay T. Johnson
Georgia Institute of Technology
Atlanta, GA, USA

Scott Hughes, Jeroen van Dam
National Renewable Energy Laboratory
Golden, CO, USA

ABSTRACT

The National Renewable Energy Laboratory (NREL) implements a number of nondestructive evaluation (NDE) and structural health monitoring (SHM) techniques during static and fatigue wind turbine blade tests to monitor the time, location, and mode of damage to the blade. However, in the laboratory blade failure is often the result of the low pressure surface buckling, which is rarely measured with the current instrumentation and only quantified by visual observations. NREL desired an advanced NDE method to evaluate the out-of-plane surface deflections of a wind turbine blade during laboratory testing to make more accurate assessments of the blade performance under test. As a result, a stereo-videogrammetry system was developed to measure the airfoil shape and blade surface motion during static and fatigue testing. The topography can be used to (a) indicate the onset of buckling in static and fatigue tests, (b) measure blade damage by quantifying out-of-plane skin deformations, (c) point toward areas of weakness in the blade design, (d) capture real-time reductions in aerodynamic blade performance, (e) measure the twist-bend coupled characteristics of the blade, and (f) supply a means to compare blade simulations and finite element models to the as-built design.

INTRODUCTION

There have been a number of nondestructive evaluation (NDE) and Structural Health Monitoring (SHM) techniques developed to examine the health of the wind turbine blades during static and fatigue testing. Strain gages, piezoelectric actuators with force sensors, photoelastic panels, impedance-based SHM systems, acoustic emission sensors, and low-frequency accelerometers have been utilized in the past [1-3]. These NDE measurements correlate their signals to the decay of the structural health of the blade, but they have difficulty determining the mode of failure.

It is common in static and fatigue tests for blades to fail due to strain from out-of-plane deformations or buckling of the low pressure (LP) panel [4-5]. Plastic deformation of blade panels during testing is a metric which can be used to determine if a blade has failed a test. Commonly used NDE or SHM instrumentation is often inadequate to quantify out-of-plane deformations of the blade skin and, therefore, incapable of monitoring the presence of plastic behavior. To addresses this gap in testing instrumentation, a stereo-videogrammetry system has been designed at the NREL's National Wind Technology Center (NWTC) to measure the surface topography of wind turbine blades during static and fatigue testing. The primary goal of this work was to create a tool to identify the onset of blade buckling, quantify the out-of-plane deflections, and predict if buckling would lead to the failure of the blade.

Additionally, knowledge of the skin behavior and airfoil shape for different loading conditions can provide a range of performance data. By using the deformed airfoil geometry, the aerodynamic performance for different wind speeds can be calculated. The surface geometry and rotation can be used to compare the as-built design to blade aerodynamic and stress simulations as well as measure the twist-bend coupled behavior of the blade, which further factors into the aerodynamics of the blade [5-6].

In order to measure the blade geometry with a non-contact, nondestructive technique, optical and laser methods were investigated. These included laser doppler vibrometry, shearography, holography, interferometry, machine vision with structured light, moiré projection, videogrammetry, shape-from-shading, and shape-from-focus systems. Using cost, system lead time, precision, reliability and ease-of-use as evaluation criteria, videogrammetry was selected as the preferred technology, since a prototype system could be built with off-the-self cameras and a projector, and the software for analyzing the images was readily available, inexpensive and intuitive. The videogrammetry system also lends itself to large out-of-plane surface displacements which were prohibitive for other methods. Futhermore, Clarke et. al have shown that photogrammetry provides greater precision than moiré projection and optical triangulation for turbine blades [7].

Photogrammetry is a method of taking geometric measurements of objects using video images captured from cameras at different points of view. This is done by triangulating the location of target points on the object by calculating the intersection of projected epipolar lines-of-sight defined by each of the images (see the mathematical deviation in [8]). Stereo-videogrammetry uses two video cameras and applies photogrammetric principles to the synchronized series of images to produce the three-dimensional time series of the targets. Videogrammetry has often been used to monitor dynamic deformable bodies when time scales are small or if capturing images of the object from different angles with a single camera is impractical.

NASA Langley developed digital videogrammetry tools for five of NASA's wind-tunnels to observe aircraft wing and fuselage deflections [8-9]. The videogrammetric deformation measurements calculated the aircraft attitude and determined static and dynamic aeroelastic deflections. This same wind-tunnel technique has been used to observe helicopter rotor blade deflection and twist using reflective markers and synchronized strobe lighting [10].

When it was difficult to paint or place reflective markers on the structure, NASA implemented a technique of projecting dots onto surfaces to create the markers for the photogrammetry system. This setup is used to measure gossamer space structures such as ultra light or inflatable structures, e.g., membrane reflectors, solar sails, or solar arrays [11-12]. Using projected targets also allowed for less preparation time, quick adjustments in the target type and spacing, and it did not interfere with the motion, deformation, or shape of the subject.

There has been limited research into videogrammetry techniques for monitoring wind turbine testing or field operation. Sabel used a two-camera videogrammetry system to measure flap and lead-lag modes, eigenfrequencies, teeter motion, and tower sway of a two-bladed, 10-m turbine [13]. Eight retro-reflective markers were placed on wind turbine blades, one marker was placed on the tower to identify the target locations, and the system was imaged with cameras located 20 m from the turbine.

Robson and Setan experimented with using photogrammetry to measure the deflections of wind turbine blades during structural testing [14]. They used six multiplexed cameras to measure a 21 m wind turbine blade undergoing static loading to verify the design stress distribution. 30 retro-reflective markers were placed on the trailing edge of the blade near the root, which had been spray painted black to reduce glare and improve marker visibility. The authors note that the largest error in marker RMS location was 180 μm, which corresponded to an objective space precision of 1:20,000.

This paper describes the prototype NREL videogrammetry system. First the videogrammetry apparatus and hardware setup is discussed, followed by a discussion on the triangulation software and the three-dimensional point cloud data reduction analysis. Finally, results from the implementation of the system on an 8.3 m wind turbine blade undergoing static and fatigue testing are presented.

SYSTEM CONFIGURATION

The basic videogrammetry setup, depicted in Figure 1, consisted of a digital projector and two cameras mounted at different viewing angles. The projector generated the markers on the low pressure side of the wind turbine blade, while the cameras captured the images of the blade motion.

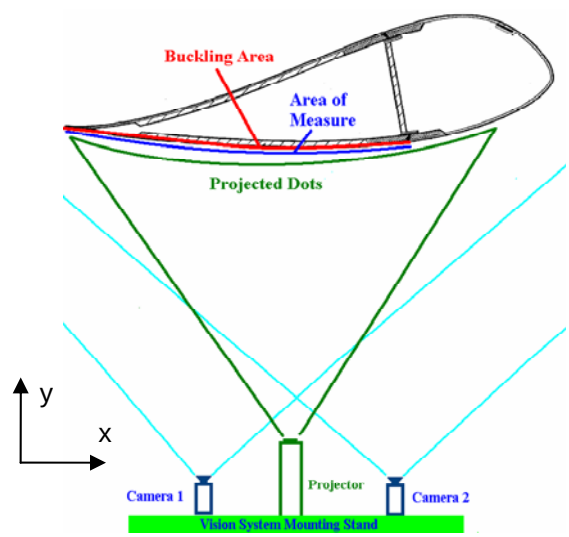

Figure 1. Videogrammetry system setup.

The cameras were Point Grey Research 1600x1200 pixel Grasshopper IEEE-1394b digital cameras with 16 mm lenses. The cameras were mounted on tripods and connected to the data acquisition computer with a dual bus firewire PCI Express card. In order to get accurate videogrammetry data the cameras were synchronized with Point Grey Research MultiSync software so that they would trigger at the same time.

A computer with Windows XP was used to record the images for later processing as well as send the image signal to the projector. The computer was configured with a dual monitor DVI output so that the projector displayed the extended desktop. Microsoft PowerPoint slides with different densities of markers were then displayed through the projector to get the correct grid spacing and size. The targets were typically coded with a binary ring, shown in Figure 2, so the videogrammetry software, PhotoModeler 6, could uniquely identify the

points in each of the images. A millisecond timer was also added to the corner of the projection monitor in order to match up the synchronized images for processing.

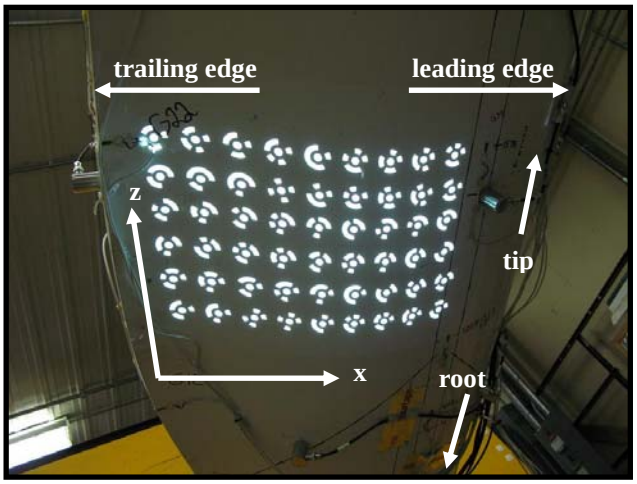

Figure 2. Projected coded targets on the high pressure side of the blade.

SYSTEM OPERATION

To run the system and process the raw data, there were a number of steps requiring different hardware and software tools. First, the camera was calibrated in order to extract accurate geometric information from the images. All cameras distort the images they take due to lens optics, so to correct for this, each camera took a series of 12 images of a 36”x36” calibration grid to determine the 10 camera parameters, including focal length, principle point, format height and width, and radial and decentering distortion coefficients. These parameters were determined in PhotoModeler with images captured from the four sides of the calibration grid, shown in Figure 3, at camera orientations of -90º, 0º, and 90º with respect to the optical axis.

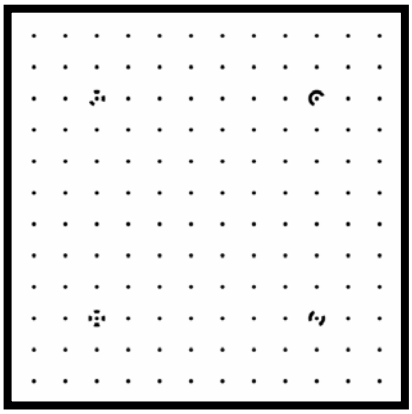

Figure 3. Calibration grid with four coded targets.

Second, the system was setup depending on the blade and the type of test. The cameras and projector were placed to gather topographical information from the area of interest on the blade. This location was generally where the largest out-of-plane motion was expected and was determined from simulations or past experience testing similar blades.

Third, the projector was turned on and setup with the correct target grid, the cameras were synchronized, and images were captured and recorded to the hard drive using Point Grey Research FlyCapture software. The aperture and frame rate were also adjusted to provide the correct contrast in the images and decrease the time between successive, synchronized image pairs. Each pair of images form an epoch, or snapshot of the target points at a specific time. In the experimental work at NWTC, it was unnecessary to turn off or dim the lighting because the projector was bright enough to provide contrast between the targets and the background, however in some situations it may be advisable to change the ambient lighting.

Fourth, the images were processed in Eos System’s PhotoModeler 6. The images were imported as epochs (frames) into PhotoModeler, where the targets were found and referenced (paired up) to create 3-D data, shown in Figure 4. The software tracked the targets through the epochs so the 3-D path of each point was calculated. At this time, the scale and axes were defined using physical intra-target measurements on the blade.

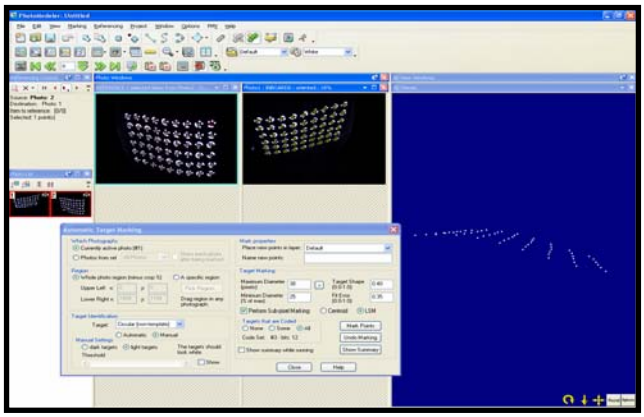

Figure 4. PhotoModeler with referenced coded targets in two images and the resulting 3D representation on the right.

Fifth, MATLAB codes developed at NREL were used to visualize and quantify blade motions using the 3-D point data exported from PhotoModeler. In static tests, the data was inspected directly for buckling characteristics whereas in fatigue tests, the data was compared to previous videogrammetry results of the same blade to monitor changes in out-of-plane deformations over the

life of the test. These changes in blade shape can indicate degradation in blade health and the onset of plastic buckling.

DATA PROCESSING

The data exported from PhotoModeler contained the time-series of each target in the point cloud in a global coordinate system. This cloud represented the surface of the blade as it moved through space, shown in Figure 5, so to measure the relative motion of the surface points, a new non-inertial reference coordinate system was created to negate the motion of the blade as a whole.

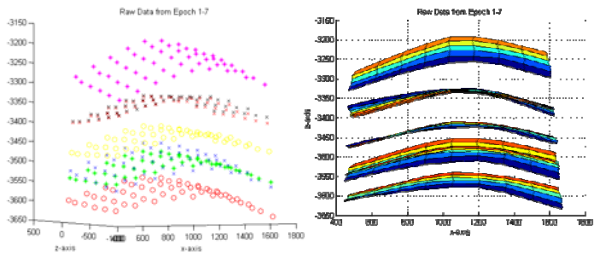

Figure 5. The point cloud displayed as points and surfaces for 6 epochs.

This coordinate system was difficult to construct using the point cloud because each point moved independently based on motion and deformation of the blade. Additionally, the projected targets were constrained to the line-of-sight of the projector and the blade was cantilevered during testing, so the data—and therefore the reference frame—translated and rotated through space. This was evident when each epoch had the center of the point cloud placed at the origin of the new reference frame and the maximum and minimum marker positions were connected, as shown in Figure 6. The twist and flap of the blade were also clearly visible in the motion between epochs, shown in Figure 7. The periphery markers move the most because blade flap and twist. A diagram of the desired coordinate system and the blade twist and flap motions are shown in Figure 8.

To convert the inertial PhotoModeler data into a common coordinate frame attached to the blade, rotational and translational transformation techniques were devised. One concept was to use a least-squares-fit plane through the targets along the tail edge and the spar cap to act as the new reference frame, as these locations were more rigid and less prone to deform. The other options were to take the centroid of the points for each epoch and place them at the origin, shown in Figure 9, and then use one of the following methods of data normalization:

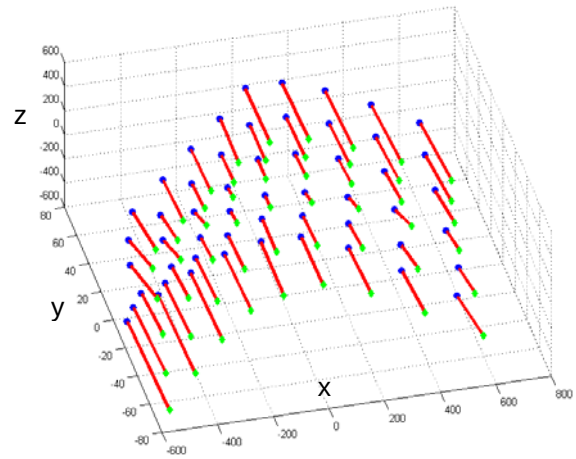

Figure 6. The maximum and minimum locations of the cloud after centering the epoch at the origin.

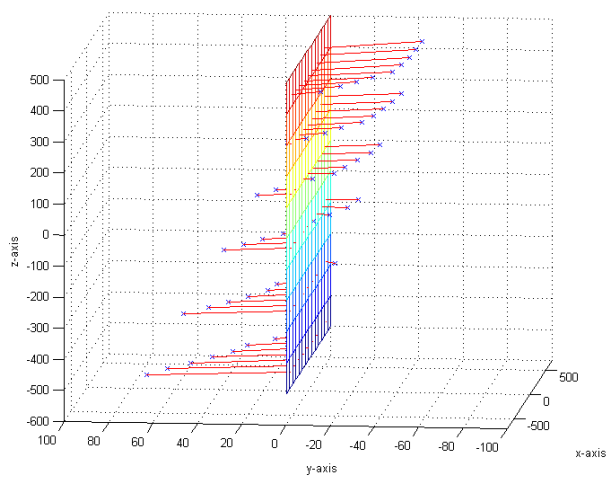

Figure 7. The motion of the data points between epochs. This shows the blade flap and twist.

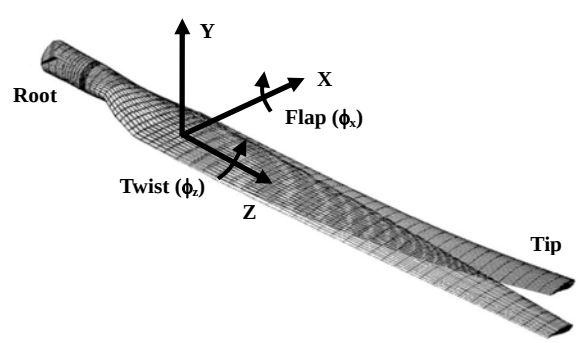

Figure 8. The coordinate system attached to the blade with the twist and flap rotations labeled.

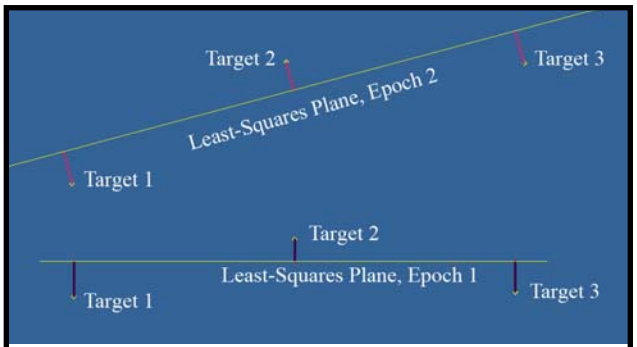

(a) Data from 2 epochs in the global coordinate system.

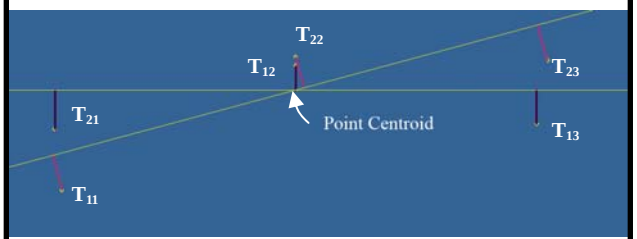

(b) New coordinate system with the centroid of point cloud for each epoch at the origin.

Figure 9. Two dimensional example of adjusting the epochs to contain the same centroid. T_{21} indicates target 1 in epoch 2.

1. **Rotation Method**: rotate the least-squares (LS) planes for all the epochs to be coplanar, shown in Figure 10. This method would be especially useful if the targets were rigidly attached or painted on the structure.
2. **Projection Method 1**: subtract the distance between the planes represented as a vector *normal to the first epoch LS plane* that passes through the target point, shown in Figure 11.
3. **Projection Method 2**: subtract the distance between the target and the LS plane from the point created from projecting the target onto the first epoch plane, shown in Figure 12.

For all of the cases the LS plane was created for each epoch and the point locations were transformed into the new coordinate system by placing the center of the point cloud at the origin. The centroid of the point cloud was calculated by

$$\mathbf{x}_c = \frac{1}{p}\sum_{i=1}^{p}\mathbf{x}_i \tag{1}$$

where $\mathbf{x}_i = [x_i, y_i, z_i]^T$ was point *i* from PhotoModeler and *p* was the number of points. The least squares plane, $Ax+By+CZ+D = 0$, is found by minimizing the sum of the squares of the distance between the points and the plane, defined by the function

$$f\left(A,B,C,D\right) = \sum_{i=1}^{p}\left(Ax_i + By_i + Cz_i - D\right)^2 \tag{2}$$

Therefore, for the rotation method of data normalization, all points for all epochs were transformed by the affine coordinate transformation

$$\begin{bmatrix} x_i' \\ y_i' \\ z_i' \\ 1 \end{bmatrix} = \mathbf{R_x}\mathbf{R_z}\mathbf{T}_c \begin{bmatrix} x_i \\ y_i \\ z_i \\ 1 \end{bmatrix} \tag{3}$$

where $[R_x]$ and $[R_z]$ are the rotation matrices about the *x*- and *z*-axes, which orient the LS plane coplanar with the *xz*-plane, and $[T_c]$ is the translation matrix which brings the centroid of the epoch data to the origin. These matrices take the form

$$\mathbf{R_x} = \begin{bmatrix} 1 & 0 & 0 & 0 \\ 0 & \cos\phi_x & -\sin\phi_x & 0 \\ 0 & \sin\phi_x & \cos\phi_x & 0 \\ 0 & 0 & 0 & 1 \end{bmatrix} \tag{4}$$

$$\mathbf{R_z} = \begin{bmatrix} \cos\phi_z & -\sin\phi_z & 0 & 0 \\ \sin\phi_z & {}_x\cos\phi_z & 0 & 0 \\ 0 & 0 & 1 & 0 \\ 0 & 0 & 0 & 1 \end{bmatrix} \tag{5}$$

$$\mathbf{T_c} = \begin{bmatrix} 1 & 0 & 0 & -x_c \\ 0 & 1 & 0 & -y_c \\ 0 & 0 & 1 & -z_c \\ 0 & 0 & 0 & 1 \end{bmatrix} \tag{6}$$

where ϕ_x and ϕ_z are the rotation angles around the *x*- and *z*-axes. For computational convenience in the projection methods, all the epochs were rotated so that the LS plane in the first epoch was coincident with *xz*-plane.

There are merits to each of these normalization schemes so it was not always clear which method should be executed. If the targets were attached to the blade, the rotation method would be preferred because the points will be approximately the same distance apart on the

surface of the blade as it rotated. However, since the NWTC videogrammetry setup used projected targets, the projection methods reduced the spatial expansion error, seen in Figure 10. This error is created when the surface rotates and decreases its projected frontal area but the area formed by the lines-of-sight for the targets remains the same. As a result, when the targets are rotated to be compared with the other epochs, the point cloud appears to have expanded on the surface.

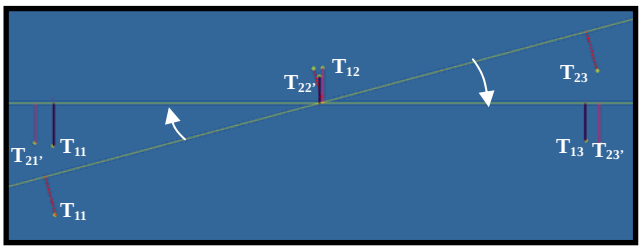

Figure 10. Rotating the LS planes to be coplanar, shown with the original and the new data points for epoch 2. New points are indicated with a prime (') in the subscript.

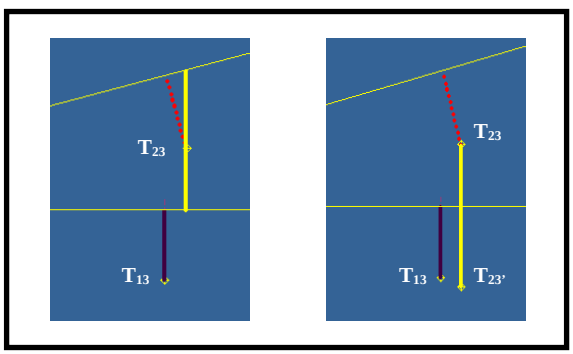

Figure 11. Data normalization using projection method 1. The yellow line is the distance between the planes normal to the LS plane in epoch 1 through T_{23}.

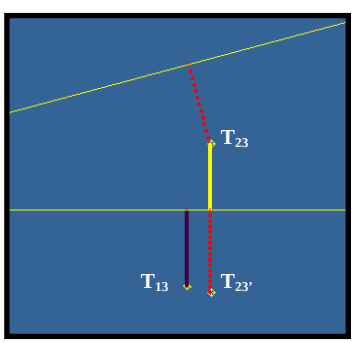

Figure 12. Data normalization using projection 2. The dotted red line is the distance between T_{23} and the LS plane for that epoch.

The projection techniques are very similar, but they try to minimize different errors. Projection method 1 assumes that the target lines-of-sight run normal to the surface of the blade in the first epoch and, therefore, subtracting the distance between the planes will leave comparable target positions. It should be noted that if a better estimate for the optical axis of the projector is known, the initial rotation values (ϕ_x and ϕ_z for epoch 1) can be determined and this will improve the transformation error which causes the targets to translate on the LS plane. Projection method 2 makes similar assumptions about the orientation of the projector but it preserves the offset distance for the points from the LS plane. Without any reference geometry—aside from the LS plane—the normal distance to the LS plane reasonably approximates the displacement of the points. However, projection method 2 tends to under-estimate surface curvature because it takes the smallest distance between the target and the LS plane.

In practice, since buckling typically occurs near max chord, where free-panel dimensions are relatively large, there is little absolute blade movement because it is close to the blade root. This resulted in small blade flap and twist angles (<1º). Therefore, it can be shown through small angle approximations that the projection methods produced essentially identical results, and the rotation method produced similar results. However, if the location of the videogrammetry system was shifted toward the tip, or implemented on larger test articles with more absolute movement, more careful selection of these techniques would be required.

CASE STUDY

The videogrammetry system was used on a Sandia National Laboratories 9-m WindPACT Blade System Design Studies (BSDS) blade during static and fatigue testing in Building A-60 at the National Wind Technology Center. These tests used 54 coded targets to record the motion of the high pressure surface at max chord, as shown in Figure 13. The results showed the absolute motion, twist and flap of the blade at this location, as well as the relative motions between the points.

The static test used a fixed hydraulic system to load the blade from 0 to 1500 lbf at approximately 5 m from the root plane over the course of 12 epochs. For this experiment the videogrammetry system was deployed on the high-pressure surface of the blade. This positioning was a compromise due to the logistics of the test setup. The surface of the blade can clearly be seen in the raw PhotoModeler three-dimensional data in Figure 14. The rotation of the blade surface was seen in the slight change in orientation of the LS plane through the epochs shown in Figure 15. The normalization methods were comparable due to small rotation angles. In the static test, the LS planes indicated the flap and twist angles were

0.10º and 0.05º, which resulted in a 1.6% difference between the rotation and projection methods.

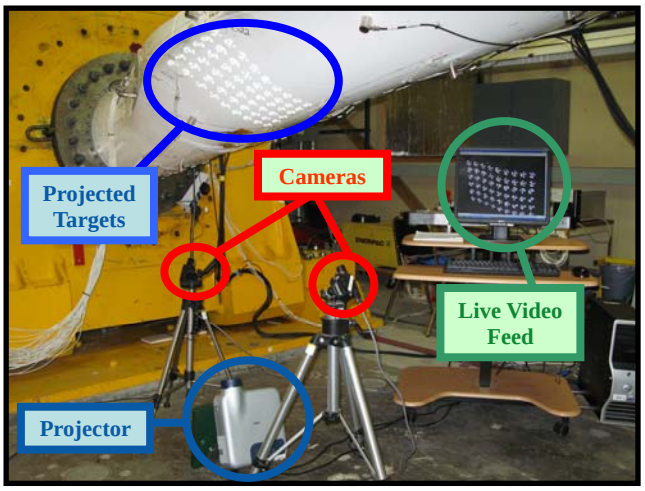

Figure 13. The videogrammetry setup for the BSDS static and fatigue tests.

The average deflections of points over the entire test are shown in Table 1. Unfortunately, the motions of the targets were on average 0.05 mm between epochs and none of the points moved more than 1 mm during the test, so the results were on the same order of magnitude as instrumentation noise, shown in Figure 16. The noise originated from camera distortions, errors in the camera calibration, and errors in the PhotoModeler ellipse-fitting algorithm used to find the center of the targets. Camera resolution, CCD noise, poor lighting and other effects combined to make it difficult for the software to determine the center of the target circle, even with subpixel accuracy in PhotoModeler. Furthermore, the 1500 lbf test load used for this experiment was well below the loading required to statically fail the blade, so the motion of the blade skin was small.

Table 1: Static test deflections for different methods.

	Rotation Method	Projection Method 1 & 2
Average point displacement during static test	0.5088 mm	0.5080 mm
Average y-displacement during static test	0.2241 mm	0.2205 mm

Photogrammetry can achieve precision results of 1:100,000 and higher, although in practice 1:30,000 is more reasonable [7]. This level of precision corresponded to ~0.03 mm since the full image field was approximately 1 m. One of the reasons the stereo-videogrammetry system suffered from low precision results was that it only incorporated two cameras. In [7] there were 19 camera stations set up and in [15] there were 5-8 camera stations. The accuracy of these results would be greatly improved with additional cameras, because the location of the target would be calculated by averaging more epipolar line intersections.

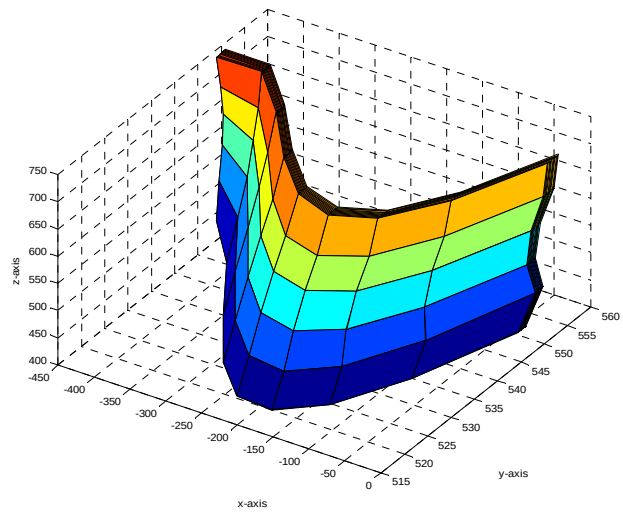

Figure 14. The surface of the blade in epochs 1-12 in the PhotoModeler coordinate system. The slight change in flapwise direction can be seen in the different layers.

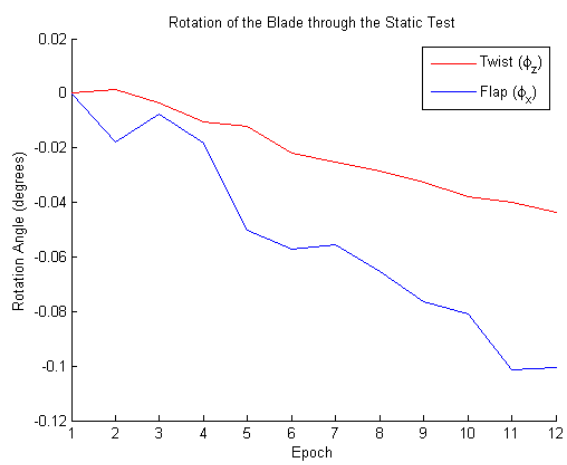

Figure 15. The twist and flap of the blade for each epoch in the static test.

Since the videogrammetry test was a proof-of-concept experiment conducted on the high pressure side of the blade, large out-of-plane motions were not expected. Thus, due to the small surface deformations and precision limitations, there was significant noise between each of the epochs; however, clearer results were obtained by comparing the first and last epoch data points. The difference in the initial and final locations of each point revealed that the center of the region of interest deformed outward, shown in Figure 17. Note that

irrespective of the method chosen, there would be points on each side of the semi-transparent plane, because the methods all center the points. The plane provides a means to qualitatively inspect for changes in the blade shape. In the case of the BSDS static test, since the targets at the extremes of the *x*-axis were on the rigid trailing edge and spar cap, it appears that the skin between the spar cap and trailing edge tended to distort outwards by a couple hundred microns. However these data are believed to be within the noise floor of the system.

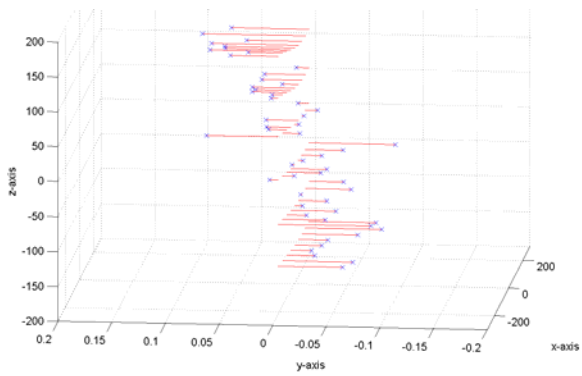

Figure 16. Motion of the centered points between epochs 10 and 11. The points all start at the y = 0 plane for illustrative purposes. The error from noise is shown by the discrepancy in motion of adjacent points.

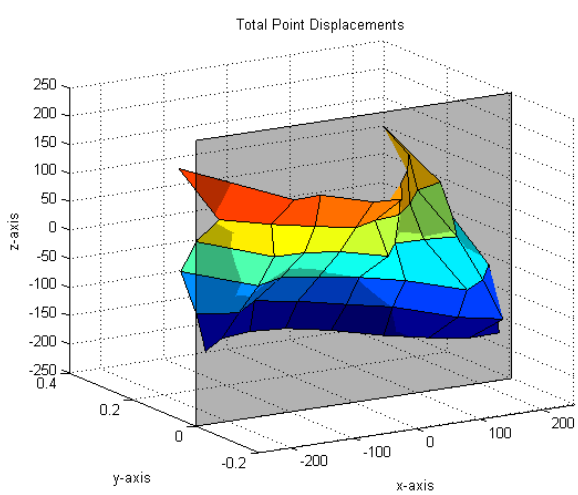

Figure 17. The y-direction displacement of the points due to static loading. The plane is drawn in at the zero deflection position.

The 1.5 Hz forced hydraulic fatigue test was run while each camera captured 300 synchronized images at 30 fps. Later 50 photos (approximately 2 cycles) were taken out of this series of epochs for post-processing. Again the test was to demonstrate the videogrammetry system, not to bring the blade to failure, so the blade deflections were small. Similar problems with the system noise were encountered as during the static test, so measurements which averaged all the epoch points such as blade displacement and LS plane rotation were most meaningful. The noise was from uncorrelated system error, so via the law of large numbers good results for the blade translation and rotations were recorded, as seen in Figures 18 and 19. Figure 18 shows that the largest motion of the projected targets was in the flapwise direction, but the targets also moved in the lead-lag and spanwise directions because the twist and flap of the blade translated the projected points. The LS plane normal vector showed that the flap angle was approximately twice the twist angle for the fatigue test loads, which matched the results for the static test in Figure 15. The measure of these angles is of particular importance, because the twist-bend coupled character-istics of the test articles are becoming more important as twist coupled aerodynamics are garnering additional research.

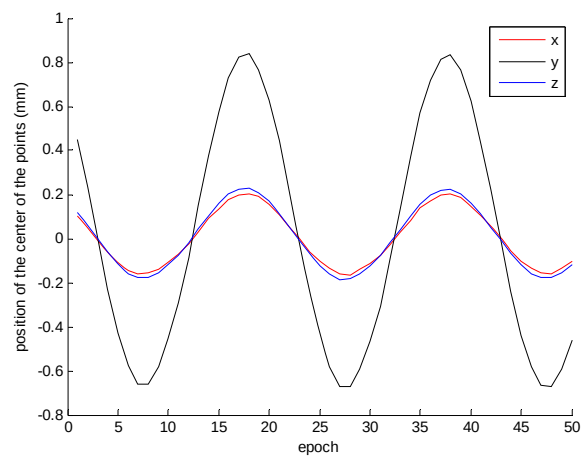

Figure 18. Displacement of the centroid of the point cloud for each of the epochs prior to applying the normalization methods.

Since fatigue tests are run for millions of cycles, it is desired to watch the periodic skin deflections over the course of the entire test to see how the skin deformation changes. If the deformations gradually increase over time this would indicate that the testing has reduced the structural stiffness over time, whereas if the blade suddenly increased the out-of-plane deformation, a more serious failure, such as cracking, could be in progress. Since the image post-processing is computationally taxing, two or three cycles of the blade could be recorded daily, and the surface deformation from the maximum and minimum flapwise positions, as shown in Figure 20, could then be analyzed. Then after the months of testing, a series of deformation values corresponding to the life of the blade could be analyzed. This information would

assist in determining if the blade failed due to buckling, a gradual decrease in strength, or a catastrophic failure.

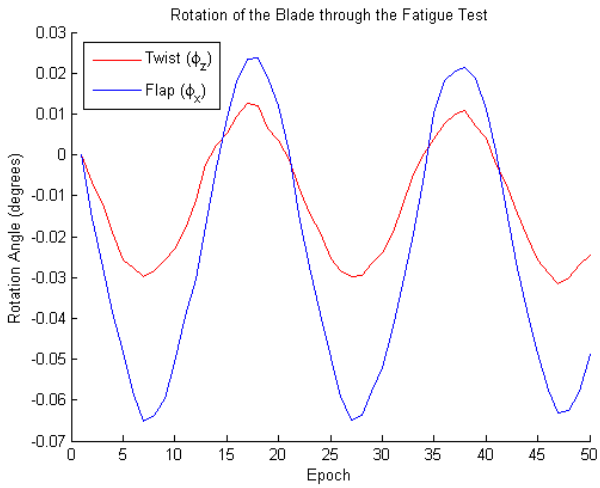

Figure 19. The twist and flap rotations of the blade with respect to the first epoch.

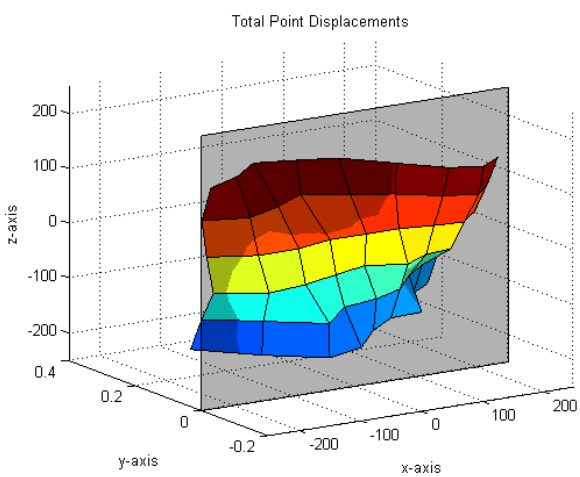

Figure 20. The y-direction displacement between epochs 7 and 18 of the fatigue test. This is the largest displacement the surface of the blade sees at this load.

CONCLUSIONS

A stereo-videogrammetry system has been created at the National Wind Technology Center to monitor the surfaces of wind turbine blades during static and fatigue testing. The system tracked projected targets on the surface of the blade with sub-millimeter accuracy, which allowed small defections and rotations of the blade to be captured. These spatial data were then converted by one of three proposed normalization methods into a common reference frame attached to the blade.

The target data were then used to quantify blade shape changes between each of the epochs and the maximum and minimum deflections. These measurements indicated areas where there was blade weakening, buckling, or other modes of damage. Additionally, the videogrammetry system monitored changes in the flap-twist-coupling and airfoil shape, which could be used to calculate the expected aerodynamic performance of operating wind turbines.

The largest difficulty with the investigated videogrammetry system is that the inter-epoch motions were close to the system noise level. As a result, the motions of individual points were very difficult to separate from the error. To gather accurate measurements of the blade, the largest displacement epochs, point cloud averages or least-squares planes were used. In the future, additional cameras will improve the accuracy of the results. Also, multiple sets of images can be captured for each of the loads in static tests. These points can be averaged to remove errors from the image processing. For fatigue tests, it would be possible to avoid some of the image noise by adjusting the capture rate until it was a multiple of the blade frequency. Then the point positions could be averaged over multiple cycles to create a mean surface shape.

ACKNOLEDGEMENTS

The authors would like to thank Mark Rumsey and the rest of Sandia National Laboratories for providing the Sandia BSDS Blade and Mike Jenks for conducting the static and fatigue tests.

REFERENCES

[1] Adams, D., White, J., Rumsey, M., and van Dam, J., 2008, “Impact, Loading and Damage Detection in Carbon Composite TX-100 Wind Turbine Rotor Blade,” 46th AIAA Aerospace Sciences Meeting and Exhibit, Reno, NV.

[2] Rumsey, M., and van Dam, J., 2008, “Experimental Results of Structural Health Monitoring of Wind Turbine Blades,” 46th AIAA Aerospace Sciences Meeting and Exhibit, Reno, NV.

[3] Rumsey. M. A., and Paquette, J. A., 2008, “Structural health monitoring of wind turbine blades,” Proc. SPIE 6933, 69330E.

[4] Paquette, J., van Dam, J., Hughes, S. and Johnson, J., 2008, “Experimental Results of Structural Health Monitoring of Wind Turbine Blades,” 46th AIAA Aerospace Sciences Meeting and Exhibit, Reno, NV.

[5] Paquette, J., van Dam, J., and Hughes, S., 2007, “Structural Testing of 9 m Carbon Fiber Wind Turbine Research Blades,” 45th AIAA Aerospace Sciences Meeting and Exhibit, Reno, NV.

[6] Lobitz, D. W., et al., 2001, “The Use of Twist-Coupled Blades to Enhance the Performance of Horizontal Axis Wind Turbines,” Sandia National Laboratories Technical Report, SAND2001-1303.

[7] Clarke, T.A., Robson, S., and Chen, J., 1993 “A comparison of three methods for the 3-D measurement of turbine blades,” Proc. SPIE Vol. 2101, Measurement Technology and Intelligent Instruments, Zhu L., et al., eds., Vol. 1, pp.1-12.
[8] Wong, K.W. 1980 “Basic Mathematics of Photogrammetry,” Chapter 2, Manual of Photogrammetry, 4th Ed. American Society of Photogrammetry, VA, pp.37-101.
[8] Graves, S.S., and Burner, A. W., 2001, “Development of an intelligent videogrammetric wind tunnel measurement system,” Technical Report NASA Langley Research Center Hampton, VA 23681-2199.
[9] Burner, A.W. and Liu, T., 2001 “Videogrammetric Model Deformation Measurement Technique,” Technical Report Technical Report NASA Langley Research Center Hampton, VA 23681-2199.
[10] Koulesh, V.P. et. al, 1999, “Videogrammetric System for Measurements of Movement and Deformation of Real-Scaled Helicopter Rotor Blades,” Image Processing Methods in Applied Mechanics, Warsaw, Poland, May 6-8.
[11] Pappa, R., et al., 2002, “Photogrammetry Methodology Development for Gossamer Spacecraft Structures,” 43rd Structures, Structural Dynamics, and Materials Conference, Denver, Colorado, Apr. 22-25.
[12] Pappa, R., et al., 2003, “Dot-Projection Photogrammetry and Videogrammetry of Gossamer Space Structures,” Journal of Spacecraft and Rockets, vol.40 no.6, pp. 858-867.
[13] Sabel, J. C., 1996 “Optical 3D Motion Measurement,” Instrumentation and Measurement Technology Conference, Brussels, Belgium, June 4-6. Vol. 1, pp. 367 – 370.
[14] Robson, S. & Setan H. B., 1996, “The dynamic digital photogrammetric measurement and visualisation of a 21m wind turbine rotor blade undergoing structural analysis,” International Archives of Photogrammetry and Remote Sensing, Vol. XXXI, (B5), 493-498.
[15] Shortis, M. R., Clarke, T. A., and Robson, S., 1995, “Practical testing of the precision and accuracy of target image centering algorithms,” Proc. SPIE Videometrics IV, El-Hakim, S.F. Eds., Vol. 2598, pp. 65-76.

ASME Early Career Technical Journal
2009 ASME Early Career Technical Conference, ASME ECTC
October 2-3, 2009, Tuscaloosa, Alabama, USA

RELIABILITY AND RISK-BASED FAILURE PREVENTION CONCEPTS FOR PIPELINE SYSTEMS

Georgios Sarakakis
Research Scientist
ReliaSoft Corporation
Tucson, AZ, USA

Dr. Dimitri B. Kececioglu, P.E.
Professor Emeritus,
Aerospace and
Mechanical Engineering
The University of Arizona
Tucson, AZ, USA

ABSTRACT

This paper presents reliability and risk-based concepts for the prevention of failures in pipeline systems. The importance of pipeline reliability is explained, together with costs related to pipeline failures. Corrosion is studied as a major cause of pipeline failures, and is approached with materials selection and corrosion prevention methods, such as cathodic protection and coating. The synergies between pipeline risk management and reliability are explained. A simple cost benefit analysis of risk reduction efforts is provided.

PIPELINE TRANSPORT

Pipeline transport is a transportation of goods through a pipe. Most commonly, liquid and gases are sent, but pneumatic tubes that transport solid capsules using compressed air have also been used. As for gases and liquids, any chemically stable substance can be sent through a pipeline. Therefore, sewage, slurry, water, or even beer pipelines exist; but arguably the most important are those transporting oil and natural gas. Often these pipelines are inspected and cleaned using pipeline inspection gauges ("pigs").

THE IMPORTANCE OF PIPELINE RELIABILITY

Maintaining safe and reliable pipeline systems is important because the products transported through pipelines – hydrocarbons in either gas or liquid form including natural gas, crude oil, high vapor pressure products such as propane and refined products such as gasoline or jet fuel – are hazardous substances. There is always the chance that pipelines could leak or rupture, and a pipeline failure can cause serious human, environmental and financial losses.

If sometimes cost analyses, engineering reports and published papers are inadequate to show the importance of pipeline reliability, recent incidents are the best proof that pipeline reliability goes even beyond enterprise earnings and longer times to failure. In January 24, 2006, CNN was reporting "More than 4 million people in Georgia were without heat for a third straight day Tuesday after a series of blasts destroyed the Russian pipeline that supplied the country's natural gas needed for its central heating. The crisis comes as the former Soviet republic battles the coldest weather it has seen in three decades. Hopes were high that heating would be restored in the next couple of days, but a number of factors now appear to be complicating that effort. Meanwhile, the repair work on the main pipeline has been postponed due to a technical problem"[1].

Constructing safe and reliable pipeline systems appears to be a major concern and effort in the U.S.A. Back in 2001 the former U.S. President stated, referring to natural gas pipelines "We will need newer, cleaner and safer pipes to move larger quantities of natural gas - up to 38,000 new miles of pipe, and 263,000 miles of [new] distribution lines" [2].

The US Department of Energy's (DOE) website states that "With the nation likely to consume 40 percent more natural gas in 2025 than it did in 2004, the integrity and reliability of the largely unseen network of pipes that lie beneath America's towns and cities will be vital to ensuring both adequate energy and the safety of the nation's citizens" [3].

The US DOE's program goals are to:

- Maintain/enhance **pipeline system reliability** and integrity.
- Increase gas deliverability.
- Reduce environmental impact by increasing the capacity of existing infrastructure.
- Reduce the environmental impact of fugitive methane emissions from pipelines and facilities.
- Address gas and electric power interdependencies and infrastructure requirements.
- Develop new technology for future intelligent gas delivery systems.
- Enhance viability of Liquid Natural Gas (LNG) as an energy option for America.

COSTS RELATED TO PIPELINE FAILURES

The average direct cost of a rupture in a large diameter natural gas pipeline is approximately $1.5 million. The cost of selective pipe replacements is about $1,400 per meter for 508-mm diameter pipes and about $3,200 per meter for 914-mm diameter pipes [4]. The average length of the rupture of natural gas pipelines is from about 20 m for a 720-mm diameter pipe to about 60 m for a 1,420-mm diameter pipe. It was estimated that direct financial loss from oil leaked from a pipeline rupture is only 1.5% of the total loss, which also includes losses due to forced outages of the pipeline, field and petroleum processing equipment, as well as damage to agriculture, forests, the environment, etc. [4]

Each consequence of a pipeline failure will have a cost associated with it, such as [5]:

- Injuries to personnel and environment.
- Loss/damage of property.
- Loss of service (down time and lost revenue).
- Environmental cleanup.
- Penalties & increased insurance rates.
- Increased operational expenses.

Reliability concepts are very useful in preventing pipeline failures. A theorized bathtub curve for pipelines is illustrated in Fig. 1.

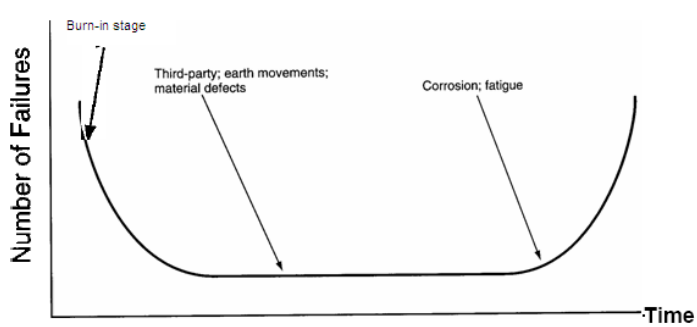

Figure 1– Bathtub curve for pipelines.

PIPELINE CORROSION AS THE HIGHEST RISK FAILURE MODE

Corrosion is defined as a destructive attack on metal by a chemical or electrochemical reaction with its environment. The driving force is the tendency for the refined metal to return to a natural state characterized by a lower internal energy. In the case of steel pipelines, the iron will tend to revert to its natural state as ferrous oxides (iron ore).

Most, if not all, buried pipelines that have been in service for five or more years experience numerous corrosion and metallurgical defects, particularly in the form of cracks. Shipilov and May [4] stated in 2004 that the sources of these cracks can be due to randomly distributed defects induced by the manufacturing process or the degradation of carbon steels used as components of pipelines. The combined action of stress (e.g., hoop and/or residual) and natural soil environment containing varying amounts of moisture and oxygen further facilitates the initiation of the crack(s) and accelerates their propagation through the pipe thickness. During pipeline operation, the cracks can grow from an initial size to a critical size large enough to cause leakage (especially in thin-walled pipelines) or spontaneous fracture (especially in thick-walled pipelines). This means that the lifetime of a pipeline containing cracks or colonies of cracks on its surface is determined by the time needed for a subcritical crack(s) to grow from an initial small size to the critical size. In other words, the lifetime of such a pipeline is determined by the rate of crack propagation.

In Fig. 2, it is evident that corrosion is the primary failure for pipeline failures, reaching 47% of the total failure causes [5]. This illustrates that it is important to study the mechanisms of pipeline corrosion and find ways to have increased pipeline reliability by developing corrosion resistance.

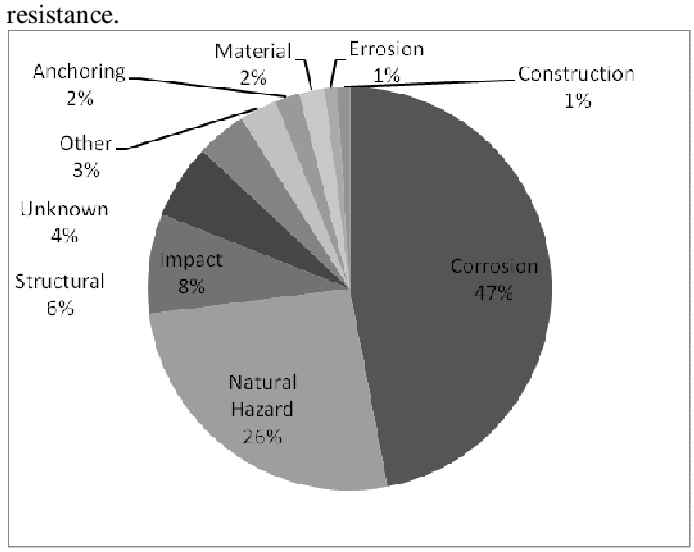

Figure 2 – Pipeline failure causes.

Steel pipe typically will last about 50 years depending upon soil conditions, quality and thickness of the steel, type of joints, corrosiveness of the water being conveyed and whether or not the steel is lined and coated to prevent corrosion [6]. Table 1 describes classifications of corrosive environments. High temperatures, high amount of oxygen, hydrogen sylfide, water and other particles, slug flow (not smooth), and low coating lifetime are all factors that indicate a very corrosive environment.

Table 1 – Classification of corrosive environments.

	VERY CORROSIVE	MILDLY CORROSIVE	NOT CORROSIVE
Temperature Range	> 100º F	100º -70º F	<70º F
Amount of Oxygen in System	>100 ppb*	20 to 100 ppb	<20 ppb
Amount of Hydrogen Sulfide in System	>1.5 psi	1.5 to 0.05 psi	<0.05
Type of Flow in System	Pseudo Slug / Slug Flow	Plug Flow	Stratified smooth Flow
Amount of Water Present in System	> 15%	14 to 5%	< 1%
Particles present in System (significant concentration)	D > 50 mils**	10 < D < 50 mils	D < 10 mils
Coating Lifetime	1 to 5 years	6 to 14 years	> 15 years

*ppb = Parts per billion.
** mil = The equivalent area of a circle whose diameter is 0.001 (10^{-3}) inch.

CORROSION INHIBITORS

Corrosion inhibitors are usually added to the inlet of a pipeline in order to reduce the corrosion rate. The effect of the inhibitor diminishes as a function of distance from the injection point. In that connection, an exponential model can be used to describe the corrosion rate along the pipeline length:

$$C_1 = 1 - e^{\left(-A\frac{L}{L_0}\right)},$$

where,

A = model parameter,

L = distance along the pipeline length,

and

L_o = characteristic length to describe the effect of the inhibitor.

This exponential behavior is illustrated in Fig. 3.

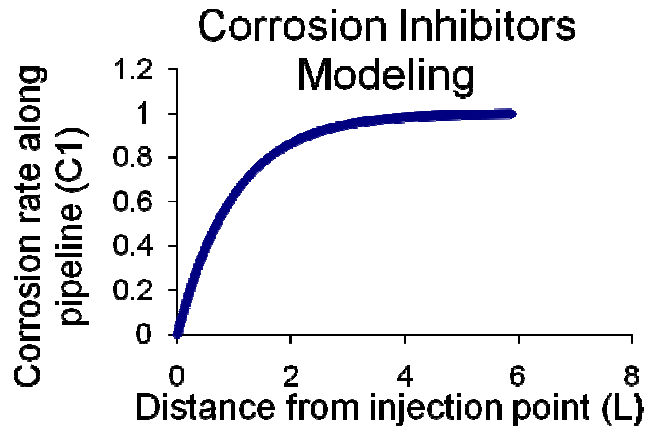

Figure 3 - Corrosion inhibitors in pipelines.

THE IMPORTANCE OF MATERIALS IN CORROSION PROTECTION

Corrosion is highly dependable on the material of the pipe. Different metals react much differently to corrosion environments. The most commonly used materials in the pipeline industry, and especially in oil and gas applications, as the most important section of pipeline engineering, are [7]:

- **Steel Pipe**

Steel is the material used in natural gas transmission systems pipes – these pipes are large in diameter and cover more than a quarter-million miles in the United States. Transmission system pipe is made of 1/4-inch to 1/2-inch thick steel, and has special coatings and Cathodic protection -- an electric current that controls corrosion on the metal surface through electro-chemistry. Some distribution main pipe is also steel, although plastic has become the material of choice for pipe installed in the last 30 years.

- **Cast Iron Pipe**

For much of the 20th century, cast iron was the choice for many urban utility systems because of its excellent resistance to corrosion. In the 1950s, steel replaced cast iron as the material of choice, mainly because of steel's ductility and strength.

- **Plastic Pipe**

During the past 30 years, plastic pipe has predominated in gas utility distribution systems operating at less than 100 pounds of pressure. In 2003, plastic pipe accounted for one-half million miles of distribution main. Plastic pipe is flexible, corrosion-resistant, easy to transport and costs less to install. Plastic pipe also can often be inserted into existing lines or through soil without traditional trenching along its entire route.

- **Titanium pipe**

Welded titanium pipe is used in the chemical industry for its corrosion resistance and is seeing growing use in petroleum drilling especially offshore for its strength, light weight and corrosion resistance. However, its cost prevents to be used in long distribution pipelines, such as oil and gas applications.

Titanium requires no corrosion allowance; pressure and structural requirements for the system are the only criteria for specifying wall thickness. Any remaining higher upfront costs are almost always a profitable investment, since the total life-cycle costs due to increased production time and reduced maintenance are lower.

Titanium forms a very tenacious surface oxide layer, which is an outstanding corrosion inhibitor. In many harsh environments it can outlast competing materials as much as 5:1. Lower failure rates translate to less downtime, reduced maintenance and total lower cost. As a result, titanium has found a home in numerous industries ranging from power generation to chemical processing to desalination plants [8].

CATHODIC PROTECTION FOR CORROSION PREVENTION

The practice of using Cathodic Protection (CP), alone or in conjunction with organic protective coatings, is generally recognized as the most effective and technically appropriate corrosion prevention methodology for buried pipelines.

Soil can be a very effective electrolyte, and a galvanic corrosion cell can be established between areas along a single pipeline or between a pipeline and another piece of buried metal. When a new piece of pipeline is attached to an old one, a galvanic corrosion cell can be established between the two metals. The two measures against this phenomenon are:

- Coating over the pipeline.
- Cathodic protection.

Coating isolates the metal from the electrolyte. If the coating is perfect, the electric circuit is blocked because the electrolyte is no longer in contact with the metal. Needless to say that no coating can ever be perfect in real applications.

Cathodic protection is engineered as follows: through connections with other metals, the pipeline is turned into a cathode, which is not subject to loss of metal. The current flow is directed in such a way that current flows to the pipeline and then away from an installed metal that is intended to corrode. This metal is called a sacrificial anode. A voltage can also be imposed to further drive the current flow. This system is called an impressed current system. In these systems, rectifiers are used to drive the low-voltage current flow between the anode bed and the pipeline (cathode). The amount of voltage is dictated by variables such as coating condition, soil type, and anode bed design, all of which add resistance to this electric circuit. Such a system is illustrated in Fig. 4.

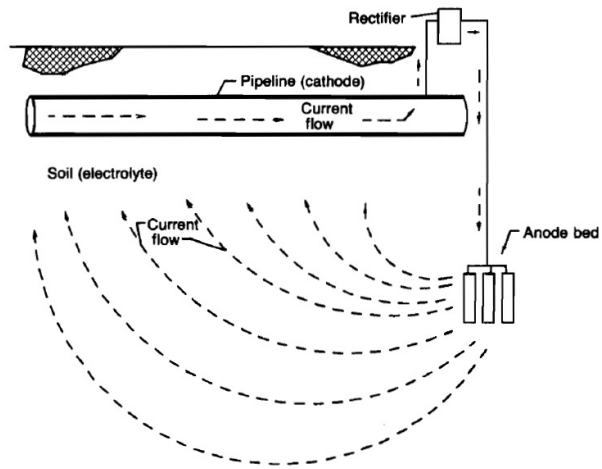

Figure 4 – Pipeline cathodic protection with impressed current rectifier.

However, there are a number of problems with this practice. One is that CP combined with a protective coating could be effective but only if the coating fails. Conversely, if the coating remains intact, CP has little effect and even does not make much sense as there can be no contact between the soil (which must be moist) and the surface of the pipe. Observations made in field studies at many locations indicated that most if not all failures on pipelines occurred with coated pipes and cracks were initiated under disbonded coating areas; i.e., at the same place where the positive (i.e., protective) effect of CP was expected. All these failures occurred on buried pipelines having CP. Marr et al. [6] wrote in 2003, "the failure of a coating system is a primary factor in the initiation and propagation of Stress Corrosion Cracking."

RELIABILITY AND RISK FOR PIPELINE FAILURE PREVENTION

Reliability concepts are identical to risk concepts in many regards. In fact, sometimes the only differences are the scenarios of interest. Where risk often focuses on scenarios involving fatality, injury, property damage, etc., reliability focuses on scenarios that lead to equipment unavailability, repair costs, etc.

Risk analysis is often more of a diagnostic tool, helping us to better understand and make decisions about an overall existing system. Reliability techniques are more naturally applied to new structures or the performance of specific components.

Many of the same techniques are used, including Failure Modes Effects and Criticality Analysis (FAMECA), root cause analyses, and event-tree/fault-tree analyses. This is logical since many of the same issues underlie risk and reliability. These include failure rates, failure modes, mitigating or off-setting actions, etc. [9].

Common reliability measurement and control efforts involve the following issues:

1. Equipment performance, as measured by availability, uptime, MTTF (mean time to failure), MTBF (mean time between failures), and Weibull analyses.
2. Reliability as a component of operation cost or ownership costs, often measured by life-cycle cost.
3. Reliability analysis techniques applied to maintenance optimization, including Reliability Centered Maintenance (RCM), Predictive Preventive Maintenance (PPM), and Root Cause Analysis. Many of these are, at least partially, risk analysis techniques, the results of which can feed directly into a risk assessment model.

PIPELINE RISK SCORING

Fig. 5 illustrates the relative risk score that reflects the risk in any given pipeline scenario.

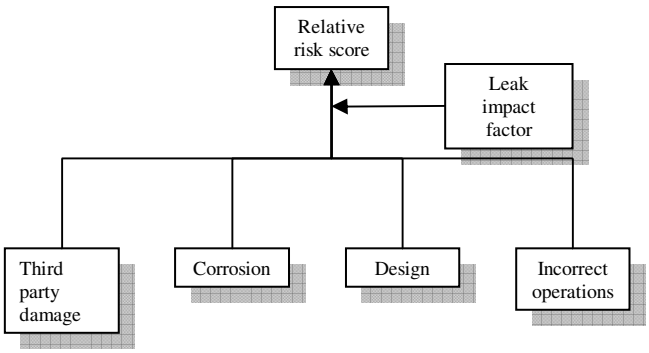

Figure 5 – Pipeline risk score.

Pipeline risk management uses weight factors for all defined causes that elevate risk, just as pipeline reliability management uses relative equations to predict failures in time. This practical approach can be very useful in terms of predicting the risks in a pipeline project, and can give a good reflection of the underlying reliability without having to calculate probabilities of failure. A framework of a pipeline risk management program is given in Fig. 6 and a flow diagram for calculating risk in Fig. 7.

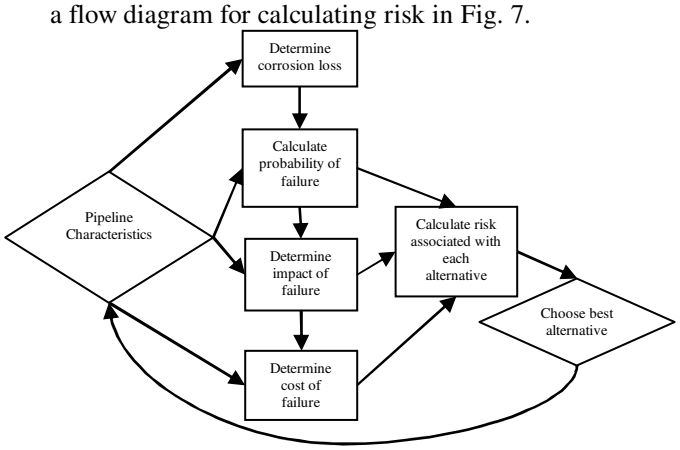

Figure 6 – Framework of a pipeline risk management program.

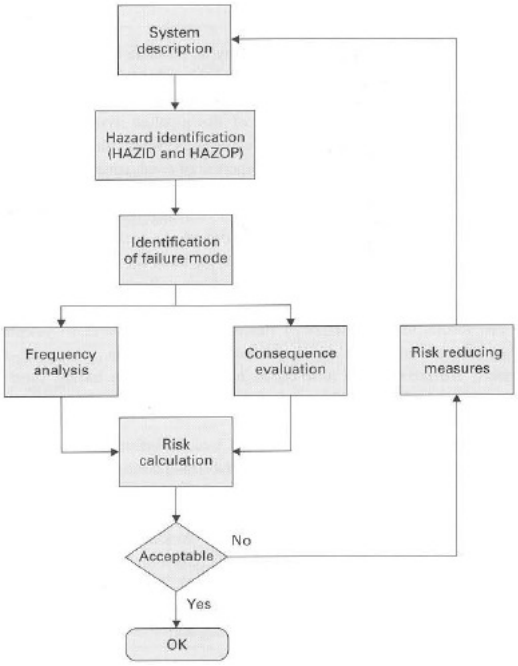

Figure 7 – Flow chart for pipeline risk calculation.

RISK ASSESSMENT AND COST-BENEFIT ANALYSIS

The methodology for the risk analysis is identical for each hazard. If the frequency and consequences of hazards are established, then the risk is defined as the product of the frequency (f) and the consequences (C):

$$\text{Risk} = f \times C.$$

In principle, the accident frequency is established on the basis of statistical information or appropriate mathematical modeling of a situation that can result in damage of the pipeline. The consequences can be defined in various ways, depending on the risk policy that is adopted. Typical consequences are system downtime, loss of property, fatalities and pollution of the environment [9].

A cost benefit analysis is an appropriate method to evaluate the gained risk reduction versus the extra cost. The cost benefit value (CBV) is defined as [10]:

$$CBV = \frac{\Delta Cost}{\Delta Risk},$$

Where,

ΔCost = increased cost due to additional risk reducing measures, expressed in monetary terms, e.g. Dollars.

and

ΔRisk = reduced risk due to the measures. The risk is measured again measured in terms of monetary values, by considering the expected probability of occurrence and

multiplied by the implicit consequence in terms of monetary values.

A cost effective solution will give a ratio of less than one, whereas a non cost-effective solution will give a ratio greater than one.

CONCLUSIONS

In this paper we presented reliability and risk-based concepts for application in pipeline systems. Pipeline failures create huge unscheduled costs and disruption of service that is considered in most cases critical. We focused on addressing pipeline corrosion as the major preventable cause of pipeline failures. Existing solutions, such as careful material selection, cathodic protection and coating can drastically improve the designed-in reliability in pipeline systems. We also suggested a risk based approach by presenting a systematic risk management program for pipelines. We also provided a simple cost benefit analysis that compares the extra cost in order to reduce risk with the expected risk reduction.

The application of reliability and risk-based failure prevention methods can be beneficial in terms of avoiding costly pipeline failures and can provide increased network availability and safer pipeline operations.

REFERENCES

[1] Ryan Chilcote, 2006, "Millions in Georgia without heat", http://www.cnn.com

[2] Fossil Energy Office of Communication, 2006, "Transmission, Distribution & storage", www.fosil.energy.gov/programs/oilgas/delivery/index.html

[3] American Gas Association, 2006, "Pipeline Safety and Reliability", http://www.aga.org/Content/NavigationMenu/Public_Relations1/Pipeline_Safety_and_Reliability/Pipeline_Safety_and_Reliability.htm

[4] Shipilov, S. A., and Le May, I., 2006 "Structural Integrity of Aging Buried Pipelines Having Cathodic Protection", Engineering Failure Analysis, Vol. 13, pp.1159-1176.

[5] Farkas, B., and Bea, R.G., 1998, "Pipeline Inspection, Maintenance and Performance Information System Progress Report", University of California at Berkeley, Marine Technology Group.

[6] Marr, J.E., Hardy, S.B., and Huuskonen, E., 2003, "SCC integrity management – liquid and gas pipeline systems", Calgary, Marr Associates.

[7] American Gas Association, 2006, "Pipeline Safety facts", http://www.aga.org/Template.cfm?Section=Pipeline_Safety_Facts_and_Resources&Template=/ContentManagement/ContentDisplay.cfm&ContentID=17342

[8] Azom Materials , 2006, "Titanium Applications", http://www.azom.com/details.asp?ArticleID=1297

[9] Muhlbauer, W.K., 2004 "Pipeline Risk Management Manual-Ideas, Techniques and Resources", Third Edition, Elsevier.

[10] Braestrup, M.W., 2005, "Design and Installation of Marine Pipelines", Co-published by Blackwell Science and ASME.

ASME Early Career Technical Journal
2009 ASME Early Career Technical Conference, ASME ECTC
October 2-3, 2009, Tuscaloosa, Alabama, USA

A NOVEL GRADIENT-TYPE METHOD BASED ON MAXIMUM ENTROPY PRINCIPLE APPLIED TO THE INVERSE RADIATION PROBLEMS

Ramin K. Rahmani
Affiliate Research Scholar
MIME Department
The University of Toledo
Toledo, Ohio, USA

Hosein Molavi
Researcher
Department of Mechanical Engineering
Tarbiat Modares University
Tehran, Tehran, Iran

Anahita Ayasoufi
Affiliate Research Scholar
MIME Department
The University of Toledo
Toledo, Ohio, USA

ABSTRACT

The development and verification of a novel gradient-type method is presented. The method is then used to predict the profile of heat flux over the heater surface for an enclosure filled with an emitting, absorbing, and scattering medium. Experiences show strong fluctuations in the retrieved heat flux during optimization process which is not suitable for practical applications. The solution of these problems is obtained by minimization of a quadratic criterion. In order to control the variations in the estimated parameters and achieving smooth profile over the heater surface, an additional term based on maximum entropy technique is added to the objective function. A generalized grid based finite volume scheme is devised to solve the radiative transfer equation. Numerical simulations are conducted to evaluate the performance and accuracy of the present approach. The new features of the combined methodology make it viable for analyzing the inverse heat transfer problems from the function estimation problems in heat conduction to boundary design problems in radiation.

INTRODUCTION

The ability to establish the desired conditions in one part of a thermal system has many applications in various branches of science and engineering. Achievement of those conditions requires adequate controlling of the conditions in other parts of the system through special equipments. Such problems involve a variety of challenges and have received considerable attention from many researchers in recent years [1-13]. Estimation of the energy input that equips radiant heaters, from the knowledge of desired temperature and heat flux profiles over a given design surface, is a radiative boundary design problem. The limitation of the forward design method (i.e., trial-and-error procedure) in determining required conditions on the heater surfaces, due to reliance on the designer's experience and its large computational time, prompts the use of optimization and inverse design techniques, which are reliable and significantly less expensive. These methodologies use all the available information specified for designed surfaces to set the necessary input on the heater surfaces. In other words, what the designer faces, is a problem of predicting cause on the basis of its observable results. Inverse design methodologies use the features of regularization method to reduce ill-posedness of the problem and to obtain a reliable inverse solution by sacrificing the accuracy of the solution to some degree. Several authors have used a variety of regularization techniques for inverse design problems [1-4]. These techniques include the Tikhonov regularization, truncated singular-value decomposition (TSVD), and conjugate gradient regularization. Daun et al. [4] compared these techniques and reported very similar results. However, every method has its unique features. The major benefit of conjugate gradient regularization is that it consumes less computational resources than other mentioned methods. When the heater surfaces contain many heaters, the TSVD method becomes time-consuming, but it can provide valuable insight into the estimation procedure. Tikhonov regularization approach penalizes by large variations in the unknown quantities. Selection of the optimal Tikhonov parameter is an important issue in applying the current method [4,13].

Optimization methodologies use iterative procedures to determine the design parameters. The performance evaluation of these techniques at each iteration is accomplished using an error function. In general, prediction of solution for aforementioned techniques can be achieved via minimization of a sum of squared error function; which is focused on the difference between the values of the measured heat fluxes and those obtained by an efficient computational method. The unknown heat fluxes on the mathematical model that minimize the aforementioned error function are the solution of the problem. Any optimization algorithm, regardless of its theoretical approach, requires the usage of a well-established solution routine for direct problem calculations. This solution routine may be called upon numerous times by the main optimization computational routine. Therefore, the use of highly efficient, as well as accurate, direct calculation schemes

is essential in any optimization technique. During the past decades, a large number of investigations have been conducted to solve the radiative transfer equation for different problems. The numerical methods such as the Finite Volume Method (FVM) [14-15], Discrete Ordinate Method [16], and the Discrete Transfer Method [17] can accurately predict radiative heat transfer in emitting-absorbing-scattering media. In this paper a conservative cell-based version of FVM scheme is devised for predicting radiative heat transfer under different boundary conditions using generalized computational grid. Two important categories of optimization strategies are metaheuristic and deterministic. Metaheuristic class uses the random number generator algorithms to search a solution space to select feasible design parameters. Simulated annealing and tabu search are two metaheuristic methods. Details about the application of metaheuristic methods to the radiative boundary design problems can be found in Refs. [4-5]. Gradient-based methods belong to the deterministic category in which the concept of gradient of error function plays an important role in reaching the final solution. In recent years inverse radiation problems are solved considering classical gradient-base techniques, such as Conjugate gradient, quasi-Newton, Newton, and Levenberg-Marquart [6-13]. In many situations, after finding the optimal solution, high-amplitude fluctuations are observed in the final profile of the heat flux at the heater surface, which may be difficult to apply in a practical application. One way to control the variations in resulting profile is to add a term to the error function. Under this circumstance, the gradient of error function and the search step size will change with respect to the traditional method. Kowsary et al. [13] modified the error function and used the variable metric method (i.e., quasi-Newton) to determine distribution of the heating elements' strengths in a radiation furnace. They considered various values for Tikhonov coefficient to determine its optimal value, which yields minimum bias and low variance of the estimated heat flux.

This paper introduces a novel approach in gradient-type methods, which is quite different from traditional methods available in the literature, and shows its application to radiative boundary design problems. This method was recently applied to inverse heat conduction problems to estimate the unknown time-varying heat flux under different conditions by the authors [18]. Considerable improvement resulted, when this method was implemented as an optimization technique. In order to overcome the difficulty associated with optimization problems, Maximum Entropy Method (MEM), which is based on probabilistic theory, is combined with the method in the present work. This technique has been applied as a regularization method to various inverse heat conduction problems [19-21]. Using the quadratic programming for determining search direction in MEM needs the calculation of the Hessian matrix and the gradient vector of the objective function and the constraints. However, the evaluation of the Hessian matrix is not an easy task. The present approach is unlike those appearing in the literature, because it does not require any constraints and evaluation of Hessian matrix, which usually consume considerable computational resources. Implementation of the present method only demands modification of the gradient vector and the search step size with regard to the traditional method without additional term, as will be described later in the related section. Entropy smoothing function has a logarithmic form and is added to the error function to seek the most likely solution [22]. The selection of coefficient of the added term is arbitrary and the optimal value for this parameter can be determined by trial and error, so that both minimum error function and low variance of the estimated parameters can be observed. In order to evaluate the performance of the combined strategy, it is applied to two test cases that are two-dimensional furnaces filled with an absorbing, emitting, and scattering gas.

NOMENCLATURE

d	descent direction
f	the error functional
I	intensity of radiation; or identity matrix
I_b	blackbody intensity
M	total number of elements on the design surfaces
N	total number of elements on the heater surfaces
q	radiant heat flux
s	vector of descent direction in Eqs. (11)-(14); or geometric path length
X	sensitivity matrix
α	coefficient of added term to error function
β	descent parameter
ε	surface emissivity
κ	absorption coefficient
σ	Stefan-Boltzmann constant
σ_s	scattering coefficient
Ω	solid angle
∇f	gradient of the error functional

Subscripts

b	black surface
c	calculated
d	design surface
h	heater surface
i	iteration number

Superscripts

T	transpose of a matrix

STATATEMENT OF THE INVERSE PROBLEM

The radiative transfer equation for a gray absorbing, emitting, and scattering gas in direction s can be written as [23]

$$\frac{dI(r,s)}{ds} = -\left[\kappa(r)+\sigma_s(r)\right]I(r,s)+\kappa(r)I_b(r)+ \frac{\sigma_s(r)}{4\pi}\int_{4\pi} I(r,s')\Phi(s',s)\,d\Omega' \quad (1)$$

where I is the radiant intensity, I_b is the blackbody intensity, s is the coordinate along the ray, κ is the absorption coefficient, σ_s is the scattering coefficient, Φ is the scattering phase function, r is the position vector, s is the direction vector, and Ω' is the control angle direction.

All boundaries are assumed to be gray and diffuse. Under this assumption, the boundary condition for each of the surfaces can be written as

$$I(r,s) = \frac{q(r)+\int_{s.n>0} I(\hat{r},\hat{s})\,s.n\,d\Omega}{\pi} \quad (2)$$

where

$$q(r) = \pi\varepsilon I_{b,w}(r) - \varepsilon\int_{s.n>0} I(r,s)\,s.n\,d\Omega \quad (3)$$

is a radiant heat flux, ε is surface emissivity, $I_{b,w}$ is the blackbody intensity of boundary surfaces, and n is the surface normal pointing out of the domain.

Figure 1 shows an illustrative example of a simple inverse radiation problem in a rectangular enclosure. The enclosure is filled with gray absorbing, emitting, and scattering gas. Here, both the heat flux and temperature are specified on surface 1; and the designer aims to predict the profile of heat flux desired on surface 3 to provide these conditions. In order to estimate the distribution of the heat flux over the design surface, when it is set over the heater surface, a suitable numerical procedure is necessary. The finite volume method has been extensively used to analyze many different radiant enclosure problems, and is especially well suited for analyzing enclosures with irregular shapes. There is no restriction on discretization of the angular domain and uniformity of the control angles and the ray effect can be easily removed [14]. In the present study, no attempt is made to describe the applied finite volume method and the interested reader is referred to Refs. [14-15] for details. It is worth mentioning that the solution of the direct problem will become different from those previously published in the literature, when the heat flux at the heater surfaces is specified. Under this circumstance, the blackbody intensity of the boundary surfaces with constant heat flux will systemically change until convergence of the computational algorithm is reached. The computational algorithm for the direct solution is briefly described as follows:

1) Suppose blackbody intensity over the domain and boundary surfaces are available.
2) Solve the radiative transfer equation to obtain the intensity field in the enclosure.
3) Update the blackbody intensity field as follows:

$$I_{b,new} = \sum_l \frac{I^l\Omega^l}{4\pi} \quad (4)$$

4) Update the blackbody intensity of boundary surfaces with constant heat flux as follows:

$$I_{b,w,new} = \frac{\left(q/\varepsilon + \int_{s.n>0} I(r,s)\,s.n\,d\Omega\right)}{\pi} \quad (5)$$

5) Examine the stopping criterion given by $I_{b,new} \cong I_{b,old}$. If not satisfied, proceed to Step 2.

OPTIMIZATION PROCEDURE

In the inverse problem considered in this study, the heat flux over the heater surface ($\vec{q}_h$) is regarded as being unknown and to be estimated from the knowledge of a desired temperature and heat flux profiles over a given design surface. The solution of the present inverse problem is to be obtained in such a way that the following function is minimized:

$$f(\vec{q}_h) = \sum_{j=1}^{M}\left[q_{d,j} - q_{c,j}(\vec{q}_h)\right]^2 \quad (6)$$

where $q_{d,j}$'s are the desired heat fluxes over the design surface and $q_{c,j}$'s are the estimated heat fluxes obtained by the developed direct code. M is the total number of elements on the design surfaces. The optimal point of function f can be achieved via an iterative process. The performance of minimization technique can be evaluated at each iteration. Among the well-known methods for design optimization methodology, the gradient methods have received the most attention. The minimization procedure of the function (6) by utilizing gradient-type methods is built as follows:

$$q_{h(i+1)}(t) = q_{h(i)}(t) - \beta_i d_i(t) \quad (7)$$

where the subscript i is the iteration number, β_i is the optimal step length, and $d_i(t)$ is the search direction. The success of these methods depends on effective choices of both the direction $d_i(t)$ and the step length β_i. Depending on the selection of the search direction, various types of gradient methods exist. The search direction often has the form:

$$d_i(t) = -B_i^{-1}\nabla f_i \quad (8)$$

$$\nabla f_i = -2\sum_{j=1}^{M}\sum_{k=1}^{N}\left[q_{d,j} - q_{c,j}(\vec{q}_{h,i})\right]\frac{\partial q_{c,j}}{\partial \vec{q}_{h,k}} \quad (9)$$

where N is the total number of elements on the heater surfaces and $\frac{\partial q_{c,j}}{\partial \vec{q}_{h,i}}$ are the elements of the sensitivity matrix, X.

$$X_{mn} = \frac{\partial q_{c,m}}{\partial \vec{q}_{h,n}}; \quad \begin{cases} m = 1,2,...,M \\ n = 1,2,...,N \end{cases} \tag{10}$$

In the steepest descent method B_i is simply the identity matrix, while in Newton's method B_i is the exact Hessian $\nabla^2 f_i$ [24]. In the Hestenes–Stiefel form of the conjugate gradient method, $(B_i)^{-1}$ has the following form [24]

$$\left(B_{i+1}\right)^{-1} = \left(I - \frac{s_i \left[\nabla f_{i+1} - \nabla f_i\right]^T}{\left[\nabla f_{i+1} - \nabla f_i\right]^T s_i} \right) \tag{11}$$

where $s_i = \beta_i d_i(t)$. In the Fletcher–Reeves version of CGM, $(B_i)^{-1}$ is replaced by [24]

$$\left(B_{i+1}\right)^{-1} = \left(I - \frac{d_i \nabla f_{i+1}{}^T}{\nabla f_i{}^T \nabla f_i} \right) \tag{12}$$

In quasi-Newton methods, B_i is an approximation to the Hessian that is updated at every iteration by means of a low-rank formula. For instance, the BFGS version of VMM uses the following equation for $(B_i)^{-1}$ [24]

$$\begin{aligned} \left(B_{i+1}\right)^{-1} = & \left(I - \frac{s_i \left[\nabla f_{i+1} - \nabla f_i\right]^T}{\left[\nabla f_{i+1} - \nabla f_i\right]^T s_i} \right) \left(B_i\right)^{-1} \\ & \left(I - \frac{\left[\nabla f_{i+1} - \nabla f_i\right] s_i^T}{\left[\nabla f_{i+1} - \nabla f_i\right]^T s_i} \right) + \frac{s_i s_i^T}{\left[\nabla f_{i+1} - \nabla f_i\right]^T s_i} \end{aligned} \tag{13}$$

The interested reader is referred to Ref. [24] for a detailed discussion of the gradient methods. In the present paper, an attempt is made to compromise between Eqs. (11), (13). Subsequently, the following equation is suggested to compute the search direction:

$$\left(B_{i+1}\right)^{-1} = \left(I - \frac{s_i \left[\nabla f_{i+1} - \nabla f_i\right]^T}{\left[\nabla f_{i+1} - \nabla f_i\right]^T s_i} \right) \left(I - \frac{\left[\nabla f_{i+1} - \nabla f_i\right] s_i^T}{\left[\nabla f_{i+1} - \nabla f_i\right]^T s_i} \right) \tag{14}$$

The optimal step length β_i is chosen as the one that minimizes the function $f[q_h]$ at each iteration i. The search step size can be determined by using a first-order Taylor series approximation and performing the minimization:

$$\beta_i = \frac{\left[Xd_i\right]^T \left[q_d - q_c\left(\vec{q}_{h,i}\right) \right]}{\left[Xd_i\right]^T \left[Xd_i\right]} \tag{15}$$

For the implementation of the iterative procedure, described here, the sensitivity term X is required. The following section provides the equations required for determining the sensitivity coefficients.

The Sensitivity Problem

The sensitivity problem is used to determine the variation of the dependent variables due to the changes in the unknown quantity. Therefore, the sensitivity problem can be obtained by differentiating the radiative transfer equation with respect to the unknown parameters, $q_{h,n}$. Thus, the following problem for the sensitivity function, D_n, can be obtained:

$$\frac{dD_n}{ds} = -\left[\kappa + \sigma_s\right] D_n + \kappa D_{b,n} + \frac{\sigma_s}{4\pi} \int_{4\pi} D\left(s'\right) \Phi\left(s', s\right) d\Omega' \tag{16}$$

where

$$D_n = \frac{\partial I}{\partial q_{h,n}}; \quad D_{b,n} = \frac{\partial I_b}{\partial q_{h,n}} \tag{17}$$

And the boundary conditions are:

$$D_n = \frac{\varepsilon D_{b,n} - \left(1-\varepsilon\right) \int_{s.n>0} D_n\left(s\right) s.n d\Omega}{\pi} \tag{18}$$

where $D_{b,w,n} = \partial I_{b,w} / \partial q_{h,n}$ is zero for surface elements with specified blackbody intensity I_b. Since the sensitivity equation is similar to RTE, it can be solved with the same method, which is FVM. In order to compute the sensitivity coefficients, the sensitivity problem must be solved N times, where N is the total number of elements on the heater surfaces.

Maximum Entropy Method

Although usage of optimization techniques leads to state of "exact matching", their solution usually appears to be highly gyrating that is not acceptable for industrial applications. To obtain physically rational solutions and damp high-amplitude fluctuations in the results, an additional term is added to the objective function; in other words, this strategy scarifies the accuracy, in the acceptable level, to make the results suitable for practical applications. In this work, entropy function is added to the objective function (Eq. (6)) to smooth the solution:

$$f\left(\vec{q}_h\right) = \sum_{j=1}^{M} \left[q_{d,j} - q_{c,j}\left(\vec{q}_h\right) \right]^2 + \alpha \left(1 - \frac{S\left(\vec{q}_h\right)}{\ln N} \right) \tag{19}$$

where the discrete entropy function S is defined by:

$$S\left(\vec{q}_h\right) = -\sum_{k=1}^{N} s_k \ln\left(s_k\right); \qquad s_k = \frac{q_{h,k} - q_h\big|_{\min}}{\sum_{i=1}^{N}\left(q_{h,i} - q_h\big|_{\min}\right)} \tag{20}$$

It should be noted that entropy function is nonnegative and that its maximum value is equal to $\ln N$. Therefore, the added term is always positive and compensates the variation in heat flux. Choosing the optimal value for the coefficient of the added term, α, is a challenging task because a very small value for this parameter results in an accurate solution, while creating high oscillations in estimated solution; whereas, larger values of α will produce the smooth solution while creating high values of error.

Combining MEM with the optimization methodology modifies the gradient vector and the search step size with regard to the traditional method, Eqs. (9), (15), to stabilize the solution. The gradient of the objective function, Eq. (19), is:

$$\nabla f_i = -2\sum_{j=1}^{M}\sum_{k=1}^{N}\left[q_{d,j} - q_{c,j}\left(\vec{q}_{h,i}\right)\right]\frac{\partial q_{c,j}}{\partial \vec{q}_{h,k}} - \alpha\frac{1+\ln\left(s_k\right)}{\ln N \times \sum_{i=1}^{N}\left(q_{h,i} - q_h\big|_{\min}\right)} \tag{21}$$

The search step size, β_i, is chosen as the one that minimizes the function $f\left(q_{h(i)} - \beta_i d_i\right)$. Therefore, the corresponding equation will become nonlinear with one unknown, β_i, and an iterative solution procedure is necessary to solve for the search step size.

Computational Algorithm for the Optimization Method

The computational procedure for the proposed method can be summarized as follows:

Suppose the values of $q_{h(i)}$ are available at iteration i (as initial estimated values for each iteration).

1) Solve the sensitivity problem to obtain sensitivity matrix, X.
2) Solve the direct problem with available estimated $q_{h(i)}$ to obtain the distribution of heat flux over the design surfaces.
3) Examine the error function given by Eqs. (6) or (19), depending upon absence or presence of MEM. If it is an acceptable value, stop the iterative procedure.
4) Calculate the gradient of the functional given by Eq. (9) or (21).
5) Compute descent direction, d_i, first by applying Eq. (14), and then by computing Eq. (8).
6) Compute the descent parameter, β_i.
7) The updating rule for the gradient-type method, Eq. (7), is then applied to determine the new value for heat flux over the heater surfaces. Then, replace i by i+1 and return to step 2.

RESULTS AND DISCUSSION

In order to assess the accuracy and efficiency of the present method, two simulated test cases for estimation of heat flux over the heater surfaces are considered. Both of the numerical simulations are performed for irregular two-dimensional enclosure filled with an emitting, absorbing, and isotropic scattering medium using the generalized grid. The following values are used for the gas properties: κ=1m^{-1}, σ_s=0.5 m^{-1}.

Three kinds of boundary surfaces are denoted in this study: Design surfaces, heater surfaces and reradiating (i.e., insulated) surfaces. In all of the results presented in this paper, heat fluxes are nondimensionalized using $E_{b,r}=\sigma T_r^4$, in which T_r is a reference temperature and σ is the Stefan-Boltzmann constant (5.67x10^{-8} W/m^{2}K^4). The temperature values are also nondimensionalized by T_r.

Numerical Test Case 1

The first boundary design problem, presented here, considers the radiative heat transfer inside an eccentric horizontal cylindrical annulus, as sketched in Fig. 2. On the outer cylinder there are heated elements of finite shape and size. The shape of the heated-element is assumed to be approximately a square, inclined at an angle of θ_h. The temperature and heat flux distributions on the inner cylindrical surface (i.e., the design surface) are desired to be maintained uniform. The objective of this exercise is to find the power input to the heater in which prescribed conditions on the design surface are achieved.

It is assumed that all the walls are gray and diffuse. The emissivities on the outer and the inner (design) surfaces are supposed to be 0.8. On the design surface, two boundary conditions of uniform dimensionless temperature, T=1, and radiative heat flux, q_d=-1, are applied. In the FVM calculations, the computational domain is discretized into 429 elements with quadratic meshes[1] and the angular space is discretized using 16 divisions in polar angles and 1 in azimuthal directions. The heater surface is divided into 74 elements, while the design surface is discretized into 30 elements.

At the first stage, the potential of the proposed method for recovering profile of heat flux over the design surface without additional term is investigated. The initial guess value of 0.1 for heat flux is used for the iterative procedure. Figure 3 shows the convergence rate and accuracy of the present method; in which the reduction of the error function is plotted with regard to iteration cycles. As can be seen, the value of error function reduces sharply with large slope at the first three iterations from nearly 20 to about 0.001. As the number of iteration increases, the value of error function reduces in a uniform manner, reaching to 10^{-5} for an iteration number of 77. Figure 4 compares predicted heat fluxes for different iteration numbers.

[1] The spatial domain is meshed by the commercial code GAMBIT, using the pave method.

The iteration numbers are chosen in such a manner that sensible improvement in the accuracy occurred. At the third iteration cycle, the profile of heat flux is smooth, while the value of error function is about 10^{-3}. However, as iteration number increases, the accuracy improves and amplitude of fluctuations in the retrieved heat flux increase. Since a smooth distribution of heat flux is more practical and demanded for industrial applications, a procedure is needed to stop the iterative algorithm with the tendency to lose less accuracy when the desired heat flux is achieved. Such difficulty can be alleviated by utilizing MEM. When the problem takes advantage of the maximum entropy scheme, the results depend on the choice of the parameter α. In order to show the effect of this parameter on the accuracy of the results, the problem was solved for different values of α and the corresponding accuracy reported. Figure 5 presents the dependency between this parameter and the accuracy. The error in the recovered heat flux becomes greater as the parameter deviates more from zero. However, the magnitude of oscillations reduces in the final profile, as depicted in Fig. 6. The results obtained on this figure reveal the fact that the heat flux profile over the heater surface becomes smoother as the parameter, α, increases. The optimal value for α can be achieved via trial and error.

Numerical Test Case 2

The proposed methodology is also employed to solve a design problem involving a 2-Dimensional diffuse-walled enclosure whose lower surface has a step-like geometry as shown in Fig. 7. The purpose of the design problem is to find a heat flux distribution over the heater surface, that maintains a uniform dimensionless heat flux of "-1" and a uniform dimensionless temperature of unity over the design surface. Each heater surface on the side wall is divided into 20 elements, while the heater surface on the top wall is separated into 35 elements. Hence, 75 components are considered for the unknown heat flux over the heater surfaces.

Figure 8 shows the recovered heat flux around the heater surfaces using the suggested algorithm. The lower left corner of the enclosure coincides with the origin of the x axis in this figure. Heater elements are ordered in the clockwise direction from the origin point of the enclosure. Then, the axis x can be divided into three parts as shown in the figure: First, the left side of the heater surfaces which governs part of the region on the x axis from 0 to 20. Second, the upper part of the heater surfaces which constitutes numbers from 21 to 55 on the x axis. Third, the right side of the heater surfaces which belongs to numbers from 56 to 75 on the x axis. As indicated in this figure, strong fluctuations appear in the final solution which shows the exact matching of the computational procedure and poses a practical problem in real practical conditions. Moreover, some components of the estimated heat flux over the heater surface become negative. This critical condition, which corresponds to physically unacceptable solutions, has been encountered in some previous studies and different approaches have been suggested for addressing it [3,13,25]. In order to establish a nonnegative and reliably practical solution, and to relax the exact matching of data, MEM is used. A value of 0.1 is selected for parameter α which is a compromise between the accuracy and the variance, obtained through a trial and error process, as noted in the previous example. Figure 9 demonstrates the corresponding heat flux over the heating surface which is notably smoother than the one without additional term and is acceptable from an engineering point of view. To evaluate the accuracy of the combined methodology, the resulting heat flux distributions over the design surface were calculated with estimated heat flux over the heater surface and were compared to the exact solution and those obtained with no additional term (which is shown in Figure 10). Desired uniform heat fluxes without extra term are achieved at the final stage. However, desired heat flux distributions using combined strategy could be achieved except at the corner regions. Results indicate that the combined algorithm is capable of providing heat fluxes close enough to the design value. The reduction histories of the objective function with and without extra term are shown in Fig. 11. It is observed that the combined methodology cannot decrease the objective function below a certain value. It should be pointed out that the combined methods sacrifice accuracy to some degree to assure the stability in the solution and this does not mean that the combined method is not helpful. The relative errors of the corresponding heat flux distribution over the design surfaces are shown in Fig. 12. It is obvious that the relative error for the combined strategy is higher than the method without additional term and higher error is within the acceptable range.

CONCLUSION

A novel gradient-type method was introduced for estimating the heat flux distribution over the heater surfaces of enclosures filled with an emitting, absorbing, and scattering medium. It was shown when the method is combined with the maximum entropy technique, it is capable of producing acceptable results by removing strong fluctuations, which occur in numerical prediction of heat flux, while it does not sacrifices the accuracy of the results significantly. The feature of the maximum entropy method without requiring evaluation of Hessian matrix was introduced, which is simple to implement. In cases that nonphysical solution is found, the combined strategy is able to deal with this problem and alleviate the difficulty associated with the design problem.

REFERENCES

1. Howell, J. R., Ezekoye, O. A., and Morales, J. C., 2000, "Inverse Design Model for Radiative Heat Transfer", *Journal of Heat Transfer*, Vol. 122, pp. 492–502.
2. Franca, F., Ezekoye, O. A., and Howell, J. R., 2001, "Inverse Boundary Design Combining Radiation and Convection Heat Transfer", *Journal of Heat Transfer*, Vol. 123, pp. 884–91.
3. Daun, K. J., and Howell, J. R., 2005, "Inverse Design Methods for Radiative Transfer Systems", *Journal of*

Quantitative Spectroscopy & Radiative Transfer, Vol. 93, pp. 43–60.
4. Daun, K., J., França, F., Larsen, M., Leduc, G., and Howell, J. R., 2006, "Comparison of Methods for Inverse Design of Radiant Enclosures", *Journal of Heat Transfer*, Vol. 128, pp. 269–282.
5. Porter, J. M., Larsen, M. E., Barnes, J. W., and Howell, J. R., 2006, "Metaheuristic Optimization of a Discrete Array of Radiant Heaters", *Journal of Heat Transfer*, Vol. 128, pp. 1031–1040.
6. Daun, K., J., Howell, J. R., and Morton, D. P., 2003, "Design of Radiant Enclosures Using Inverse and Non-Linear Programming Techniques", *Inverse Problems in Science and Engineering*, Vol. 11, No. 6, pp. 541–60.
7. Hosseini Sarvari, S. M., Mansouri, S. H., and Howell, J. R., 2003, "Inverse Design of Three-Dimensional Enclosures with Transparent and Absorbing–Emitting Media Using an Optimization Technique", *International Communications in Heat and Mass Transfer*, Vol. 30, pp. 149–162.
8. Hosseini Sarvari, S. M., Mansouri, S. H., and Howell, J. R., 2003, "Inverse Boundary Design Radiation Problem in Absorbing–Emitting Media with Irregular Geometry", *Numerical Heat Transfer, Part A,* Vol. 43, pp. 565–584.
9. Hosseini Sarvari, S. M., Howell, J. R., and Mansouri, S. H., 2003, "Inverse Boundary Design Conduction-Radiation Problem in Irregular Two-Dimensional Domains", *Numerical Heat Transfer, Part B*, Vol. 44, pp. 209–224.
10. Tito, M. J. B., Roberty, N. C., Neto, A. J. S., and Cabrejos, J. B., 2004, "Inverse Radiative Transfer Problems in Two-Dimensional Participating Media", *Inverse Problems in Science and Engineering*, Vol. 12, No. 1, pp. 103–121.
11. Kim, K. W., and Baek, S. W., 2006, "Inverse Radiation Design Problem in a Two-Dimensional Radiatively Active Cylindrical Medium Using Automatic Differentiation and Broyden Combined Update", *Numerical Heat Transfer, Part A*, Vol. 50, pp. 525–543.
12. Pourshaghaghy, A., Pooladvand, K., Kowsary, F., and Karimi-Zand, K., 2006, "An Inverse Radiation Boundary Design Problem for an Enclosure Filled with an Emitting, Absorbing, and Scattering Media", *International Communications in Heat and Mass Transfer*, Vol. 33, pp. 381–390.
13. Kowsary, F., Pourshaghaghy, A., and Pooladvand, K., 2007, "Regularized Variable Metric Method Versus the Conjugate Gradient Method in Solution of Radiative Boundary Design Problem", *Journal of Quantitative Spectroscopy & Radiative Transfer,* Vol. 108, pp. 277-294.
14. Rahmani, R. K., Koomullil, R. P., Cheng, G., and Ayasoufi, A., 2006, "Finite Volume Method for Non-Equilibrium Radiative Heat Transfer Using Generalized Grid", AIAA Paper-2006-3782, *9th AIAA/ASME Joint Thermophysics and Heat Transfer Conference*, San Francisco, CA.
15. Raithby, G. D., 1999, "Discussion of the Finite-Volume Method for Radiation, and its Application Using 3D Unstructured Meshes", *Numerical Heat Transfer, Part B*, Vol. 35, pp. 389-405.
16. Fiveland, W. A., 1984, "Discrete-Ordinates Solutions of the Radiation Transport Equation for Rectangular Enclosures", *Journal of Heat Transfer*, Vol. 106, pp. 699-706.
17. Coelho, P. J., and Carvalho, M. G., 1997, "Conservative Formulation of the Discrete Transfer Method", *Journal of Heat Transfer,* Vol. 119, pp. 118–28.
18. Molavi, H., Hakkaki-Fard, A., Pourshaghaghy, A., Molavi, M., and Rahmani, R. K., 2009, "Heat Flux Estimation in a Nonlinear Inverse Heat Conduction Problem with Moving Boundary", ASME Paper-HT2009-88501, *Proceedings of 2009 ASME Summer Heat Transfer Conference*, HT2009, San Francisco, Ca, USA.
19. Muniz, W.B., Ramos, F.M., and Velho, H.F.D., 2000, "Entropy- and Tikhonov-Based Regularization Techniques Applied to the Backwards Heat Equation", *Computers & Mathematics with Applications*, Vol. 40, pp. 1071-1084.
20. Kim, S.K., and Lee, W.I., 2002, "Solution of Inverse Heat Conduction Problems Using Maximum Entropy Method", *International Journal of Heat and Mass Transfer*, Vol. 45, pp. 381-391.
21. Kim, S.K., Jung, B. S., and Lee, W.I., 2007, "An Inverse Estimation of Surface Temperature Using the Maximum Entropy Method", *International Communications in Heat and Mass Transfer*, Vol. 34, pp. 37–44.
22. Wu, N., *The Maximum Entropy Method*, Springer–Verlag, 1997.
23. Modest, M. F., *Radiative Heat Transfer*, Series in Mechanical Engineering, McGraw Hill, New York, 1993.
24. Glynn, P., and Robinson, S. M., 1999, *Numerical Optimization*, Springer-Verlag, New York.
25. Erturk, H., Ezekoye, O. A., and Howell, J. R., 2002, "The Application of an Inverse Formulation in the Design of Boundary Conditions for Transient Radiating Enclosures", *Journal of Heat Transfer*, Vol. 124, pp. 1095–1102.

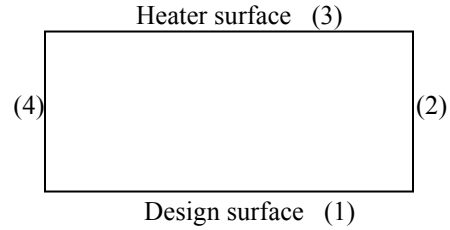

Figure 1: Example of a radiant enclosure design problem

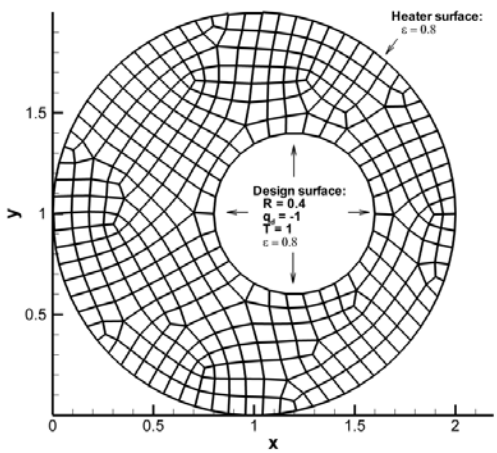

Figure 2: Geometry and boundary condition used in the first test case

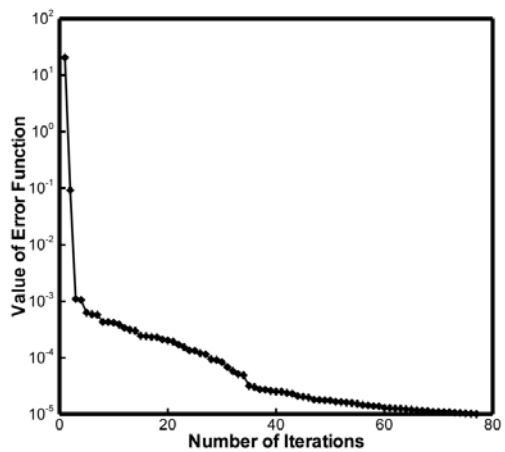

Figure 3: Reduction histories of the error function in the first test case

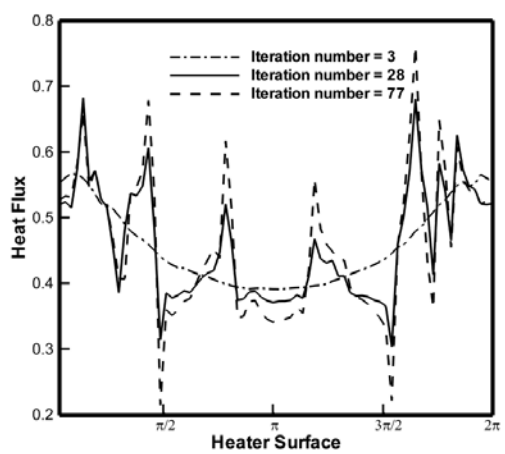

Figure 4: Heat flux profile over the heater surface for various iteration numbers

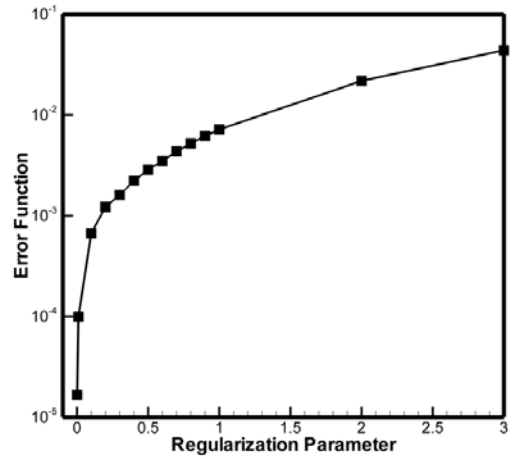

Figure 5: Error in estimated heat flux versus parameter α

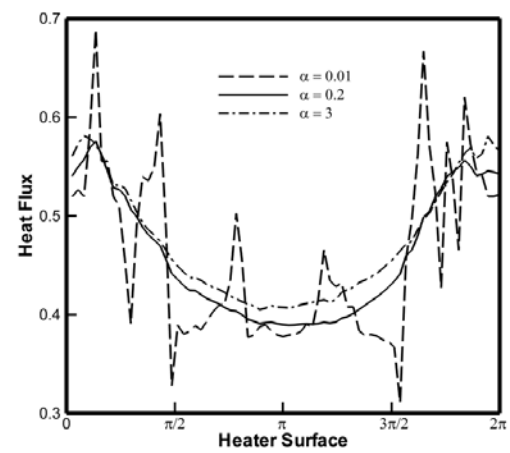

Figure 6: Profile of heat flux over the heater surface for various parameters α

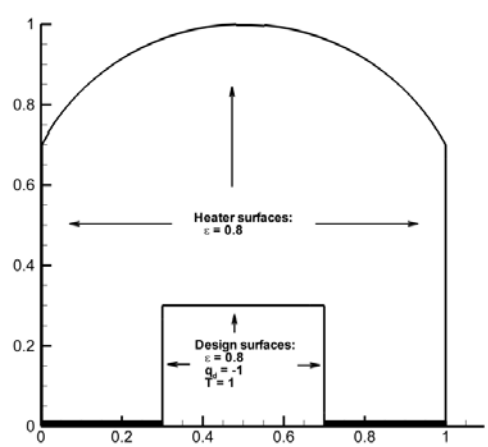

Figure 7: Geometry and boundary condition used in the second test case

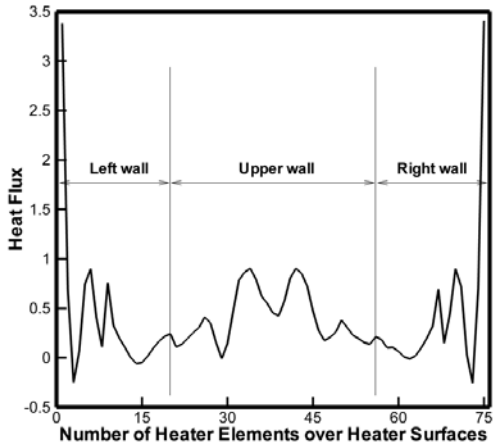

Figure 8: Heat flux distribution over the heater surface for the second test case

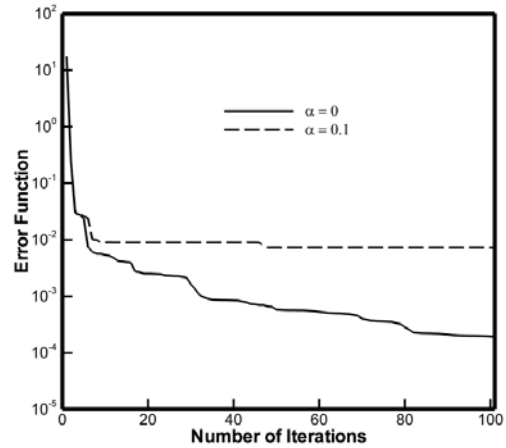

Figure 11: Reduction histories of the error function in the second test case

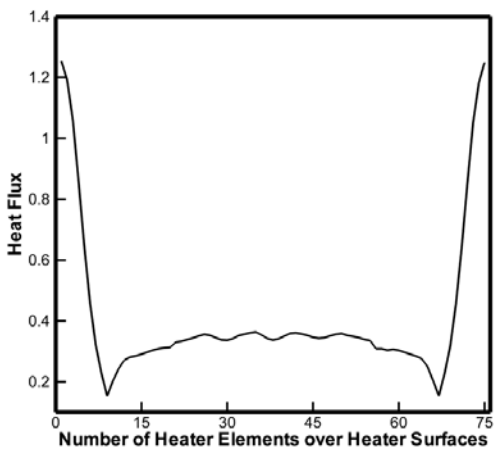

Figure 9: Profile of heat flux over the heater surface for parameters α=0.1

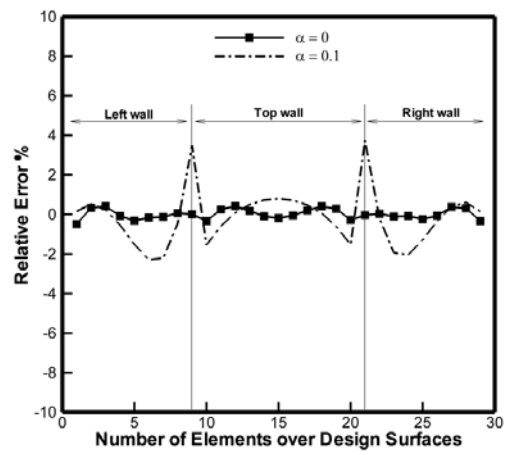

Figure 12: Relative errors between calculated and design heat fluxes

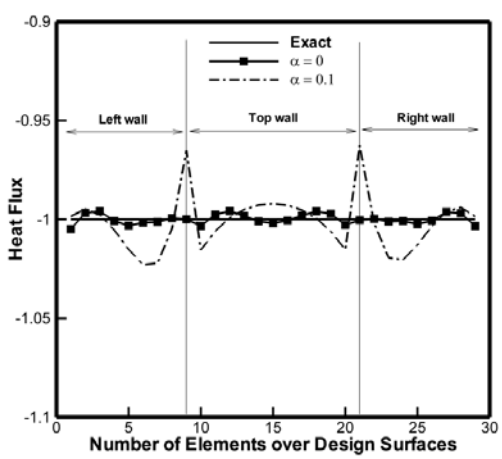

Figure 10: Comparison of the exact and the estimated heat fluxes over the design surfaces

ASME Early Career Technical Journal
2009 ASME Early Career Technical Conference, ASME ECTC
October 2-3, 2009, Tuscaloosa, Alabama, USA

FUTURISTIC PREDICTION OF LIFE AND FATIGUE PERFORMANCE OF A STEERING KNUCKLE

Kartik D. Kothari
Lecturer,
V.V.P. Engineering College,
Rajkot, Gujarat, India

Ramdevsinh L. Jhala
Asst. Professor and Head Of Department
V.V.P. Engineering College,
Rajkot, Gujarat, India

Dr.S.S.Khandare
Principal,
B.D. College of Engineering,
Varda, Maharashtra,India

ABSTRACT

The research criteria of the paper is to compare fatigue performance and assess fatigue life of steering knuckles made from three materials having different shapes of different manufacturing processes. By considering geometry variations, alternative materials and manufacturing process parameters as design variables, the part was optimized. These include forged steel, cast aluminum, and cast iron knuckles. The paper envisages that fatigue behavior is a key consideration in design and performance evaluation of steering knuckle, since it is subjected to repeated loading during its service life.

Forging process was considered as the base for investigation and other processes were compared to it, mainly due to the high volume of forged steel vehicle components. Strain-controlled monotonic and fatigue tests of specimens machined from the three knuckles were conducted. From these experiments, monotonic as well as baseline cyclic deformation and fatigue properties were obtained and are compared. In addition, a number of loads controlled fatigue component tests were conducted for the forged steel and cast aluminum knuckles. Finite element analysis of the steering knuckles was also conducted to obtain stress and strain distributions in each component. Based on the reference results of specimen testing and finite element analysis, life predictions were performed. Better fatigue resistance is offered from forged steel material in comparison to the two cast materials.

INTRODUCTION

A strong trend towards the adoption of optimum materials and components is there in automotive industry. Automotive designers have a wide range of materials and processes to select from; Steel forgings are in competition with aluminum forgings and castings, cast iron, and sintered powder forgings. The steering knuckle, being a part of the vehicle's suspension system, has alternatives of forging and casting as its base manufacturing process. Since it is connected to the steering parts and strut assembly from one side and the wheel hub assembly from the other, it has complex restraint and constraint conditions and tolerates a combination of loads.

In addition, parameters such as internal defects, stress concentrations and gradients, surface finish, and residual stresses can have considerable influence while designing for fatigue. A common practice of fatigue design consists of a combination of analysis and testing.

A problem that arises at the fatigue design stage of components is the transferability of data from smooth specimens to the component. The component geometry and surface specifications often deviate from that of the specimen investigated and neither a nominal stress nor a notch factor can be defined in most cases.

A methodology was developed to quantitatively assess fatigue lives of automotive structures and to identify critical and non-damaging areas for design enhancement and weight reduction. The methodology combines load-time history file with results from elastic FEA to estimate fatigue lives. Knuckle strain gage measurements were made for elastic as well as inelastic load ranges.

The correlations of maximum principal strains between the FEA and the experimental results showed average errors of 23% and 27% for lateral and fore/aft loads in elastic range, respectively. The differences between observed and predicted lives in the inelastic range were found to be factors of 3.9 and 1.4 at the R50C50 life (the fatigue life with reliability

of 50% and confidence level of 50%) for fore/aft and lateral loading tests, respectively. To perform fatigue analysis and implement the local stress-strain approach in complex vehicular structures, used strain-life results simulated 3-D stress-strain models and multiaxial deformation paths to assess fatigue damage. After the complex load history was reduced to a uniaxial (elastic) stress history for each critical element, a Neuber plasticity correction method was used to correct for plastic behavior. Elastic unit load analysis, using strength of material and an elastic FEA model combined with a superposition procedure of each load point's service history was proposed. These include mean stress effects, load sequence effects above and below the endurance limit, and manufacturing process effects such as surface roughness and residual stresses.

S-N curves under constant amplitude loading and strain-life curves under variable amplitude loading for unnotched and notched specimens and components were compared. It was concluded that the same failure criterion (i.e. first detectable crack), accurate determination of the local equivalent stress or strain, and the same maximum stressed/strained material volume for both the specimens and the components, were preconditions for the transferability of material data obtained from specimens to the component. The maximum stressed/strained material volume appeared to be suitable for taking into account the statistical and mechanical size effects in a relatively simple manner. The objectives of the current study were to compare fatigue performance and assess fatigue life for steering knuckle, a fatigue critical part, made from three materials of different manufacturing processes. Knuckles of three vehicles were selected. These included forged steel knuckle of the rear suspension of a *Maruti 800,* cast aluminum knuckle of front suspension of *Mahindra Scorpio*, and cast iron knuckle of the front suspension of a *Maruti Omni*. Only the forged steel knuckle included the spindle portion. Figure 1 shows the digitized models of the three components.

(a) (b) (c)

Figure 1 Model Of The (a)Forged Steel, (b) Cast Aluminum And (c) Cast Iron Steering Knuckles Created In Pro Engineer

COMPARISON OF DURABILITY AND FATIGUE BEHAVIORS FOR STEERING KNUCKLE

Manufacturing process, such as forging or casting, generally determines the strength level and scatter of mechanical properties, but the geometry can suppress the influence of the material. For a complex component geometry where no notch factors could be defined, transferability of material test data could be performed only through local equivalent stresses or strains in the failure critical areas. In this study, the local equivalent stresses and strains corresponding to the experimental loading conditions were obtained by applying equivalent loads to the simulated finite element models. Since the tests were conducted with a mean load, the modified Goodman equation was used to account for the effect of mean stress:

$$\frac{\sigma_a}{\sigma_{Nf}} + \frac{\sigma_m}{S_u} = 1 \qquad (1)$$

Where σ_a, σ_{nf}, σ_m and S_u are alternating stress in the presence of mean stress, alternating stress for equivalent completely reversed loading, mean stress, and ultimate tensile strength, respectively.

The Basquin equation was then used to obtain the fatigue life using the material properties:

$$\sigma_{Nf} = \sigma'_f (2N_f)^b \qquad (2)$$

Normally, a surface finish reduction factor is applied to the fatigue strength of a component. However, the fillet of the forged steel knuckle was machined and polished and, therefore, no surface finish factor was applied. For the two cast knuckles, due to the nature of the casting materials and the fact that the defects of a casting material is uniform internally and externally, no surface finish factor was implemented either. In the strain-life approach, the local values of stress and strain at the critical location were used to find fatigue life, according to the Smith-Watson-Topper (SWT) parameter that considers the mean stress effect:

$$\sigma_{max}\, \varepsilon_a E = (\sigma'_f)^2 (2N_f)^{2b} + \sigma'_f \varepsilon'_f E (2N_f)^{b+c} \qquad (3)$$

Where σ_{max} is the maximum stress ($\sigma_{max} = \sigma_a + \sigma_m$) and ε_a is the strain amplitude.

FEA OF STEERING KNUCKLE

The objective of the stress analysis was to obtain the complete three dimensional stress and strain distributions at a potential failure site, facilitating fatigue life predictions. Depending on the method of fatigue life prediction, stress analysis can be linear or nonlinear. Linear elastic analysis is the most common type of stress analysis pursued in automotive design and analysis. The majority of automobile engine components like camshaft, crankshaft and connecting rod operate within the material elastic region, and therefore linear elastic analysis is feasible to model their behavior. On the other hand, most components in chassis and suspension undergo occasional overloads in service and cyclic plasticity becomes a major factor to define their stress-strain response, particularly at stress

concentrations. In these cases linear analysis is not sufficient to analyze component's behavior and nonlinear elastic-plastic analysis should be performed. Although in this study the components underwent unidirectional loading condition, the state of stress at many locations was found to be multiaxial. In addition, gross yielding existed for a number of experimental applied moment cases. Therefore, both linear finite element analysis (FEA) to be used along with a stress/strain correction method, and nonlinear FEA to directly estimate elastic-plastic distributions of stress and strain were performed. Pro Mechanica FEA program and its help library bookshelf were employed for the analysis.

Linear and nonlinear static finite element analyses employing Pro Mechanica software were conducted on each knuckle. Nonlinear analysis was necessary due to local yielding in most cases, as well as gross yielding in some cases, as mentioned previously. In order to generate precise geometries of the three steering knuckles, a Coordinate Measuring Machine (CMM) was used, with the resulting digitized models as presented in Figure 1. Details of the FEA are discussed in this paper.

COMPONENT GEOMETRY GENERATION

The geometries of components were generated as solid parts using a coordinate measuring machine and the modeler tools of the software. The resulting solid models are presented in Figure 1. The weights of the generated models were 2.35 kg, 2.38 kg and 4.62 kg versus the actual components weight of 2.4 kg, 2.4 kg and 4.7 kg for the forged steel, cast aluminum and cast iron steering knuckles, respectively. These show differences of 2%, 1 % and 2 %, respectively, and verify the accuracy of the geometries generated for analysis. The fillets and chamfers of the components were removed (except at the critical locations as sighted in figure 2) in the models used for the analysis in order to reduce the complexity of the models and the runtime.

MODEL BOUNDARY CONDITIONS

The boundary conditions and loading were selected to represent the assumed component testing conditions. To verify the model with the specified boundary conditions other alternatives were analyzed by switching the loading and boundary conditions and also by releasing any one of the fixed points to ensure the critical locations remained the same.

For the cast aluminum steering knuckle in service while the loading is applied to the strut joints through struts, the four hub bolt holes are connected to the wheel assembly. Several trials for boundary conditions were analyzed including fixing the whole area of the four hub bolt holes, fixing the centerline of the hub bolt holes, only fixing the pair of bolt holes away from the load application point, and fixing two points at the middle area of the hub. It was found that except for the case of fixing the whole area of the bolt holes, all the other three cases provided approximately similar results at the critical location. This critical location was the node at the area that the crack initiated during component testing. Moreover, the strain readings from strain gages were reasonably close to the strain values for these three options are discussed. The option to fix the whole area of the bolt hole resulted in lower value of stress at the node of this critical location and the highest stresses occurred at a different location. In addition, for this option the strain value at the location where strain gage was installed was different from the strain gage reading.

Based on these two observations, the choice of fixing the hub bolt hole-centerlines was selected as the base boundary condition case for the cast aluminum steering knuckle. For the cast iron steering knuckle, where the geometry and service conditions were close to the cast aluminum steering knuckle, similar loading and boundary conditions were applied.

MESHING OF THE FINITE ELEMENT MODELS

To generate the mesh for the components, free meshing feature of the software was employed since it has no geometry restrictions and it could be defined on complicated volumes. The free mesh generator uses an algorithm that minimizes element distortion. Three-dimensional linear tetrahedron solid elements with three translational degrees of Freedom were used. Although parabolic element offers more accurate results, the analysis time, especially for nonlinear analysis, is immensely more than that of linear elements.

Nonlinear analysis at the highest moment level with parabolic elements showed negligible difference in results with those using linear tetrahedral element and, therefore, the linear element was selected for modeling. For the complex three-dimensional geometry of the steering knuckles, solid element offers more accurate results and Pro Mechanica software employs tetrahedron solid elements. In spite of a global mesh size for each component, free local meshing feature was used to increase the number of elements at the vicinity of the critical points.

Convergence of stress and strain energy was considered as the criteria to select the mesh size. Too much refinement at the critical points would result in extremely lengthy analysis time and was, therefore, avoided. Figure 2 shows the variation of stress at the critical points of each steering knuckle. Global mesh size of 5.1 mm for the forged steel and cast aluminum steering knuckles and 3.8 mm for the cast iron steering knuckle and local mesh size of 0.1 mm for the forged steel and 0.64 mm for the cast aluminum and cast iron steering knuckles were specified. The critically-stressed locations were spindle fillets for the forged steel, and hub bolt-holes for the cast aluminum and cast iron steering knuckles. Due to higher stress concentration at the spindle fillet of the forged steel steering knuckle, large stress gradient existed at this location, and therefore, more refined mesh size was implemented. As another verification of convergence of the mesh, the averaged and unvaried stress values at the critical nodes were confirmed to be approximately equal.

Figure 2 shows the three meshed components with the darker areas representing those with higher mesh density. Adaptive meshing module as a tool to improve a mesh by

moving nodes, splitting elements, or remeshing the model, was examined. The software derives the new mesh by analyzing the data variation along the boundaries and within the interior regions of the faces. Adaptive meshing could be used to reduce elemental distortion or refine a mesh in areas where error estimates are highest. Energy error norm is used as basis for the adaptive meshing method. The energy error norm (EEN) is based on the strain energy error. It is computed from the elemental strain energy errors and the model's total strain energy from Zienkiewicz-Zhu parameter (Pro Mechanica Help):

$$\text{Energy error norm} = \sqrt{\left[\frac{\sum \text{elemental strain energy errors}}{\text{total strain energy}}\right]} \times 100$$

where the summation is over the entire volume of the component.

The Convergence is determined by comparing EEN in the model to the EEN specified. For the forged steel steering knuckle with an initial mesh size of 5.08 mm, EEN was calculated to be 10.7%. Remeshing option of adaptive meshing that increases the number of elements at the areas with high strain energy error was applied and the first adaptive trial resulted in EEN equal to 7.9%. No more adaptive meshing was possible due to high distortion of the newly generated elements. This is attributed to the geometric complexity of the component. The component's appropriate loading and boundary conditions were applied to the refined model and the results were compared to the results from the converged mesh using free local meshing, where they were found not to be equal.

In addition, the averaged and unaveraged stress and strain results for the adaptive-meshed model were compared and they were not equal either. These show that the mesh did not converge. As a result, the final meshed models used for solution were those with free local meshing and the adaptive meshing tool was found not to be suitable for the components.

MATERIAL NONLINEAR BEHAVIOR MODELS

To define the limit of elastic behavior in nonlinear analysis, von Mises yield criterion was assumed, using an associated flow rule in which the plastic potential function is the same as the yield function and the components of the plastic strain increment are given by a Prandtl-Reuss type equation. Ziegler-Prager kinematic hardening rule was selected, for which a bilinear stress-strain curve of the material is assumed. The appropriate portion of the materials cyclic stress-strain curve was used to define material properties for each cyclic moment level; i.e. for each applied cyclic moment level, a slope for the second line of the bilinear model was assumed and the stress and strain results were obtained from FEA. This slope was found by trail and error in an iterative process until the resultant stress-strain point matched the experimental material cyclic stress-strain curve. The actual cyclic stress-strain curves at different cyclic moment levels including the values of stress and strain at the critical points of failure at each level obtained from FEA also superimposed. It was observed that the assumed model provides stress/strain values in the component with a reasonable error of less than 10% with respect to the actual material stress-strain curve. Note that even at the lower moment level, which can be considered as an indication of long-life service of the components, the material undergoes local plastic deformation. This is evidence that mere use of linear elastic FEA is not sufficient for reliable fatigue life predictions.

MODEL SOLUTIONS

The model solution equation solver for linear or nonlinear analysis creates a set of simultaneous linear equations that must be solved. For instance, the number of equations created for the highest load level of the forged steel steering knuckle model with 4245 nodes and 19098 elements was 12570 equations. The direct method is represented by Gaussian elimination along with Choleski decomposition or factorization method. With Choleski decomposition, the matrix of equations is factorized into a lower triangular, diagonal, and upper triangular matrix; the upper triangular matrix is the transpose of the lower triangular matrix. After factorization, the equations are solved for the unknown values by performing a forward and backward substitution upon the load vector. Following decomposition of the stiffness matrix, the displacements are calculated and strain and stresses are obtained.

A nonlinear solution proceeds incrementally with equilibrium iterations performed at every solution point. The stiffness matrix in the nonlinear solution does not participate in the equilibrium statement as is the case in linear analysis. The stiffness relates incremental displacements to incremental forces. The software computes tangent stiffness based on current geometry, stress, and plastic strain. Then it computes applied loads based on current configuration, and computes internal force based on current displacements and plastic strains. In the next step, it computes force residual, computes displacement increment, updates displacements, computes plastic strain increments at element integration points, and checks for convergence. Energy convergence ratio is the convergence criterion that uses both displacements and forces. The amount of work done by the residual forces in the ith iteration is compared with the first iteration (Pro Mechanica Help). As an example, the nonlinear solution for the highest load level of the forged steel steering knuckle took four iterations to converge.

ANALYSIS OF THE RESULTS

The finite element models were solved for loading and unloading under the assumed component testing conditions with the assumed moment levels. The procedure used to obtain maximum and minimum stresses and strains in a loading cycle is as follows; first, loading was applied to the FEA model at the maximum moment assumed to be used in the test and von Mises stress at the critical location was obtained (σ_{VMmax}). Then the moment range assumed to be used in the experiment was

applied to the FEA model and von Mises stress range at the same critical location was obtained ($\Delta\sigma_{VM}$). It should be noted that when using the maximum moment, the stress-strain relation used was the material cyclic curve based on amplitudes, whereas when using the moment range, the cyclic stress-strain curve was based on ranges (i.e. equation of the hysteresis loop). Having σ_{VMmax} and $\Delta\sigma_{VM}$, the range and mean values of stresses and strains were then calculated. Figure 2 shows contours of Von Mises stress for the maximum moment level of 1515 N.m for forged steel and 2230 N.m for cast aluminum and cast iron steering knuckles. For the forged steel and cast aluminum steering knuckles at the higher moment levels, yielding occurred both gross (at the spindle and the hub, respectively) and locally (at the fillet and hub bolt-holes, respectively), whereas for the cast iron steering knuckle only local yielding occurred at the critical points (hub bolt-hole). The contours of stress and strain at the lower moment levels were different, showing only local plastic deformation. In this case, the spindle and the hub area for the forged steel and cast aluminum steering knuckles undergo elastic deformation.

The x, y and z components, principal and equivalent von Mises values of stress and strain for the three components at the critical locations for the highest moment level applied in the analysis. The z direction aligns with the spindle axis for the forged steel steering knuckle, and the y and x directions align with the strut arm for the cast aluminum and cast iron steering knuckles, respectively. The spindle 1st step fillet area for the forged steel and hub bolt hole for the cast aluminum and cast iron steering knuckles were found to be the high-stressed locations with high stress gradient. The effect of stress concentration can be seen by showing the distribution of local stress at the spindle 2nd step fillet and nominal stress at a cross section remote from the fillet for the maximum moment level of 1515 N.m. For spindle radius smaller than 10 mm the material behavior is elastic, while for larger radii it becomes inelastic. The variation of stress at different locations of the forged steel steering knuckle with respect to moment steps to provide a comparison between the level of stress at the critical location and other locations is plotted.

The stress concentration produced by a notch depends on the mode of loading applied to the component. Not only the stress concentration at the fillet of the forged steel steering knuckle increases the stress level, but also the stress gradient is higher than, for instance, tension loading due to the loading mode (bending). Examining the data clearly demonstrates the multiaxial nature of stress and strain at the critical locations, although the primary loading on the components are unidirectional. The ratio of σ_y/σ_z in the case of the forged steel steering knuckle is 0.36, σ_x/σ_y for the cast aluminum steering knuckle is 0.69, and τ_{yz}/τ_{xy} is -0.36 for the case of the cast iron steering knuckle. Therefore, equivalent values of stress and strain should be calculated to account for multi axiality. Since the stresses and strains obtained form these analyses were used to predict fatigue life, the proportionality of stresses is also an important issue for selection of an appropriate fatigue life prediction model. Only one source of load exists for the primary loading that these components undergo, therefore the stresses are proportional throughout the components, i.e. the stresses increase and decrease in-phase as the primary loads increase and decrease, respectively. For proportional stressing, von Mises stress and strain have been found effective in calculating the equivalent values as a result of multi axiality (Stephens et al., 2000), and were used for subsequent fatigue life analyses.

Another observation that could be made from these data is the stress state at the critical locations. The values of σ_2/σ_1 for the critical locations are 0.36, 0.12 and 0.06 while the values of $\varepsilon_2/\varepsilon_1$ are -0.09, -0.35 and -0.13 for the forged steel, cast aluminum and cast iron steering knuckles. This indicates that at the critical location, the state of nearly plane strain prevails for the forged steel steering knuckle, while the state of stress at the critical locations of the cast aluminum and cast iron steering knuckles is closer to plane stress. Slightly different results were obtained for lower moment levels due to limited plastic deformation, but the same conclusion about the state of stress could be drawn for them too.

An important point for the fatigue analysis to be mentioned here is the effect of the notch on local stresses and strains due to cycling. Cyclic loading generates residual stress at the notch and therefore, makes the local deformation behavior different from the nominal behavior. The nominal moment ratios and local stress ratios as results of loading and unloading simulations of the components. As the nominal R-ratio remains almost constant (close to zero), significant negative R-ratio is observed for most of the simulations as a result of the residual stress generated at the stress concentrations (i.e. critical locations). This phenomenon is more pronounced at the higher moment levels, as expected, because of increased plastic deformation and nonlinear material behavior.

Von mises yield criterion and a kinematics hardening rule that used a bilinear stress-strain curve, adequately representing the material cyclic deformation behavior, were assumed for the nonlinear analysis. The boundary conditions and loading were selected to represent the component service and testing conditions. For the forged steel knuckle, the primary loading was applied to the spindle, and the four suspension and strut holes were restrained.

The analysis showed that changing the location in the spindle length at which the load is applied does not affect the location and magnitude of the stresses at the critical point. To verify the model, other alternatives were analyzed by switching the loading and boundary conditions, and also by releasing any one of the fixed points, to ensure the critical locations remained the same. For the cast aluminum knuckle in service, while the loading is applied to the strut joints through struts, the four hub bolt holes are connected to the wheel assembly.

Several trials for boundary conditions were analyzed, including fixing the whole area of the four hub bolt holes, fixing the centerline of the hub bolt holes, only fixing the pair

of bolt holes away from the load application point, and fixing two points at the middle area of the hub. It was found that except for the case of fixing the bolt holes, for which the value of stress was lower and the critical location was different, all the other three cases provided approximately similar results.

Therefore, the choice of fixing the hub bolt hole-centerlines was selected. For the cast iron knuckle, where the geometry and service conditions are close to the cast aluminum knuckle, similar loading and boundary conditions were applied. While defining a solid mesh for the components, auto meshing feature of the software was employed since it has no geometry restrictions and it could be defined on complicated volumes.

The auto mesh generator used an algorithm that minimizes element distortion. 3-D linear tetrahedral solid elements, with global element sizes of 3.81 mm for the forged steel and cast iron knuckles and 5.08 mm for the cast aluminum knuckle were used. Local element sizes of 0.254 mm for the forged steel and 0.635 mm for the cast aluminum and cast iron knuckles were considered at the critical locations (i.e. spindle fillets for forged steel knuckle, and hub bolt holes for cast aluminum and cast iron knuckles). These mesh sizes were obtained based on the convergence of stress and strain energy at certain geometry locations.

A potential source of significant error in fatigue analysis is inaccuracy of stress and strain predictions. Therefore validating the FEA models was critical to this study. To validate the models, values of strains as measured by strain gages in component testing and as predicted using the finite element analysis were compared and are listed in Table 1. The strain gages for the forged steel knuckle were positioned at the vicinity of the spindle root and the first step fillets, and for the cast aluminum knuckle two gages were positioned at the goose neck of the strut arm and two at the hub bolt holes where the crack initiation was observed during component testing. These locations are identified in Table 1. Depending on the location of the gage, the proper component of the strain obtained from the FE analysis was selected for comparison. The differences between measured and predicted strains obtained for the two knuckles were considered reasonable for the complex knuckle geometries. For the forged steel knuckle, which has a relatively simpler geometry, results of strain calculations from analytical mechanics of materials equation are also listed in Table 1. As can be seen, these results are mostly in between the measured and FEA-predicted strains. The results of the finite element analysis were also checked with regards to symmetry and linearity of the loading in the elastic range. It should be noted that the position of the strain gages and the magnitudes of the applied loads were such that all measured strains were in the elastic range.

Table 1 Values Of Strains As Measured By Strain Gages In Component Testing And Values Predicted Using The FEA With Their Figures

Gage Number	Measured Strain	P/A +Mc/I	Predicted Strain from FEA	Difference in Strain(%)
Forged Steel				
1	545	580	591	8.5
2	-529	-560	-549	4.0
3	1566	1576	1718	10
4	-1485	-1539	-1597	8.0

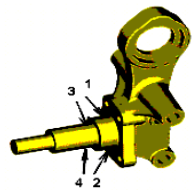

Forged Steel Knuckle

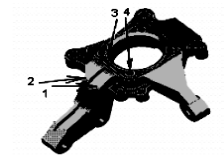

Cast Aluminum Knuckle

Gage Number	Measured Strain	P/A +Mc/I	Predicted Strain from FEA	Difference in Strain(%)
Cast Aluminum				
1	459	----	438	5.0
2	533	----	476	11.0
3	232	----	269	16.0
4	295	----	326	10.5

The equivalent Von mises stress contours and critical locations for a typical load value are presented for the three models in Figure 2. The spindle 1st step fillet area for the forged steel knuckle, the hub bolt holes for the cast aluminum knuckle, and the strut arm root and hub bolt hole for the cast iron knuckle, were found to be the areas of high stresses. Von mises equivalent stresses and strains are used for subsequent fatigue life analysis and comparisons.

For the forged steel knuckle, at the highest experimental load level yielding occurred both gross (in the spindle) and locally (at the fillet), whereas for the cast aluminum knuckle at the highest experimental load only local yielding (at the hub bolt hole) occurred.

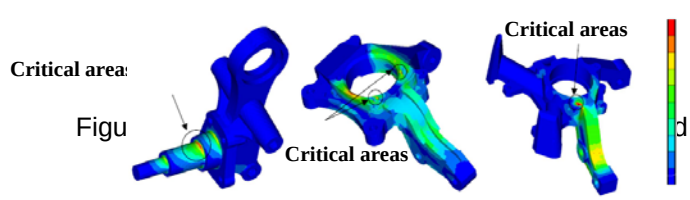

Figu

CONCLUSIONS

Based on the analyses presented for a steering knuckle, the following conclusions can be made:

1. Better S-N fatigue resistance of the forged steel was observed, as compared with the two cast materials. Long-life fatigue strengths of cast aluminum and cast iron are only 35% and 72% of the forged steel, respectively.

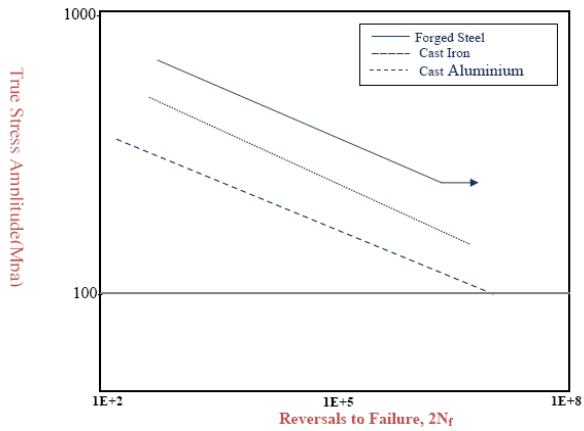

Figure 3 S – N Curves for Three Materials

2. The cyclic yield strength of cast aluminum and cast iron were found to be 54% and 75% of forged steel, respectively, while the cyclic strain hardening exponent of cast aluminum and cast iron were 46% and 55% of the forged steel, respectively. These indicate higher resistance of the forged steel to cyclic plastic deformation.
3. The differences between measured and FEA predicted strains obtained for the forged steel and cast aluminum knuckles were found to be reasonable for the complex knuckle geometries considered.
4. The S-N predictions were overly conservative, whereas strain comparison of the strain-life prediction curves of the components demonstrated that the forged steel knuckle offers more than an order of magnitude longer life than the cast iron knuckle.
5. In the high-cycle period, forged steel resulted in about an order of magnitude longer life than the cast iron, and about a factor of 3 longer lives, compared to the cast aluminum.

REFERENCES

[1] Design of Machine Elements by V.B. Bhandari
[2] Machine Design by Joseph Shigley
[3] Design of Machine Elements by Dr. Abdul Mubeen
[4] Finite Element Analysis by Chandrapatula
[5] Gunnarson, S., Ravenshorst, H., and Bergstorm, C. M., “Experience with Forged Automotive Components in Precipitation Hardened Pearlitic- Ferritic Steels,” Fundamentals of Micro alloying Forging Steels, Proceedings, Metallurgical Society of AIME, 1987, pp. 325-338.
[6] Lee, S. B., “Structural Fatigue Tests of Automobile Components under Constant Amplitude Loadings,” Fatigue Life Analysis and Prediction, Proceedings, International Conference and Exposition on Fatigue, Goel, V. S., Ed., American Society of Metals, 1986, pp. 177-186.
[7] Lee, Y. L., Raymond, M. N., and Villaire, M. A., “Durability Design Process of a Vehicle Suspension Component,” Journal of Testing and Evaluation, Vol. 23, 1995, pp. 354-363.
[8] Beranger, A. S., Berard, J. Y., and Vittori, J. F., “A Fatigue Life Assessment Methodology for Automotive Components,” Fatigue Design of Components, ESIS Publication 22, Proceedings of the Second International Symposium on Fatigue Design, FD’95, 5-8 September, 1995, Helsinki, Finland, Marquis, G., Solin, J., Eds., 1997, pp. 17- 25.
[9] Conle, F. A. and Chu, C. C., “Fatigue Analysis and the Local Stress-Strain Approach in Complex Vehicular Structures,” International Journal of Fatigue, Vol. 19, No. 1, 1997, pp. S317-S323.
[10] Savaidis, G., “Analysis of Fatigue Behavior of a Vehicle Axle Steering Arm Based on Local Stresses and Strains,” Material wissenschaft und Werkstoff technik, Vol. 32, No. 4, 2001, pp. 362, 368.
[11] Sonsino, C. M., Kaufmann, H., and Grubisic, V., “Transferability of Material Data for the Example of a Randomly Loaded Forged Truck Stub Axle,” SAE Technical Paper No. 970708 in SAE PT-67, Recent Developments in Fatigue Technology, Chernenkoff, R. A., Bonnen, J. J., Eds., Society of Automotive Engineers, 1997.
[12] ASTM Standard E606-92, "Standard Practice for Strain-Controlled Fatigue Testing," Annual Book of ASTM Standards, Vol. 03.01, 1998.
[13] ASTM Standard E8-03, "Standard Test Methods for Tension Testing of Metallic Materials," Annual Book of ASTM Standards, Vol. 03.01, 2003.
[14] Kothari K. D. 2009, “Dynamic Simulation and optimization for a dynamically loaded crankshaft of a Single cylinder I.C. Engine”, Dissertation report - Saurashtra University, Rajkot.

ASME Early Career Technical Journal
2009 ASME Early Career Technical Conference, ASME ECTC
October 2-3, 2009, Tuscaloosa, Alabama, USA

NUMERICAL SIMULATION OF TRANSIENT RADIATIVE HEAT TRANSFER APPLYING FINITE VOLUME METHOD ON GENERALIZED COMPUTATIONAL GRID

Ramin K. Rahmani, Anahita Ayasoufi
Affiliate Research Scholar
MIME Department
The University of Toledo
Toledo, Ohio, USA

Hosein Molavi
Researcher
Department of Mechanical Engineering
Tarbiat Modares University
Tehran, Tehran, Iran

ABSTRACT
The ability to predict transient radiant energy transfer is required in order to understand the heating phenomena associated with the short pulse laser, which has applications in material processing, particle detection and sizing, remote sensing, biomedical engineering, etc. It is desired to develop a stand-alone numerical module for transient radiative heat transfer that can be easily incorporated in existing CFD codes. The Finite Volume Method (FVM) is one of the most popular approaches to be employed by a numerical flow solver to predict radiative heat transfer in emitting-absorbing-scattering media. In this paper a FVM method for predicting transient radiative heat transfer using generalized computational grid is presented. A novel method to overcome overhang problem associated with non-orthogonal grids is presented. The numerical approach is validated using some benchmarks and is shown to be capable of producing accurate results.

INTRODUCTION
There are several applications of steady state radiative heat transfer in participating media such as heat transfer through porous materials, combustion chambers, rocket nozzles, exhaust plumes, steam generators, solar-energy utilization, cloudy atmosphere, and reentry vehicles. The transient term of Radiative Transfer Equation (RTE) can be ignored in those studies. Numerical solution of steady RTE has received an enormous amount of attention in the past decades, since it is a practical approach for real complex geometries and conditions. Among several numerical methods, five methods (and their variations) have became more popular than the others: Zone method [1], Monte Carlo method [2], Spherical harmonics methods (Approximate PN methods) [3], Discrete Ordinates Method (DOM) [4], and Finite Volume Method (FVM) [5,6]. A review of these methods can be found in [7].

On the other hand, recent advances in the ultra short pulse laser have led to emerging areas that neglecting the transient term of RTE is not acceptable. Ultra short pulse laser has applications in thin film property measurements, material processing, particle detection and sizing, remote sensing, micro-machining, optical data storage, optical ablation, biomedical engineering, etc. [8,9]. Optical tomography, X-ray computed tomography, and magnetic resonance imaging, are among the applications that can employ short pulse laser, which is believed to be superior to traditional imaging techniques [9]. In such situations, the variation of radiative intensity within the length scale of the radiative transport per unit time is comparable to the variation over the length scale of the medium, or the time scale of the internal or external disturbance to the radiative field is comparable to the time scale of the radiation transport within the medium. Under such circumstances, the transient effect of radiative transfer must be considered [10].

Several studies have been conducted on the Transient Radiative Transfer Equation (TRTE) for different problems in the recent years [8-17]. The majority of previous work on transient radiative heat transfer considered a one-dimensional slab or a two-dimensional rectangular. In practice, several cases have three-dimensional geometry with non-homogeneous radiative property distribution. In this paper, transient radiative heat transfer in three-dimensional geometry with non-homogeneous absorbing and scattering medium is studied numerically.

Although FVM approach has been used to solve RTE in several cases, it has not received adequate attention, when it comes to TRTE. FVM is fully conservative. Analytical integration ensures exact satisfaction of all full moment conditions. There is also no loss of scattered radiation. Another attractive feature of FVM is that it shares the same computational grid as the CFD approach for the spatial domain; thus, the method can conceptually be applied with the same orthogonal or non-orthogonal computational grids used to compute fluid flow and convective heat transfer. There is no restriction on discretization of the angular domain and uniformity of the control angles. The ray effect can be easily removed, using FVM approach. However, FVM may converge slowly when applied to the optically thick medium. To be able

to implement FVM to a non-orthogonal grid (which is widely used in CFD applications), a problem called "overhanging" needs to be resolved. In this paper, a numerical method based on FVM approach that can be employed by a CFD solver with generalized computational mesh is developed, which resolves the overhanging issue with no approximation and with very low computational cost. The method is applied to three-dimensional steady and transient benchmark test cases and it is shown that the method is capable of producing accurate results.

NOMENCLATURE

A	=	area vector
a	=	blackbody weight
c	=	speed of light
E_b	=	blackbody emissive flux
I	=	intensity
I_b	=	blackbody intensity
I_{if}	=	intensity associated with the direction i at the face of the control volume
I_{i0}	=	intensity at the control volume in the direction i
J_f	=	a geometric factor defined in Eq. (7)
L	=	path-length
L_0	=	dimensional scale
q	=	radiative heat flux
$\hat{r}$	=	position vector
s	=	coordinate along the ray
$\hat{s}$	=	direction vector
S	=	source term
t	=	time
T	=	temperature
ΔV	=	volume of control angle
θ	=	polar angle
κ	=	absorption coefficient
σ	=	Stefan-Boltzmann constant
σ_s	=	scattering coefficient
ϕ	=	azimuthal angle
Φ	=	scattering phase function
Ω, Ω'	=	control angle direction

ANALYSIS

Consider the TRTE in a Cartesian coordinate system as shown in Fig. 1. The TRTE for a gray absorbing, emitting, and scattering gas in the direction s may be written as

$$\frac{1}{c}\frac{\partial I(\hat{r},\hat{s},t)}{\partial t}+\frac{\partial I(\hat{r},\hat{s},t)}{\partial s}=-\left[\kappa(\hat{r})+\sigma_s(\hat{r})\right]I(\hat{r},\hat{s},t)+S(\hat{r},\hat{s},t) \quad (1)$$

In this equation, I is the radiant intensity, κ is the absorption coefficient, σ_s is the scattering coefficient. The source term S is given by

$$S(\hat{r},\hat{s},t)=\kappa(\hat{r})I_b(\hat{r},t)+\frac{\sigma_s(\hat{r})}{4\pi}\int_{4\pi}I(\hat{r},s',t)\Phi(s',s)d\Omega' \quad (2)$$

where $\hat{r}$ is position vector and $\hat{s}$ is ray direction vector; I_b is the blackbody intensity and Φ is the scattering phase function. Ω is the incoming direction, Ω' is the outgoing direction. This equation needs to be solved for all directions.

NUMERICAL METHOD

To solve TRTE, two computational domains need to be discretized: The spatial domain and the directional domain. The computational spatial domain is discretized into arbitrary unstructured convex polyhedra. The cell $C0$, in Fig. 2, is simply treated as a polyhedron with faces a-b-c-d. All unknowns are stored at cell centers. The angular space 4π steradians (directional domain) at any spatial location is discretized into discrete non-overlapping solid angles ω_i, the centroids of which are denoted by the direction vector s_i. Though the discretization of angular space can in principle be unstructured, in this study a structured discretization was adopted. The quantities (θ_i,ϕ_i) denote the polar and azimuthal angles associated with the centriod ω_i; the extends are given by $\Delta\theta$ and $\Delta\phi$. Since $\hat{s}$ is constant, Eq. (1) may be written as

$$\frac{1}{c}\frac{\partial I}{\partial t}+\frac{\partial I}{\partial x_i}s_i=-\left[\kappa(\hat{r})+\sigma_s(\hat{r})\right]I(\hat{r},\hat{s},t)+S(\hat{r},\hat{s},t) \quad (3)$$

If in Eq. (3), $\partial I/\partial t$ is insignificant compared to the speed of light, this equation can be simplified to steady RTE. TRTE should considered in cases that time-scale of the problem under study is of order of L_0/c or less. It is mentioned that the time scales are usually on the order of 10^{-9}~10^{-15} seconds in transient radiative heat transfer. The first term on the LHS of Eq. (3) is discretized using implicit backward differencing [12]. Control volume balance is then applied to each cell in the domain. For each discrete direction i Eq. (3) is integrated over the control volume $C0$ in Fig. 2 and the solid angle ω_i, in each new time step, to yield

$$\frac{I_{i0}^{n+1}-I_{i0}^{n}}{c\,\Delta t}+\frac{1}{\omega_i\,\Delta V_0}\sum_f J_f\,I_{if}^{n}=\left[-(\kappa+\sigma_s)I_{i0}^{n}+S_i\right] \quad (4)$$

To solve Eq. (4) numerically, at each new time step of $n+1$, iterations are made until the convergence of the source term values at all the points is achieved, using the values of time step n as the initial guess values for intensities. In this equation, I_{if}^{n} is the intensity associated with the control direction i at the face of the control volume, and I_{i0}^{n} is the intensity at the cell $C0$ in the direction i. I_{i0}^{n+1} is the intensity at the cell $C0$ in the new time step. ΔV_0 is the volume of the control volume $C0$. The solid angle ω_i is given by

$$\omega_i = \int_{\Delta\phi}\int_{\Delta\theta} \sin\theta \, d\theta \, d\phi = 2\sin\theta_i \sin\left(\frac{\Delta\theta}{2}\right)\Delta\phi \qquad (5)$$

The source term S_i is given by

$$S_i = \kappa I_{b0} + \frac{\sigma_s}{4\pi}\sum_j I_{j0}\left(\frac{1}{\omega_i}\int_{\omega_i}\int_{\omega_j} \Phi\left(\mathrm{s}_{i'} \bullet \mathrm{s}_{j'}\right) d\omega_{j'} \, d\omega_{i'}\right) \qquad (6)$$

The blackbody intensity I_{b0} is based on the temperature of the cell $C0$ and I_{j0} are the cell intensities in the directions j. J_f is a geometric factor which is defined in the following. For direction i with no control angle overhang at the face f, the following treatment is used

$$J_f I_{if} = I_{if} \, \hat{\mathrm{A}} \bullet \int_{\Delta\phi}\int_{\Delta\theta} \hat{\mathrm{s}} \, \sin\theta \, d\theta \, d\phi \qquad (7)$$

Here

$$\hat{\mathrm{s}} = \sin\theta\sin\phi \, \hat{\mathrm{i}} + \sin\theta\cos\phi \, \hat{\mathrm{j}} + \cos\theta \, \hat{\mathrm{k}} \qquad (8)$$

Computing the integral in Eq. (7) we get

$$J_f I_{if} = I_{if} \, \hat{\mathrm{A}} \bullet \hat{\mathrm{S}}_i \qquad (9)$$

The vector $\hat{\mathrm{A}}$ is the outward-pointing vector with respect to cell $C0$, as shown in Fig. 2. $\hat{\mathrm{S}}_i$ is given by

$$\begin{aligned} \hat{\mathrm{S}}_i = & \left[\Delta\theta - \cos(2\theta_i)\sin(\Delta\theta)\right] \\ & \left[\sin(\phi_i)\sin\left(\frac{\Delta\phi}{2}\right)\hat{\mathrm{i}} + \cos(\phi_i)\sin\left(\frac{\Delta\phi}{2}\right)\hat{\mathrm{j}}\right] \\ & + 0.5\sin(2\theta_i)\sin(\Delta\theta)\hat{\mathrm{k}} \end{aligned} \qquad (10)$$

There are different approaches to determine the intensity I_{if} on a given face based on the values of intensities in the centers of cells connected to that face. To relate the boundary intensities to the nodal intensities, spatial differencing schemes are needed. One common scheme is the modified-exponential scheme [18]. This approach can lead to physically incorrect negative nodal intensity. Another alternative, which is used here, is the step approximation. This approach guarantees that intensity values are always positive. Using a step approximation for I_{if} we may write

$$I_{if} = I_{i,\text{upwind}} \qquad (11)$$

Here $I_{i,\text{upwind}}$ is the value of I_i in the "upwind" cell.

For body-fitted and unstructured meshes, the discretization of TRTE is complicated by the possibility of control angle overhangs. Because the directions s_i are defined with respect to a global coordinate system (x, y, z), the boundaries of the discrete solid angles ω_i do not necessarily align with control volume faces. Mathematically, a control angle i is an overhanging control angle if $\hat{\mathrm{S}}_{ij} \bullet \hat{\mathrm{A}}$ $(j = 1,4)$ are not all of the same sign. Here, $\hat{\mathrm{S}}_{ij}$ is the ray vector to the jth corner of the ith control angle (each control angle has four corners). This illustrated in two dimensions in Fig. 3.

In three dimensions, the intersection of the control volume with the angular discretization is more complex. The line of intersection between the control volume face and the sphere is a great circle; the arbitrary intersections the discrete solid angle and this great circle determine the amount of overhang. This problem does not occur in Cartesian orthogonal meshes. It may also be avoided in structured body-fitted meshes by using local coordinates. Different approaches have been used to solve the steady radiative transfer equation on a directional grid with overhang control angles [19-21]. Technically, those approaches could be employed to overcome this issue for solving TRTE. An approach toward treatment of overhanging control angles was presented by Chui and Raithby [19], which treats control angle overhang at boundaries for two dimensions; however, it does not address it at interior faces. Their treatment requires the definition of neighbor directions that are fully incoming or fully outgoing. This is workable in two dimensions, but such directions cannot uniquely be identified for general three-dimensional overhangs. In three-dimensional cases, two approaches have been used commonly toward overhang control angles: The bold approach, and the pixelation approach.

The bold approach proposed by Chai et al. [20] treats overhanging control angle by assuming that the entire control angle is either incoming or outgoing. The control angle is purely incoming, if its larger section is incoming and to assume it is purely outgoing otherwise. This approach is numerically inexpensive, but inaccurate, especially when the overhang control angle is divided into two portions with close sizes.

The other common approach is called pixelation [21]. In this approach, if the direction i exhibits overhang at the face f, the incoming and outgoing portions of the solid angle are differenced differently. Equation (9) is written as

$$J_f I_{if} = I_{if,\text{out}} \, \alpha_{i,\text{out}} + I_{if,\text{in}} \, \alpha_{i,\text{in}} \qquad (12)$$

where

$$\alpha_{i,\text{out}} = \mathrm{A} \bullet \int_{\Delta\phi}\int_{\Delta\theta} \mathrm{s} \sin\theta \, d\theta \, d\phi, \quad \text{when } \mathrm{s} \bullet \mathrm{A} > 0 \qquad (13)$$

$$\alpha_{i,\text{in}} = \text{A}\bullet \int_{\Delta\phi}\int_{\Delta\theta} \text{s}\sin\theta\, d\theta\, d\phi, \quad \text{when s}\bullet\text{A} \le 0 \qquad (14)$$

The overhanging solid angle is divided into $N_{\theta_P} \times N_{\phi_P}$ pixels. Each pixel is identified by a pixel direction s_{Pi} written in terms of the pixel centroid angles (θ_{Pi}, ϕ_{Pi}) as

$$\text{s}_{Pi} = \sin\theta_{Pi}\sin\phi_{Pi}\,\text{i} + \sin\theta_{Pi}\cos\phi_{Pi}\,\text{j} + \cos\theta_{Pi}\,\text{k} \qquad (15)$$

We may then write Eqs. (13) and (14) as

$$\alpha_{i,\text{out}} = \text{A}\bullet \sum_{\text{s}\bullet\text{A}>0} S_{Pi} \qquad (16)$$

$$\alpha_{i,\text{in}} = \text{A}\bullet \sum_{\text{s}\bullet\text{A}\le 0} S_{Pi} \qquad (17)$$

where S_{Pi} is written analogously to Eq. (10), using the pixel angles (θ_{Pi}, ϕ_{Pi}) rather than (θ_i, ϕ_i). The summation is over all pixels in the control angle. Using the pixelation approach, control angle overhang can be computed up to the pixel resolution. The pixelation is computationally expensive.

The most accurate approach is the accurate angular discretization approach, which is the approach used in this work. In this approach, each overhanging control angles is divided into only two new control angles by using the related spatial grid cell face in a way that one of these new control angle is completely incoming solid angle and the other one is completely outgoing solid angle. Using the accurate angular discretization approach, control angle overhang can be computed up to the machine zero. Also, this approach is computationally less expensive than the pixelation approach. If there are $N_{overhang}$ overhanging control angles in a domain, $N_{overhang} \times N_{\theta_P} \times N_{\phi_P}$ computations is needed the pixelation approach. However, the accurate angular discretization approach only needs $2 \times N_{overhang}$ computations regarding the treatment of overhanging control angles.

RESULTS AND DISCUSSION

The presented method for solving TRTE has been applied to some different three-dimensional test cases. The first case studied here is a verification case, which is a steady-state radiative heat transfer problem. The results of the TRTE solver presented here are compared to the results of RTE solver in presented [7] as well as the exact solution. This case was studied by Kim and Huh [22]; and is simulation of radiation in a three-dimensional domain and involves a black enclosure with participating medium. A cubical enclosure with side length L_0 is considered (Fig. 4, top). It has black walls at a temperature of 0 K. The temperature profile in the enclosure is given by

$$T_{(x,y,z)} = h\left(\frac{1}{L_0}\sqrt{2\left((y-0.5L_0)^2 + (z-0.5L_0)^2\right)}\right) \times aT_0\, h\left(\frac{x-0.5L_0}{0.5L_0}\right) + (1-a)T_0 \qquad (18)$$

where function h is given by

$$h(p) = 1 - p^2 \qquad (19)$$

The reference temperature, T_0, represents the peak temperature in the enclosure. The parameter, a, is for the steepness or non-uniformity of the temperature profile. Kim and Huh discretized the enclosure into 25×25×25 control volumes and used an $N_\theta = 8$ by $N_\varphi = 12$ angular grid, where θ is the polar direction and φ is the azimuthal angle [22]. In the present simulation, a 15×15×15 spatial grid with $N_\theta = 8$ and $N_\varphi = 12$ is used. For a equal to 0.5, and κL_0 equal to 0.1 and 10, the radiative heat flux along the centerline on the boundary face is predicted; where κ is the absorption coefficient. Figure 5 compares the predicted solution by TRTE solver to the exact solution and the solution obtained by RTE [7], when $\kappa L_0 = 0.1$ for two perpendicular walls: wall at $y = 0$ and wall at $z = L_0$. The heat flux value in this figure is nondimensionalized with σT_0^4; where σ is the Stefan-Boltzmann constant ($5.67\text{x}10^{-8}$ $\text{W/m}^2\text{K}^4$). The obtained results are symmetric, as expected. The difference between the predicted solution by TRTE solver and RTE solver and the exact solution is hardly distinguishable. The TRTE solver, however, is computationally slightly more expensive, compared to the RTE solver. Figure 6 (top) shows the numerical prediction for the heat flux on wall at $z = L_0$, when κL_0 is set to 10. The results from RTE solver show higher heat flux compared to the exact solution; it overestimates the heat flux by about 9.4%. The TRTE solver underestimates the heat flux by about 2.6%. Therefore, it is seen that when the medium is optically thick, TRTE solver shows some advantages compared to the RTE solver. It is mentioned that if a finer mesh of 25×25×25 is used (which includes 5 times more cells, compared to the first mesh), then both approaches can predict the heat flux accurately, as it is shown in Fig. 6 (bottom). It is seen that the present method can produce better results, when the mesh is coarse and the medium is optically thick, compared to the steady RTE code. However, both methods converge to the exact solution, when a finer mesh is employed.

The second verification case studied here is from Ref. [10]. This case is a cubic enclosure with one hot wall (Fig. 4, bottom). Initially, the medium is assumed to be at a temperature of 0 K and initial intensities everywhere in the medium are zero. At $t = 0$, the intensity at the hot wall is set to $I_0 = 1$. The intensity is independent of direction. The other walls are kept at 0 K and assumed to be black. Tan and Hsu used a 17×17×17 spatial computational grid and used constant time steps, each

time step equal to the length of the computational cell divided by the speed of light. The value of the scattering albedo $\sigma_s/(\sigma_s+\kappa)$ was set to 0.1, while the optical thickness was assumed to be nonhomogenous as shown in below [10].

$$\kappa L_0 = \begin{cases} 1, & 0.00 < z/L_0 \le 0.35 \\ 5, & 0.35 < z/L_0 \le 0.65 \\ 1, & 0.65 < z/L_0 \le 1.00 \end{cases} \tag{20}$$

where, L_0 is the cube length, which is unit; and z is the axial direction normal to the hot wall, which is positioned at $z = 0$. In the present simulation, a 17×17×17 spatial grid with $N_\theta = N_\varphi = 12$ is used. Figure 7 compares the results obtained by the present method to the results of Ref. [10]. The physical time for the presented results is equal to $49L_0/16c$. As can be seen, the results predicted by the present FVM TRTE solver is in very good agreement with the results given in [10]; the maximum difference between the results of is less than 5%.

CONCLUSION

A numerical method compatible with CFD solvers was presented to predict transient radiative heat transfer using finite volume method on a generalized grid that can treat the overhang control angles accurately with minimal computational cost. It was shown that the method can accurately, predicts radiative flux in steady and transient problems with optically homogenous and nonhomogenous media.

REFERENCES

1. Hottel, H. C., and Cohen, E. S., 1958, "Radiant heat exchange in a gas-filled enclosure: Allowance for nonuniformity of gas temperature", AIChE Journal, 4, pp. 3-14.
2. Howell, J. R., and Perlmutter, M., 1964, "Monte Carlo solution of thermal transfer through radiant media between gray walls", Journal of Heat Transfer, 86, pp. 116-122.
3. Jeans, J. H., 1917, "The equations of radiative transfer of energy", Monthly Notices of the Royal Astronomical Society, 78, pp. 28-36.
4. Fiveland, W. A., 1984, "Discrete-Ordinates solutions of the radiation transport equation for rectangular enclosures", Journal of Heat Transfer, 106, pp. 699-706.
5. Raithby, G. D., and Chui, E. H., 1990, "A finite-volume method for predicting a radiant heat transfer in enclosures with participating media", Journal of Heat Transfer, 112, pp. 415-423.
6. Raithby, G. D., 1999, "Discussion of the finite-volume method for radiation, and its application using 3D unstructured meshes", Numerical Heat Transfer, Part B, Vol. 35, pp. 389-405.
7. Rahmani, R. K., Koomullil, R. P., Cheng, G., and Ayasoufi, A., 2006, "Finite volume method for non-equilibrium radiative heat transfer using generalized grid", AIAA Paper-2006-3782, 9th AIAA/ASME Joint Thermophysics and Heat Transfer Conference, San Francisco, CA.
8. Katika, K. M., and Pilon, L., 2006, "Modified method of charateristics in transient radiation transfer", Journal of Quantitative Spectroscopy & Radiative Transfer, 98, pp. 220-237.
9. An, W., Ruan, L. M., Tan, H. P., Qi, H., and Lew, Y. M., 2007, "Finite element simulation for short pulse light radiative transfer in homogeneous and nonhomogeneous media", Journal of Heat Transfer, 129, pp. 353-362.
10. Tan, Z. M., and Hsu, P. F., 2002, "Transient radiative transfer in three-dimensional homogeneous and non-homogeneous participating media", Journal of Quantitative Spectroscopy & Radiative Transfer, 73, pp. 181-194.
11. Liu, L. H., and Tan, H. P., 2001, "Transient radiation and conduction in a two-dimensional participating cylinder subjected to a pulse irradiation", International Journal of Thermal Science, 40, pp. 877-889.
12. Mishra, S. C., Chugh, P., Kumar, P., and Mitra, K., 2006, "Development and comparison of the DTM, the DOM and the FVM formulations for the short-pulse laser transport through a participating medium", International Journal of Heat and Mass Transfer, 49, pp. 1820-1832.
13. Hassan, T., Naqvi, K. R., El-Wakil, S. A., and Abulwafa, E. M., 2003, "Transient radiative heat transfer through thin films using Laguerre–Galerkin method", Journal of Physics D: Applied Physics, 36, pp. 3014-3026.
14. Liu, L. H., and Hsu, P. F., 2008, "Time shift and superposition method for solving transient radiative transfer equation", Journal of Quantitative Spectroscopy & Radiative Transfer, 109, pp. 1297-1308.
15. Ayranci, I., and Selcuk, N., 2004 "MOL solution of DOM for transient radiative transfer in 3-D scattering media", Journal of Quantitative Spectroscopy & Radiative Transfer, 84, pp. 409-422.
16. Liu, L. H., and Hsu, P. F., 2007, "Analysis of transient radiative transfer in semitransparent graded index medium", Journal of Quantitative Spectroscopy & Radiative Transfer, 105, pp. 357-376.
17. Chai, J. C., 2003, "One-dimensional transient radiation heat transfer modeling using a finite volume method", Numerical Heat Transfer, Part B, 44, pp. 187-208.
18. Chai, J. C., Lee, H. S., and Patankar, S. V., 1994, "Finite volume method for radiation heat transfer", Journal of Thermophysics and Heat Transfer, 8, pp. 419-425.
19. Chui, E. H., and Raithby, G. D., 1993, "Computation of radiant heat transfer on a non-orthogonal mesh using the finite-volume method", Numerical Heat Transfer, 23, part B, pp. 269-288.
20. Chai, J., Parthasarathy, G., Patankar, S., and Lee, H., 1994, "A finite-volume radiation heat transfer procedure for irregular geometries", AIAA Paper 94-2095.
21. Murthy, J. Y., and Mathur, S. R., 1998, "Finite volume method for the radiative heat transfer using unstructured

meshes", Journal of Thermophysics and Heat Transfer, 12, pp. 313-321.

22. Kim, S. H., and Huh, K. Y., 1999, "Assessment of the finite-volume method and the discrete ordinate method for radiative heat transfer in a three-dimensional rectangular enclosure", Numerical Heat Transfer, Part B, 35, pp. 85-112.

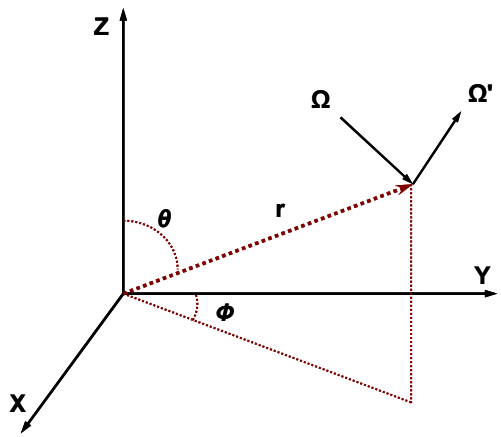

Figure 1: Incoming and outgoing radiant beams

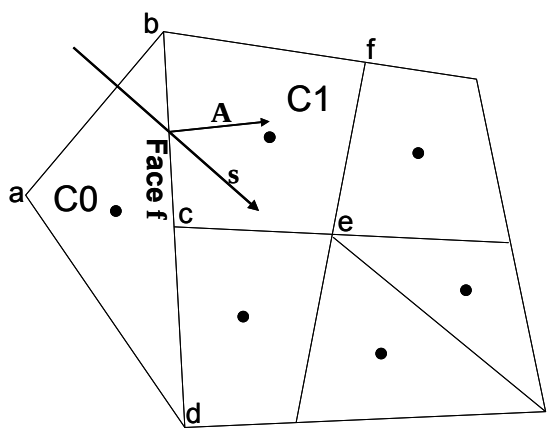

Figure 2: Control volume (Generalized grid)

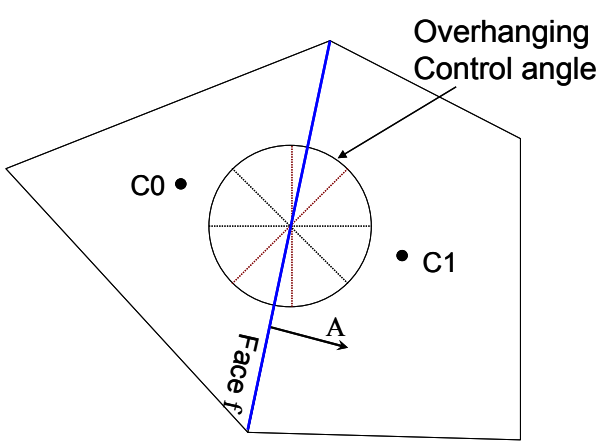

Figure 3: Control angle overhanging (2D spatial grid)

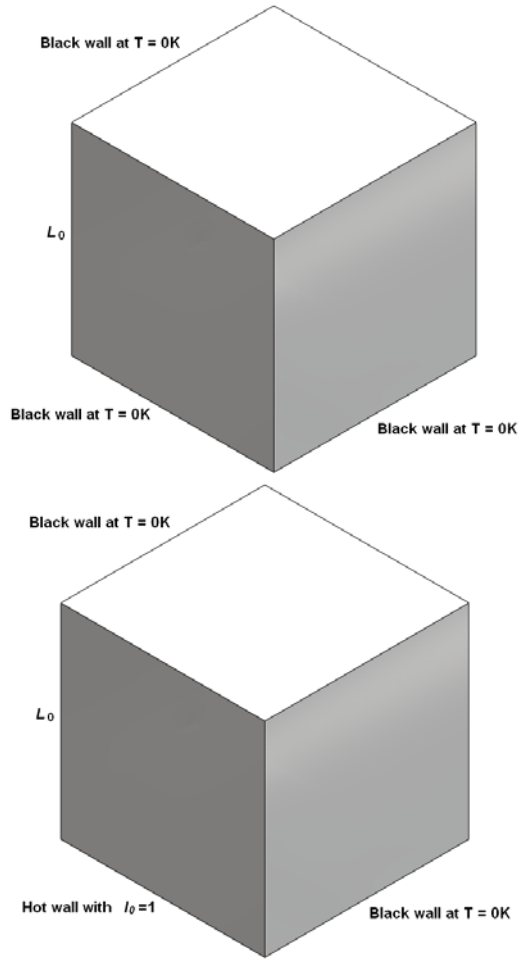

Figure 4: First and second studied cases

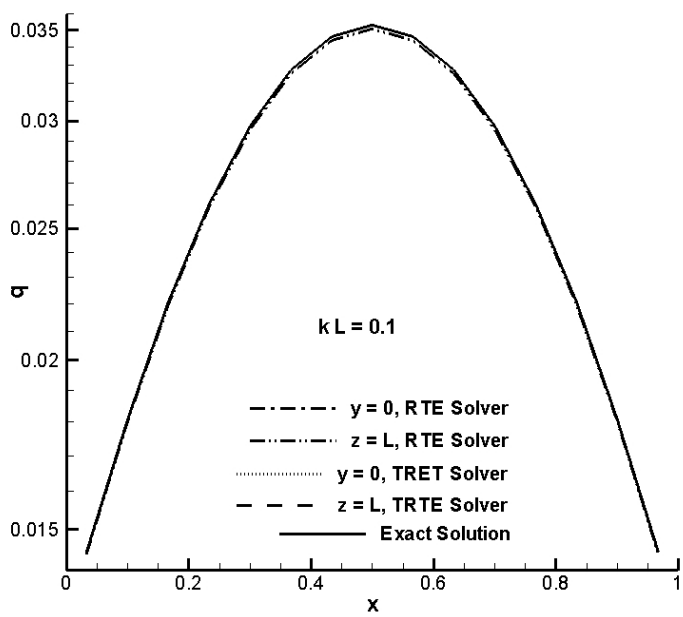

Figure 5: Comparison of TRTE to RTE and exact solution for a black body enclosure steady problem with κL_0 = 0.1

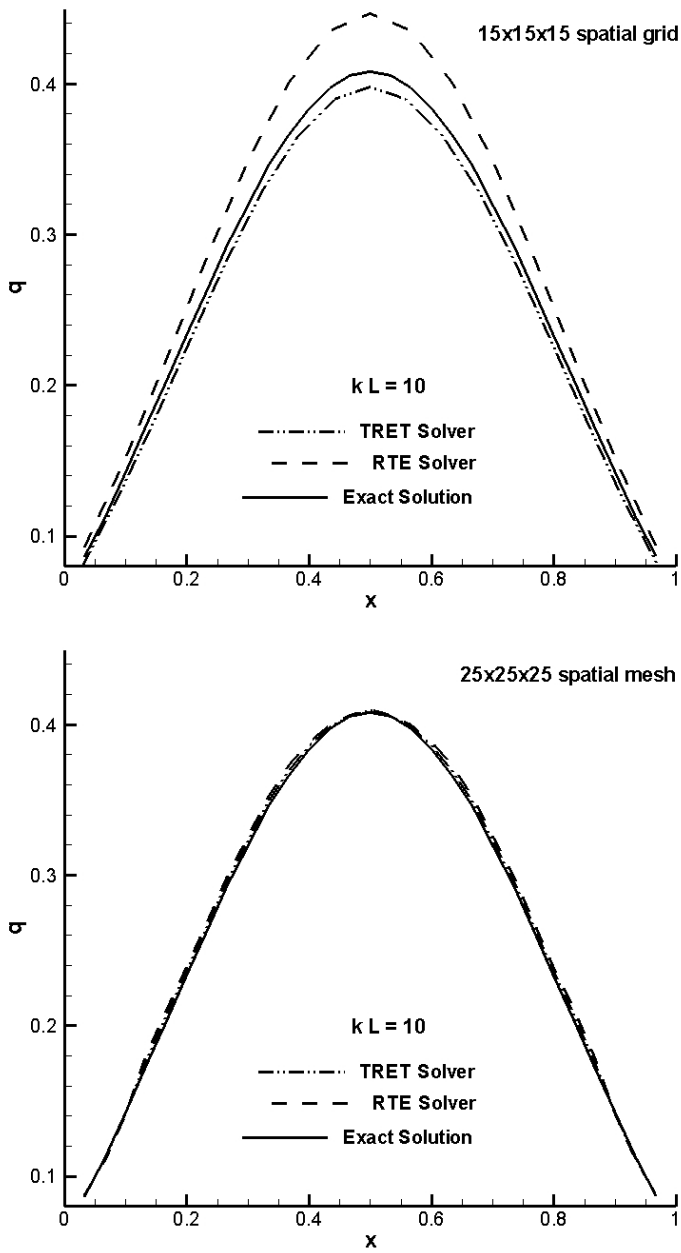

Figure 6: Comparison of TRTE to RTE and exact solution for a black body enclosure steady problem with $\kappa L_0 = 10$

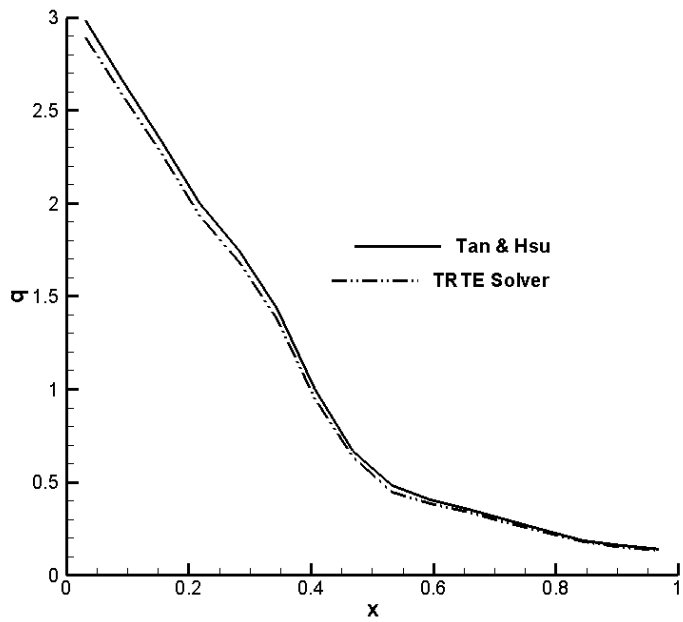

Figure 7: Radiative heat flux along the center line of a nonhomogenous cubic medium at $t = 49\ \Delta t$

ASME Early Career Technical Journal
2009 ASME Early Career Technical Conference, ASME ECTC
October 2-3, 2009, Tuscaloosa, Alabama, USA

AN ANALYTIC METHOD TO DETERMINE THE COMPRESSIVE CHARACTERISTIC LENGTH OF COMPOSITE JOINTS

O. Aluko
Department of Computer Science, Engineering and Physics
University of Michigan-Flint
Flint, Michigan, USA

ABSTRACT

Accurate prediction of joint strength in laminated composites has been an important research topic and the search to provide solutions to joint problems has remained a driving force for researchers. Among the methods utilized for prediction of composite joint strength, the characteristic length method has been known to be the most promising. An analytical method to determine the compressive characteristic length in different orthotropic materials is developed for the failure analysis of composite joint.

The analysis involves the specification of displacement expressions that were used to obtain the stress functions required to compute the stresses. The evaluated bearing strength for the plate based on the obtained characteristic length is validated by the experimental results in the literature. Good agreement was found between the analytical method and the test. The generality of the model makes it of practical importance to the researchers of composite joints and structures.

INTRODUCTION

Accurate determination of load bearing capacity of composite structures is very important; most especially when the region subjected to compressive loading is highly localized on either the surface or within the structures. This type of loading condition is most commonly encountered in mechanically fastened composite joints that are often utilized where structures are required to be assembled and disassembled for accessibility and maintenance. Owing to the difficult task of meeting the strength requirements of composite joint, as a result of low bearing strength of fiber reinforced composite materials, the analytical determination of bolted joint strength has attracted the attention of many researchers [1-10].

Adequate design of mechanically fastened composite joints requires the determination of the stress distribution at the pin-plate contact surface and within the plate, determining the failure load, and the failure mode. It is worth noting that even though the stresses around the mechanically fastened hole could be accurately determined, the failure at a point within the stress concentration regions do not necessarily lead to mechanical failure of the joint. The failure load of a joint would always be underestimated if a point failure within the stress concentration region is taken to be the ultimate failure of the joint. Hence, it constitutes a serious challenge to develop analytical method that can accurately evaluate the complicated failure and structural behavior of composite joint.

However, one of the most common and efficient methods of predicting the strength is the characteristic length method. This method was proposed by Whiney and Nuismer [5, 6], and it has been further developed by Chang et al. [7]. For this method, both the characteristic lengths in tension, R_t, and compression, R_c, must be determined by stress analysis associated with the results of bearing and tensile tests on notched and unnotched plates before employing an appropriate failure theory along the characteristic curve, r_c as shown in Figure 1. By definition, the characteristic length (in tension or compression) is the radial distance from the hole boundary over which the plate must be critically stressed to initiate a sufficient flaw that can cause failure.

Additionally, under practical conditions, mechanically fastened joints are designed to fail in bearing mode; therefore it is important to mention that characteristic length in tension is not a critical factor on the strength of practical joint. Based on this fact, the objective of this study is to develop an analytic method that can be used to determine the compressive characteristic length for joint strength analysis since it remains the critical factor controlling

the failure load of mechanical joints with bearing mode.

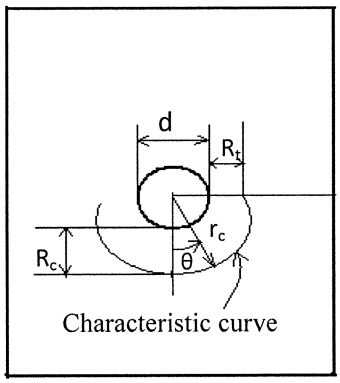

Figure 1. Schematic diagram for characteristic curve

Furthermore, this analytical method employs two approaches; one with bearing test and the other without bearing test. Also, the analysis entails the determination of stress distributions within the plate and at the pin-plate interface. In order to demonstrate the practical application of compressive characteristic length, Whitney-Nuismer's Point Stress Criterion [5] and the Yamada Failure Criterion [8] are used to predict the compressive failure of the plate.

STRESS ANALYSES

The present study utilized an analytical technique that accommodates a plate of any arbitrary thickness to determine stress distribution both within the plate and at the pin-plate contact surface. The composite bearing plate is considered to be homogeneous and semi-infinite with a semi-circular hole loaded by a rigid and frictionless pin which has the same diameter as the hole, as shown in Figure 2. The load P applied in the x-direction is assumed to cause a displacement of u_o in its own direction and u_o/c at points G_1 and G_2. The principal material directions are considered to coincide with the x- and y-axes. It is assumed that the pin load is resisted by distributed loading at infinity, and that the deformed plate is in a state of plane stress. The boundary conditions of this geometry can be expressed as

$$u = u_o \text{ and } v = 0 \qquad \theta = 0 \tag{1}$$

$$u = {}^{u_0}/_{c} \text{ and } v = 0 \qquad \theta = {}^{\pi}/_{2}, {}^{3\pi}/_{2} \tag{2}$$

$$(u_o - u)\cos\theta = v\sin\theta \quad {}^{3\pi}/_{2} \le \theta \le {}^{\pi}/_{2} \tag{3}$$

where u and v are the displacements along x and y axes respectively. Angle θ is defined from x-axis in counterclockwise direction along the pin-hole contact boundary and c is a constant to be determined.

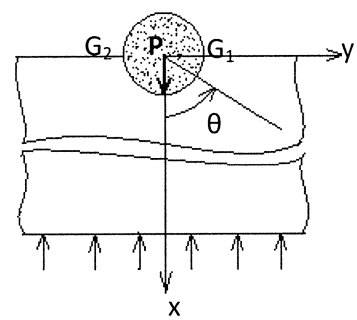

Figure 2. Schematic representation of compressive loading

Therefore, the displacements u and v that satisfy the above boundary conditions along the hole can be expressed by the following,

$$u_1\cos2\theta + u_2\cos4\theta \tag{4}$$

$$v_1\sin2\theta + v_2\sin4\theta \tag{5}$$

where u_1, u_2, v_1 and v_2 are the unknowns to be determined from boundary conditions.

The boundary condition of the plate at the free surface, where x equals zero, is

$$\sigma_r = 0 \text{ and } \tau_{r\theta} = 0 \tag{6}$$

Similarly, the traction boundary condition at the hole boundary can be expressed as

$$\tau_{r\theta} = 0 \qquad \text{at } \theta = \pi/2 \tag{7}$$

$$\int_0^{\frac{\pi}{2}} \tau_{r\theta}\, r d\theta = -\eta \int_0^{\frac{\pi}{2}} \sigma_r\, r d\theta \tag{8}$$

where η is the friction coefficient for Coulomb friction. Substituting Equations 4 and 5 into Equations 1 through 3, we have

$$u_1 = {}^{(c-1)u_o}/_{2c}, u_2 = v_2 = {}^{(c+1)u_o}/_{2c} \text{ and } v_1 = {}^{(3c+1)u_o}/_{2c} \tag{9}$$

Lekhtnitskii [2] has shown that if the known boundary displacement at the contour of the opening can be expressed in the form

$$u^* = \alpha_0 + \sum_{m=1}^{\infty}\{\alpha_m \rho^m + \bar{\alpha}_m \rho^{-m}\} \quad (10a)$$

$$v^* = \beta_0 \sum_{m=1}^{\infty}\{\beta_m \rho^m + \bar{\beta}_m \rho^{-m}\} \quad (10b)$$

and the components of the resultant forces that cause the displacement are given, then the stress functions can be expressed by the following relations

$$\phi_1 = A\ln\varsigma_1 + \left[\bar{\alpha}_1 q_2 - \bar{\beta}_1 p_2 + \frac{1}{2}\omega(ibq_2 + ap_2)\right]\frac{1}{D\varsigma_1} + \frac{1}{D}\sum_{m=2}^{\infty}\{\bar{\alpha}_m q_2 - \bar{\beta}_m p_2\}\,\varsigma_1{}^{-m} \quad (11a)$$

$$\phi_2 = B\ln\varsigma_2 - \left[\bar{\alpha}_1 q_1 - \bar{\beta}_1 p_1 + \frac{1}{2}\omega(ibq_1 + ap_1)\right]\frac{1}{D\varsigma_2} - \frac{1}{D}\sum_{m=2}^{\infty}\{\bar{\alpha}_m q_1 - \bar{\beta}_m p_1\}\,\varsigma_2{}^{-m} \quad (11b)$$

where $\rho = e^{i\theta}$ and, α_m and β_m are known coefficients that depend on the load distribution at the opening edge, α_0 and β_0 are arbitrary constants, and bars represent conjugate values. In this analysis, $\omega = 0$ since there is no rotation of the plate.

By expressing trigonometric functions in Equations 4 and 5 in terms of ρ defined by

$$\cos n\theta = \frac{\rho^n + \rho^{-n}}{2};\ \sin n\theta = \frac{\rho^n - \rho^{-n}}{2i} \quad (12)$$

and utilizing the above concept from Lekhtnitskii [2] yields the stress functions

$$\emptyset_1(z_1) = A\ln\varsigma_1 + \left({}^{1}/_{2D}\right)[(u_1 q_2 - iv_1 p_2)\varsigma_1^{-2} + (u_2 q_2 - iv_2 p_2)\,\varsigma_1^{-4}] \quad (13a)$$

$$\emptyset_2(z_2) = B\ln\varsigma_2 - \left({}^{1}/_{2D}\right)[(u_1 q_1 - iv_1 p_1)\varsigma_2^{-2} - (u_2 q_1 - iv_2 p_1)\,\varsigma_2^{-4}] \quad (13b)$$

Additionally, the external forces, X_x and Y_y at the boundary and displacement components can be expressed in term of stress functions as

$$\int_0^s Y_y\, ds = 2\mathrm{Re}\sum_{k=1,2}\emptyset_k(z_k), -\int_0^s X_x\, ds = 2\mathrm{Re}\sum_{k=1,2}\mu_k\emptyset_k(z_k) \quad (14)$$

$$u = 2\mathrm{Re}\sum_{k=1,2} p_k\emptyset_k(z_k),$$
$$v = 2\mathrm{Re}\sum_{k=1,2} q_k\emptyset_k(z_k) \quad (15)$$

By imposing both single-valued displacement conditions and satisfying the requirements for resultant load at the hole boundary, one obtains

$$A + B - \bar{A} - \bar{B} = 0$$

$$\mu_1 A + \mu_2 \mathrm{B} - \bar{\mu}_1\bar{A} - \bar{\mu}_2\bar{B} = -\frac{P}{\pi hi}$$

$$\mu_1{}^2 A + \mu_2{}^2 \mathrm{B} - \bar{\mu}_1{}^2\bar{A} - \bar{\mu}_2{}^2\bar{B} = 0 \quad (16)$$

$$\frac{1}{\mu_1}A + \frac{1}{\mu_2}\mathrm{B} - \frac{1}{\bar{\mu}_1}\bar{A} - \frac{1}{\bar{\mu}_2}\bar{B} = \frac{a_{12}}{a_{22}}\frac{P}{\pi hi}$$

It should be noted that coefficients A and B are determined by solving the above equations. These coefficients are given by the formulas

$$A = \left({}^{P}/_{\pi hi}\right)\left(\mu_1\bar{\mu}_1 + \mu_1\mu_2 + \mu_1\bar{\mu}_2 - \left({}^{a_{12}}/_{a_{22}}\right)\mu_1\mu_2\bar{\mu}_1\bar{\mu}_2\right)/\left((\mu_1 - \bar{\mu}_1)(\mu_1 - \mu_2)(\mu_1 - \bar{\mu}_2)\right) \quad (17a)$$

$$B = \left({}^{P}/_{\pi hi}\right)\left(\mu_2\bar{\mu}_2 + \mu_1\mu_2 + \mu_2\bar{\mu}_1 - \left({}^{a_{12}}/_{a_{22}}\right)\mu_1\mu_2\bar{\mu}_1\bar{\mu}_2\right)/\left((\mu_2 - \bar{\mu}_2)(\mu_2 - \mu_1)(\mu_2 - \bar{\mu}_1)\right) \quad (17b)$$

where the bar implies conjugate and

$$D = a_{11}(\mu_1 - \mu_2)g \quad (18)$$

$$p_1 = a_{11}\mu_1{}^2 + a_{12} \text{ and } p_2 = a_{11}\mu_2{}^2 + a_{12} \quad (19a)$$

$$q_1 = a_{12}\mu_1 + {}^{a_{22}}/_{\mu_1} \text{ and } q_2 = a_{12}\mu_2 + {}^{a_{22}}/_{\mu_2} \quad (19b)$$

$$\varsigma_k = \left(z_k \pm \sqrt{z_k^2 - \mu_k r^2 - r^2}\right)/(r - i\mu_k r);$$

$$z_k = x + \mu_k y \quad k = 1,2 \quad (20)$$

with a_{ij} $(i,j = 1,2,6)$ being the compliances, and μ_1 and μ_2 the roots of the characteristic equation for orthotropic plate defined by

$$a_{11}\mu^4 + (2a_{12} + a_{66})\mu^2 + a_{22} = 0 \quad (21)$$

where 1 and 2 are parallel and transverse to the loading direction respectively, and r is the radius of the hole.

The stresses in polar co-ordinates are given by the expressions

$$\sigma_r = 2\mathrm{Re}\{(\sin\theta - \mu_1\cos\theta)^2\emptyset_1'(z_1) + (\sin\theta - \mu_2\cos\theta)^2\emptyset_2'(z_2)\} \quad (22a)$$

$$\tau_{r\theta} = 2\mathrm{Re}\{(\sin\theta - \mu_1\cos\theta)(\cos\theta + \mu_1\sin\theta)\emptyset_1'(z_1) + (\sin\theta - \mu_2\cos\theta)(\cos\theta + \mu_2\sin\theta)\emptyset_2'(z_2)\} \quad (22b)$$

$$\sigma_\theta = 2\mathrm{Re}\{(\mu_1\sin\theta + \cos\theta)^2\emptyset_1'(z_1) + (\mu_2\sin\theta + \cos\theta)^2\emptyset_2'(z_2)\} \quad (22c)$$

The prime implies the derivative of the stress functions with respect to z.
The radial stress σ_r and shear stress $\tau_{r\theta}$ expressions in Equation 22 at the hole boundary can be written as

$$\sigma_r = \{((c+1)/cgr)u_o\}\{n(1-k)\cos5\theta\} + (u_o/cgr)[(c+1)(3v_{12} - 3k - kn) + ((c-1)/2)\,n(1-k)]\cos3\theta - [P/\pi rh + ((c-1)u_o/2cgr)(2k - 2v_{12} + nk + n) + ((c+1)u_o/cgr)(k - v_{12} + n)]\cos\theta \quad (23)$$

$$\tau_{r\theta} = -\{((c+1)/cgr)u_o\}\{n(1-k)\sin5\theta\} - (u_o/cgr)[(c+1)(k - v_{12} + kn + 2n) + ((c-1)/2)\,n(1-k)]\cos3\theta + [P/\pi rh - ((c-1)u_o/2cgr)(2k - 2v_{12} + nk + n) - ((c+1)u_o/cgr)(k - v_{12} + n)]\sin\theta \quad (24)$$

where the parameters k, n and g are material constants of the plate expressed as

$$n = -i(\mu_1 + \mu_2) = [2(k - v_{12}) + E_1/G_{12}]^{1/2} \quad (25a)$$

$$k = -\mu_1\mu_2 = (E_1/E_2)^{1/2} \quad (25b)$$

$$g = (1 - v_{12}v_{21})/E_2 + k/G_{12} \quad (25c)$$

Solving Equations 7 and 8 simultaneously for η=0, using Equations 23 and 24, one obtains the displacement u_0 and constant c expressed as

$$c = C_1/C_2 \quad (26)$$

where

$$C_1 = -10k - 9n - 21kn + 10v_{12}$$

$$C_2 = 10k + 19n + 11kn - 10v_{12}$$

and

$$u_o = A_1/\big(h\pi(A_2 + A_3)\big) \quad (27)$$

where

$$A_1 = \big(gP(10k + 9n + 21kn - 10v_{12})\big)$$

$$A_2 = 20k^2 + 28kn + 52k^2n + 48kn^2$$

$$A_3 = 12k^2n^2 - 40kv_{12} - 28nv_{12} - 52knv_{12} + 20{v_{12}}^2$$

The unknown coefficients u_i and v_i can be determined from Equations 9, 26 and 27 and have the results substituted into Equation 22 to yield the values of the normal, shear and hoop stresses. The preceding analysis provides a direct solution to the stress distribution within the loaded composite plate for different orthotropic materials once the parameters n and k that characterized the orthotropy of the plate are known. Hence, this analytical model can be used as template to compute the compressive characteristic length of orthotropic plate of any arbitrary thickness.

Additionally, the stresses in Equation 22 can be transformed into rectangular co-ordinate to obtain

$$\sigma_x = 2\mathrm{Re}\{{\mu_1}^2\emptyset_1'(z_1) + ({\mu_2}^2\emptyset_2'(z_2)\} \quad (28a)$$

$$\tau_{xy} = -2\mathrm{Re}\{(\mu_1\emptyset_1'(z_1) + \mu_2\emptyset_2'(z_2)\} \quad (28b)$$

$$\sigma_y = 2\mathrm{Re}\{\emptyset_1'(z_1) + \emptyset_2'(z_2)\} \quad (28c)$$

COMPRESSIVE CHRACTERISTIC LENGTH

As stated earlier, the characteristic length method of predicting joint strength is one of the most promising and efficient methods [5-7]. Two approaches are employed in this study for the determination of compressive characteristic length. The first approach involved the bearing test to failure since bearing failure load must be known a priori. Within the context of this method, the compressive characteristic length R_c, as showed in Figure 3, for point stress criterion [5] is the distance from the front of hole boundary to a point at which the normal stress is equal to bearing strength. The bearing strength can be expressed as

$$\sigma_b = {}^{P}/_{dh} \quad (29)$$

The second approach introduced by Kweon et al. [10] is without the bearing test. This method utilizes any arbitrary load to compute the mean bearing stress, defined by

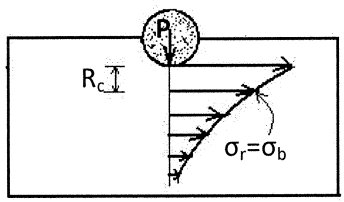

Figure 3. Schematic diagram of the compressive characteristic length and normal stress distribution pattern

$$\sigma_{mb} = {}^{P_m}/_{dh} \tag{30}$$

where, P_m, d and h are the arbitrary loads, diameter of hole and laminate thickness respectively. Based on this method, the compressive characteristic length is redefined as the distance from the front hole-edge to a point where the local compressive stress by the arbitrarily applied load is the same as the mean bearing stress.

In this study, the plate (MO1) made from carbon-epoxy unidirectional prepreg (USN125) and plain weave prepreg (HPW193) [9] with stacking sequence $[\pm45_3/90/\pm45_2/0_4/90/0_4//\pm45_2/90/\pm45_3]$ was used. The notation "±45" is used to represent a plain weave carbon/epoxy layer and the lamina thicknesses of the unidirectional and woven fabric layers are 0.125 mm and 0.19 mm, respectively. The hole diameter (d) is 9.53 mm, the width (W) of the plate is 26.8 mm, and the edge distance (e) is 19 mm. Also, MO2 composite plate [10] having the same stacking sequence as above was utilized. The unidirectional layers are from the USN125 graphite/epoxy prepreg by Hankook Fiber Glass. The DMS2288 graphite/epoxy woven fabrics are by Sunkyong. The one-ply-thicknesses of the unidirectional and woven fabric layers are 0.114 mm and 0.198 mm, respectively. Other geometries of these two plates are the same. Additionally, AS4/3501-6 graphite/epoxy laminate, having the stacking sequence $[(45/0/-45/0/90/0/45/0/-45/0)_2]_s$ with geometry of diameter (d), thickness (h), ratio of end distance to hole diameter (e/d) equal to 0.635 cm, 0.584 cm and 2, respectively, was also used in this analysis [3] for method without bearing test. The material properties of the three laminates are as given in Table 1.

Utilizing the Bearing Test Method, the compressive failure load P, obtained from experiment [9,10], was used to determine the characteristic length in compression. However, for the No-bearing Test Method, the arbitrary loads and the corresponding mean bearing stresses used to determine the compressive characteristic length are shown in Tables 2 and 3. In both approaches, the normal stress distribution in Equation 22a was numerically evaluated by a symbolic computer code written in Mathematica. As mentioned before the Point Stress Criterion, introduced by Whitney and Nuismer [5], was used to evaluate the compressive characteristic length.

Table 1. The material properties of composite materials

Properties	Type of Material			
	USN 125	HPW 193	DMS 2288	AS43501-6
E_1 (GPa)	131	65.4	65	144.14
E_2 (GPa)	8.2	65.4	65	11.72
G_{12} (GPa)	4.5	3.59	3.6	6.69
υ_{12}	0.281	0.058	0.058	0.33
X_c (MPa)	1400	692.9	692.9	1480
S_{12} (MPa)	70	64.9	65	60

Table 2. The applied arbitrary load and mean bearing stress for MO1 plate

Loads (P_m)		Mean bearing stress (σ_{mb})	
Symbols	Value KN	Symbols	Values MPa
P_{m1}	5.0	σ_{mb1}	162.232
P_{m2}	7.0	σ_{mb2}	227.125
P_{m3}	10.0	σ_{mb3}	324.464
P	12.1	σ_b	392.600

FAILURE ANALYSES

The practical application of the compressive characteristic length was demonstrated by utilizing the stress values, obtained from the present analytical method at the computed characteristic length in compression from the hole boundary, to predict the compressive strength of loaded plates. The Yamada-Sun failure criterion was used in this analysis as a test condition for first ply failure at any point along the

compressive characteristic curve as shown in Figure 4. This curve can be expressed as

$$r_c = r + R_c \tag{31}$$

Table 3. The applied arbitrary load and mean bearing stress for $[(45/0/-45/0/90/0/45/0/-45/0)_2]_s$

Loads (P_m)		Mean bearing stress (σ_{mb})	
Symbols	Value KN	Symbols	Values MPa
P_{m1}	15.0	σ_{mb1}	404.996
P_{m2}	20.0	σ_{mb2}	539.995
P_{m3}	25.0	σ_{mb3}	674.993
P_{m4}	29.8	σ_{mb4}	805.00

and the criterion is given by the expression [8]

$$(\sigma_1/X_c)^2 + (\tau_{12}/S)^2 = e^2 \tag{32}$$

where σ_1 and τ_{12} are longitudinal compressive and shear stresses, X_c the ply longitudinal compressive strength and S the ply shear strength. In this model, failure is expected to occur when the value of e is either equal to or greater than unity. Additionally, the notched strength for a finite plate can be obtained from the notched strength determined for an infinite plate as

$$Y\sigma_N^{\infty} = \sigma_N \tag{33}$$

where, σ_N and $\sigma_N{}^{\infty}$ denote the notched strength for finite and infinite plate, respectively. Y is the Finite-width Correction Factor developed by Tan [1] and it can be expressed as

$$Y = \frac{\left[2-\left(\frac{2r}{W}\right)^2-\left(\frac{2r}{W}\right)^4\right]}{2} + \frac{\left(\frac{2r}{W}\right)^6 (K_T^{\infty}-3)\left[1-\left(\frac{2r}{W}\right)\right]}{2} \tag{34}$$

where

$$K_T^{\infty} = 1 + \sqrt{\frac{2}{A_{66}}\left(\sqrt{A_{11}A_{22}}-A_{12} + \frac{A_{11}A_{22}-A_{12}^2}{2A_{66}}\right)} \tag{35}$$

and A_{ij}, i,j = 1,2,6 denote the effective laminate in-plane stiffnesses, and W is the plate's width. The computer code used to evaluate the failure load was written in Mathematica.

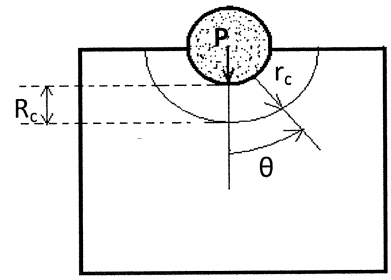

Figure 4. A schematic description of the compressive characteristic length and curve

RESULTS AND DISCUSSION

In utilizing the Bearing Test Method, the compressive failure load P of magnitude 12.1 kN obtained from the previous work of Choi and Chun [9], was used to evaluate carbon-epoxy plate (MO1) with the properties and geometries as previously mentioned. The bearing strength of the plate is 392.6 MPa. Figure 5 shows the normal stress distributions from hole edge due to bearing failure load. As can be seen from this figure, based on the Point Stress Criterion, a compressive characteristic length of 1.32 mm was obtained. Choi and Chun [9] used the Finite Element Method to determine the compressive characteristic length for this plate and obtained 1.158 mm. The normal stress distribution in this study and that of Choi et al. [9] showed a good agreement except in the vicinity of hole where the stress concentration factor is different. Apart from the fact that the finite element method for analyzing stresses

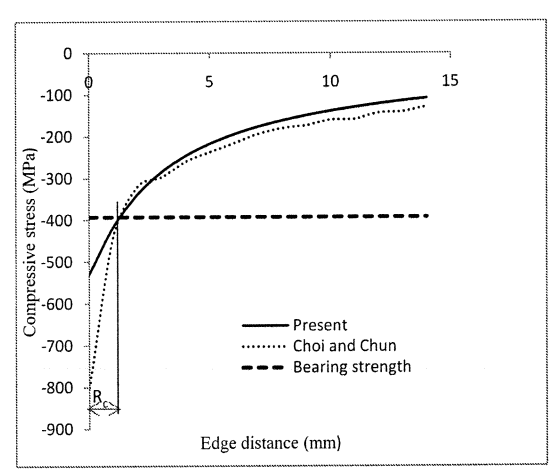

Figure 5. Compressive characteristic length with bearing test for MO1 plate

is generally an approximation of the analytical solution, Choi et al. [9] also did not explain how they specified the boundary conditions, and these may probably account for this difference in the stress value within the vicinity of the hole boundary.

For the case of No-bearing Test Method, Figure 6 showed all the arbitrary compressive loads used and their corresponding normal stress distributions in the direction of compression. Based on the definition of characteristic length for this approach, it is shown on this figure that, regardless of the arbitrary loads used to determine the normal stress distribution, the obtained value of compressive characteristic length remains unchanged and is also equal to 1.32 mm. The computed characteristic length is in close agreement with the result from [9] in both methods, and this establishes the validity of the present analytical method.

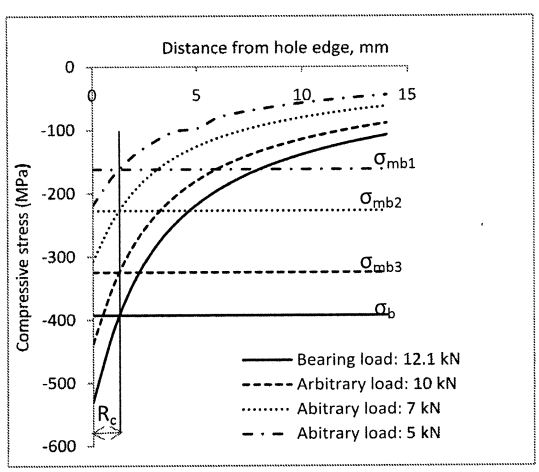

Figure 6. Compressive characteristic length without bearing test for MO1 plate

Additionally, in order to demonstrate the applicability of the compressive characteristic length, the computed characteristic length in compression was used in conjunction with the Yamada-Sun failure criterion to evaluate failure load of the bearing plate and the result compared with the experimentally obtained failure load from the previous work of Choi and Chun [9]. Figure 7, shows the reasonable agreement between the analytical and the experimental value. The analytic failure load is 3 % higher than experimental result. This difference can be caused by the assumption that the plate is homogeneous and the uncertainties involved in measuring the experimental value.

Furthermore, the validity of this analytical model was demonstrated by using the No-bearing Test Method, to evaluate the compressive characteristic length of graphite/epoxy plate of AS4/3501-6 laminate. Figure 8 equally showed all the arbitrary compressive loads used and their corresponding normal stress distributions from the hole edge in the direction of compression. As shown in this figure, the characteristic length, which is the distance from the front hole-edge to a point where the local compressive stress by the arbitrarily applied load is the same as the mean bearing stress, is 1.2949 mm. Since there was no available experimental data for this plate in order to obtain the characteristic length using the bearing test approach, Whitworth et al. [3], in their analysis used available experimental data for AS4/3501-5 laminate to evaluate the

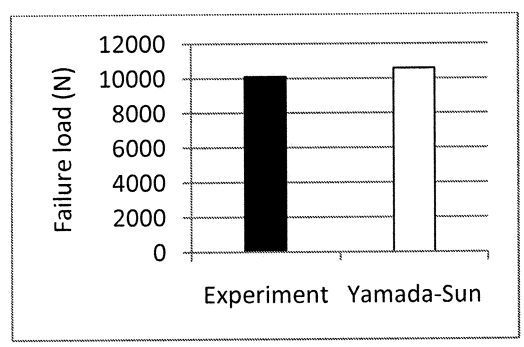

Figure 7. Bearing failure load of composite plate (MO1)

compressive characteristic length for AS4/3501-6, based on the fact that they both have similar properties, for which they obtained 1.3 mm. Again, the excellent agreement between these two results further proved the validity of the present analytical method for determining the compressive characteristic length. Also, the evaluated bearing strength for this plate, based on the computed value of compressive characteristic length is 382.7 MPa.

To further verify the application of compressive characteristic length to bearing strength of laminated plate, the analytically obtained characteristic length in compression, of 3.47 mm was used to compute the strength of composite plate MO2. Figure 9 shows the computed failure load as compared with the experimental value. It can be

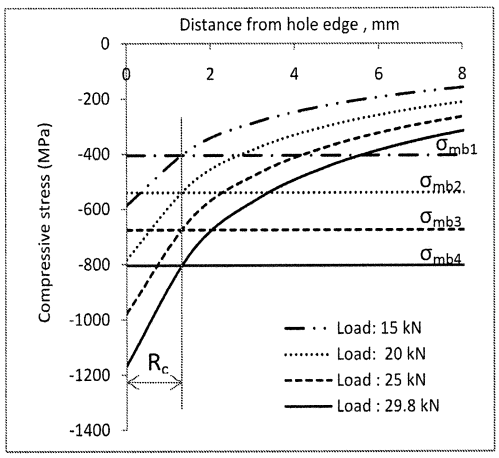

Figure 8. Compressive characteristic length without bearing test for $[(45/0/-45/0/90/0/45/0/-45/0)_2]_s$

seen from this figure that there is a reasonable agreement between the two values, which further proves that the present method for determining the characteristic length in compression is adequate. However, the prediction is within 4.6% accuracy of the experimental result. As stated earlier, the difference cannot be disconnected from the initial assumption that the material is homogeneous, the limitation from two-dimensional analysis, and the uncertainties that follow the experimental characterization of failure loads.

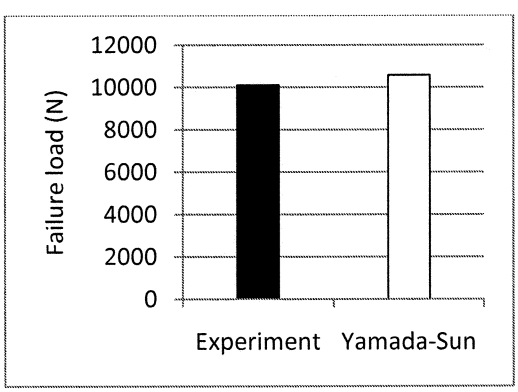

Figure 9. Bearing failure load of laminated composite plate (MO2)

CONCLUSION

An analytical method was proposed to evaluate the compressive characteristic length of different orthotropic materials. The two approaches used (bearing test and no bearing test) are equally effective to evaluate compressive characteristic length. The validity of the present analytical method was established by the excellent agreement between the computed values of characteristic length in both approaches and the available results in the literature. The practical application of the compressive characteristic length was demonstrated by the agreement between the computed bearing strength of the plate based on the analytically obtained compressive characteristic length and the experimental result. The simplicity and generality of the model make it of practical importance to the researchers in composite joints and structures.

REFERENCES

[1] Tan, S. C., 1988, "Finite-Width Correction Factors for Anisotropic Plate Containing a Central Opening," J. of Comp. Materials, 22, pp. 1080-1097.

[2] Lekhnitskii, S. G., 1968, "Anisotropic Plates", Translated from the 2nd Russian edition by Tsai, S.W. and Chevron,T., Gordon and Breach, London 1968.

[3] Whitworth, H. A., Othieno, M., and Barton, O., 2003, "Failure Analysis of Composite Pin Loaded Joints," Composite Structures, 59, pp. 261-266.

[4] Zhang, K., and Ueng, C. E. S., 1984, "Stress Around a Pin Loaded Hole in Orthotropic Plates," Journal of Composite Materials, 18, pp. 432-446.

[5] Whitney, J. M., and Nuismer, R. J., 1974, "Stress Fracture Criteria for Laminated Composites Containing stress Concentrations," Journal of Composite Materials, 8(253), pp. 253-265.

[6] Whitney, J. M., and Nuismer, R. J., 1975, "Uniaxial Failure of Composite Laminate Containing Stress Concentrations," Fracture Mechanics of Composite, ASTM STP, pp. 117-142.

[7] Chang, F. K., and Scott, R. A., 1982, "Strength of mechanically Fastened Composite joints," Journal of Composite Materials, 16, pp. 470-494.

[8] Nahas, M. N., 1986, "Survey of Failure and Post-Failure Theories of Laminated FR Composites," J. of Comp. Tech. and Research, 8(4), pp.138-153.

[9] Choi, J., and Chun, Y., 2003, "Failure Load Prediction of Mech. Fastened Composite Joints," J. of Composite Materials, 37(24), pp. 2163-2177.

[10] Kweon, J.,Ahn, H., and Choi J., 2004, "A new Method to determine the Charact. Lengths of Comp. Joints without Testing," Comp. Structures, 66, pp. 305-315.

ASME Early Career Technical Journal
2009 ASME Early Career Technical Conference, ASME ECTC
October 2-3, 2009, Tuscaloosa, Alabama, USA

SHOCK RESPONSE AND FINITE ELEMENT MODELING OF NANOCLAY AND GRAPHITE PLATELET REINFORCED VINYL ESTER NANOCOMPOSITES

Swasti Gupta, P. Raju Mantena
Mechanical Engineering, University of Mississippi
University, MS, USA

Ahmed Al-Ostaz, Christopher L. Mullen
Civil Engineering, University of Mississippi
University, MS, USA

ABSTRACT

The shock response of Derakane 411-350 vinyl ester thermoset beam specimens with 1.25 and 2.5 wt. percent randomly distributed exfoliated graphite nanoplatelets and Cloisite 30B nanoclay were investigated. Shock tube apparatus was used to study the material response at a peak pressure of 70 psi (482.6 kPa), and approximate strain rate of 1000 per second; and 120 psi (827.4 kPa), and approximate strain rate of 1400 per second. Shock tube experiments were also modeled using the explicit finite element program, ANSYS LS-DYNA.

The energy absorption improved by about 150 percent with increasing nano reinforcement, for shock tests conducted at 120 psi peak pressure. A close agreement was observed between experimental data and finite element modeling of the shock response.

INTRODUCTION

Nanocomposites are often touted as the material of the 21st century finding applications in almost all industries including automobiles, electronics, space, chemicals, sensors, storage systems, health care, and structural applications among others. These new class of composites are increasingly being studied for their application in structures such as spacecrafts, airplanes, warships etc. which requires high stiffness-to-weight ratio along with high damping. Nanoclay [1-4] and graphite platelets [5-9] are some of the nano scale inclusions proposed as filler materials showing promise for structural applications, and have been investigated in this work for naval ships and homeland security applications.

The objective of this work is to study the shock response of nanoclay/ vinyl ester; and graphite platelet/ vinyl ester nanocomposites with 1.25 and 2.5 wt. percent reinforcement in comparison with the pure polymer. These nanocomposites are planned to be used as face plates of sandwich composite structure with fire-resistant foam layered in between to further enhance the energy absorption along with optimal flexural rigidity, vibration, damping and reduced flammability. These new materials are being developed to make structures blast/shock/impact resistant with reduced weight for naval ships and homeland security applications.

SHOCK TESTS

A simple shock tube consists of two halves isolated from each other by a diaphragm with high gas pressure on the driver side of the shock tube [10-11]. Diaphragm is controlled to burst at the required pressure difference which develops a shock wave. This shock wave propagates into the test section (low pressure or driven section) of the tube. At the same time, an expansion wave develops and propagates in the driver side of the tube. If a test specimen is kept in the driven section (low pressure region) of the shock tube, the specimen undergoes this shock which simulates the rush of gas after an explosion. The shock tube test facility at University of Rhode Island was utilized in the current study.

Shock tube tests were conducted on plates of dimension 254 mm x 101.6 mm x 9.9 mm (10” x 4” x .39”). One panel from each configuration was subjected to 70 psi (482.3 kPa) and another at 120 psi (827.4 kPa) peak pressure. It is to be noted that pure vinyl ester specimen was first shock loaded with 70 psi (482.3 kPa) peak pressure and then with 120 psi (827.4 kPa) peak pressure. It was reported that samples subjected to 70 psi (482.3 kPa) peak pressure did not fracture. However, post-test samples received show hairline fractures for 1.25 and 2.5 wt percent graphite platelet samples subjected to 70 psi peak pressure. All the samples subjected to 120 psi (827.4 kPa) peak pressure fragmented into pieces.

The nanocomposite panels were held under simply supported conditions so as to minimize damage due to gripping and clamping. The span of the simply supported plate was 152 mm (6”) and the overhangs measured 50.8 mm (2”) along each end. The center of the specimen was kept in line with the center of the shock tube. The ratio of the loading diameter to the span was 0.5. The specimens were blast loaded from the exit of the shock tube on the face opposite to the supports [11].

Dynamic pressure sensor (PCB Piezotronics A123) mounted near the exit of the shock wave measures the shock pressure and reflected pressure history. Shock velocities are measured using break circuits and adequate calibration data is also available for the same. The shock wave velocities for the experiments conducted in this study were 500 m/s for a peak pressure of 70 psi (482.3 kPa) and 600 m/s with a peak pressure of about 120 psi (827.4 kPa). Images of the specimens loaded by the shock wave were captured in real time intervals of 100-150 microseconds [11] by using a high-speed IMACON 2000 camera.

Strain Rate Approximation

For viscoelastic materials, the rate of loading is an important characteristic since energy absorbed before failure may vary for different strain rates. Viscoelastic materials typically become stiff at high strain rates with a reduction in strength and vice versa. An approximation of the transient strain rate under shock tube testing has been obtained using the bending moment equation under quasi-static load conditions.

The quasi-static bending moment equation was used for computing the flexural stress (σ):

$$\sigma = \frac{M \cdot y}{I} \tag{1}$$

Transient bending strain, ε(t) as a function of the instantaneous transient load, is obtained from:

$$\varepsilon(t) = \frac{\sigma(t)}{E} \tag{2}$$

The transient bending moment, M(t), was computed from transient load, P(t) obtained from pressure profile curve at each time step, t by multiplying it with the effective area of the driven section (3" Diameter) as shown in Figure 1. The transient shock load in this test was applied on a circular region which was approximated as a rectangular zone along the beam width as shown in Figure 2.

Boundary conditions are approximated as a simply-supported beam. Substituting value of σ from Equation (1), to obtain the, ε at each time step, t.

$$\varepsilon(t) = \frac{M(t) \cdot y}{E \cdot I} \tag{3}$$

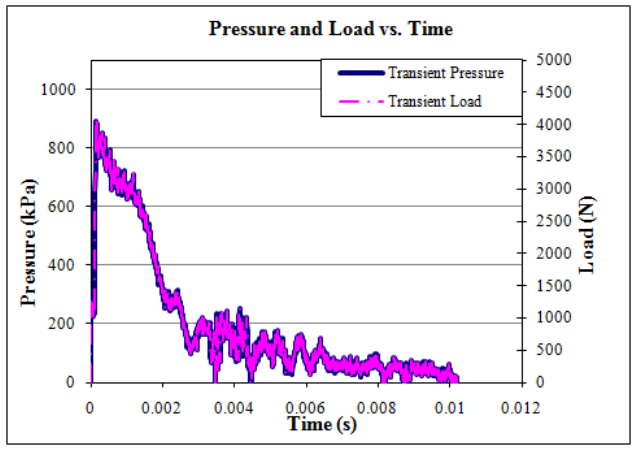

Figure 1. Pressure and load vs. time for pure vinyl ester specimen obtained from shock tube test

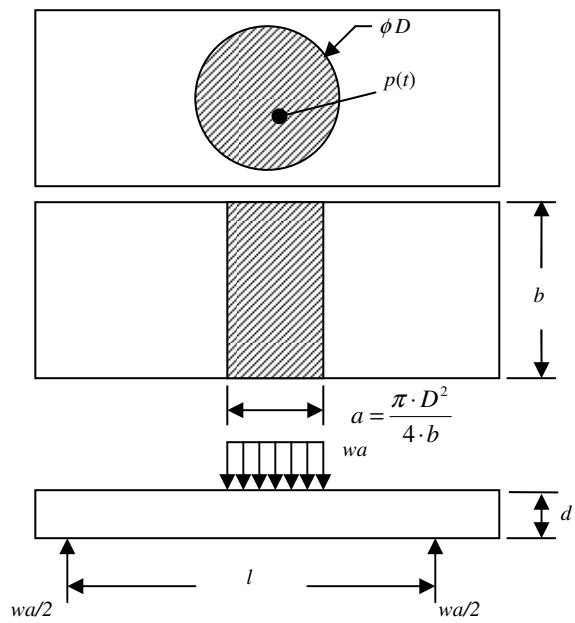

Figure 2. Boundary condition for Shock Test

Maximum bending moment at the center is given by:

$$M(t) = \frac{1}{8} wa \cdot (2l - a)$$

$$= \frac{1}{8}\left(p(t) \cdot b\right) \cdot \left(\frac{\pi \cdot D^2}{4b}\right) \cdot (2l - a)$$

$$M(t) = \frac{1}{8} p(t) \cdot (2l - a) \tag{4}$$

where $p(t)$ = Transient pressure
and $P(t)$ = Transient load

The area moment of inertia for rectangular beam specimen is given by:

$$I = \frac{b \cdot d^3}{12} \tag{5}$$

With the maximum flexural stress occurring at the outermost bottom layer of the specimen:

$$y = \frac{d}{2} \tag{6}$$

Substituting value of $M(t)$, I, and y from equation (4), (5), (6) respectively in equation (3) gives:

$$\varepsilon(t) = \frac{\frac{1}{8} P(t) \cdot (2l - a) \cdot \frac{d}{2}}{E \cdot \frac{bd^3}{12}} = \frac{3}{4}\left(\frac{P(t) \cdot (2l - a)}{E \cdot b \cdot d^2}\right) \tag{7}$$

or

$$\varepsilon(t) = K \cdot P(t) \tag{8}$$

where

$$K = \frac{3}{4}\left(\frac{(2l - a)}{E \cdot b \cdot d^2}\right) \tag{9}$$

K will be a constant based on the experimental set-up and type of material tested. The transient strain computed as a function of the transient load using equation (8) is plotted with time on the x-axis. A typical graph of transient strain versus time (and load versus time) for pure vinyl ester is shown in Figure 3.

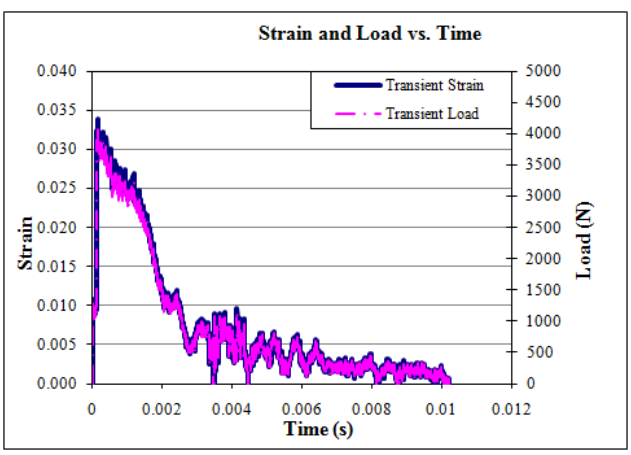

Figure 3. Strain and load vs. time for pure vinyl ester specimen obtained from shock tube test

Strain rate was then computed based on the initial slope. A typical graph for the slope of strain curve from shock tube for a peak pressure of 120 psi for pure vinyl ester is shown in Figure 4 with a linear fit line in the initial portion where maximum increase in pressure is observed. An approximate strain rate of 1000 per second and 1400 per second respectively for the 70 psi and 120 psi peak pressure was computed for the shock tube tests.

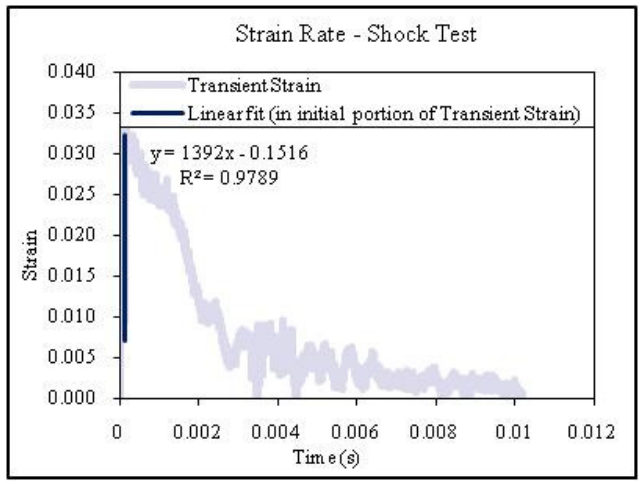

Figure 4. Strain rate for pure vinyl ester specimen for a shock tube test with a peak pressure of 120 psi

Analysis of Shock Tube Test Data

The pressure profile curve, real time images, post-test visual examination and deflection data of vinyl ester nanocomposites were reported by the University of Rhode Island [11]. No failure was reported in the vinyl ester specimens subjected to 70 psi peak pressure, while specimens subjected to 120 psi peak pressure were shattered in pieces.

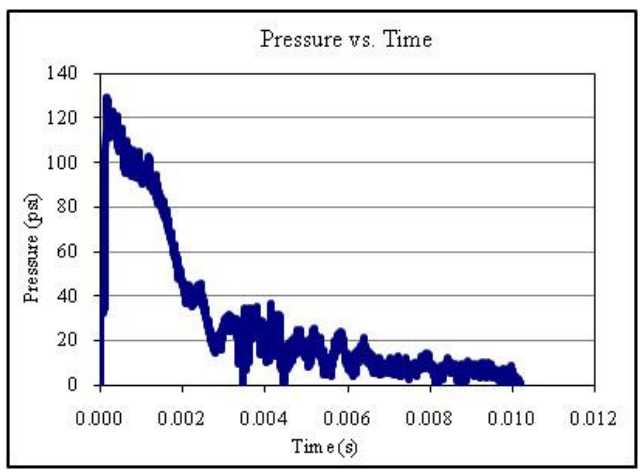

Figure 5. Pressure profile for pure vinyl ester subjected to 120 psi peak pressure [11]

The typical pressure profile curve, real time images and the post-test images for pure vinyl ester specimen subjected to 120 psi peak pressure is shown in Figures 5 to 7 and the response deflection versus time graph is shown in Figures 8 and 9. It is to be noted that in the case of pure vinyl ester, the same specimen was used for both 70 psi and 120 psi peak pressure.

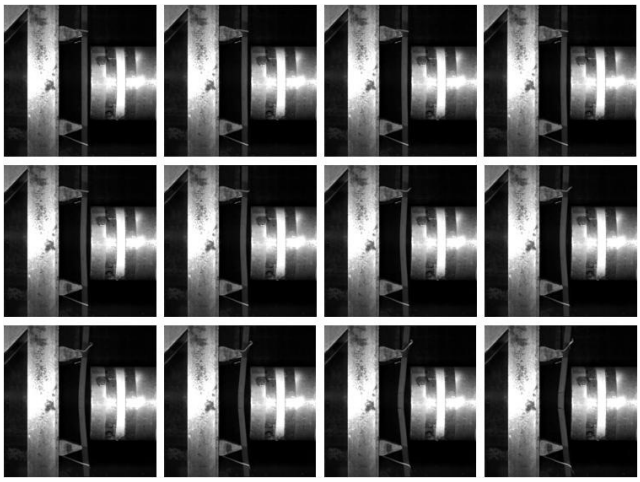

Figure 6. Real time image of 2.5% graphite platelet/vinyl ester subjected to 120 psi peak pressure in shock tube [11]

Figure 7. Post-test image of 2.5% graphite platelet/vinyl ester specimen subjected to 120 psi peak pressure in shock tube [11]

In order to analyze the material response to shock loading, quasi-static approach was adopted. In the quasi-static method, energy absorbed by each specimen is obtained by correlating the mid-span deflection with the pressure in terms of transient load. Pressure at respective time intervals was converted to transient load exerted on the specimen by multiplying it with the effective cross-sectional area of the driven section (3" Diameter). Transient load thus obtained was plotted against respective mid-span deflection. Energy absorbed was then computed with numerical integration up to the point of maximum deflection (failure). For this numerical integration, DPlot software [12] was used which employs trapezoidal rule to do the integration.

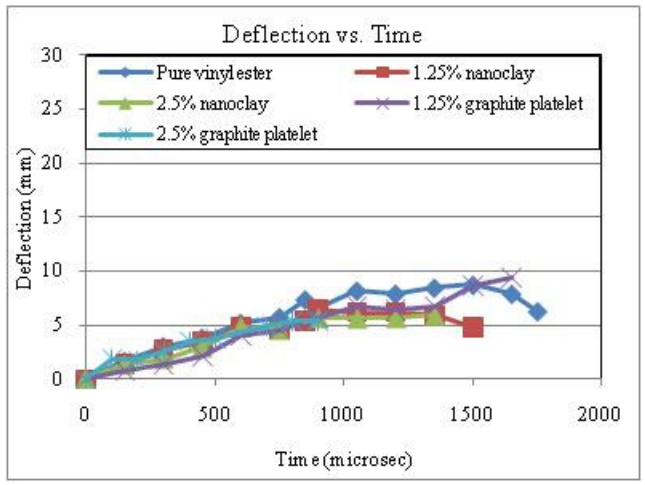

Figure 8. Mid-point deflection vs. time obtained from high speed images for vinyl ester panels with and without nano reinforcement at 70 psi peak pressure

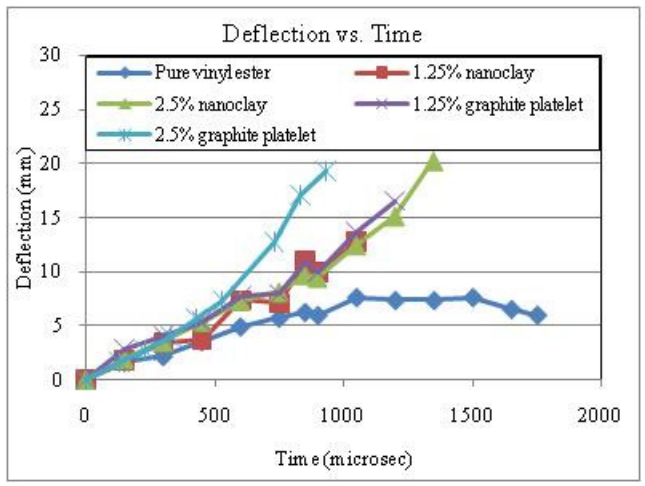

Figure 9. Mid-point deflection vs. time obtained from high speed images for vinyl ester panels with and without nano reinforcement at 120 psi peak pressure

Finite Element Analysis of Shock Tube Test

Finite element modeling using ANSYS LS-DYNA of vinyl ester nanocomposite beam specimens subjected to shock loading was attempted. ANSYS LS-DYNA has the advantage of having explicit finite element program which provides faster solutions for large deformation and multiple nonlinearities problems [13].

The material to be analyzed is approximated to be randomly distributed nanoparticles in an isotropic matrix and the structure is supposed to have large deformations and complex loading through the thickness. Solid 168, a higher order 3D, 10 node tetrahedral structural solid, explicit dynamic element was used for modeling. The element is defined by ten nodes each having three degree of freedom at each node for translation motion in x, y, and

z direction. No real constants need to be defined for this element as everything is defined in the material property.

Standard piecewise material model was used for defining the material properties. This model provides a multi-linear elastic-plastic material option that allows input of stress-strain curve at different strain rates and effective failure plastic strain can be defined for defining failure point [13]. This material model required true stress-true plastic strain curve, density, and effective failure plastic strain as input. Engineering stress-strain and failure strain was obtained from quasi-static test and was converted to true stress-true plastic strain for input in the material model [14]. It is to be noted that the quasi-static test were conducted on nanocomposites produced using brominated 510A-40 vinyl ester resin as opposed to the non-brominated Derakane 411-350 vinyl ester resin used for shock tube experiments. Density of non-brominated Derakane 411-350 vinyl ester resin nanocomposites was used in finite element modeling [14].

Model of the structure was created using appropriate key points exactly in the same way as in shock tube experimental setup. A dense meshing in the loading area and a coarse meshing in outer area was employed. A total of 51786 elements with 76596 nodes were created.

Proper restraints were then assigned to define the boundary condition to match the experimental set-up as shown in Figure 10. As the test specimen was simply supported at a span of 150 mm (6") with an overhang of 50 mm (2") at both ends, the respective lines in the model were restrained to move in z-direction. To avoid twisting of the specimen, node at the center of the specimen and center of the left support were restrained to move in x and y direction.

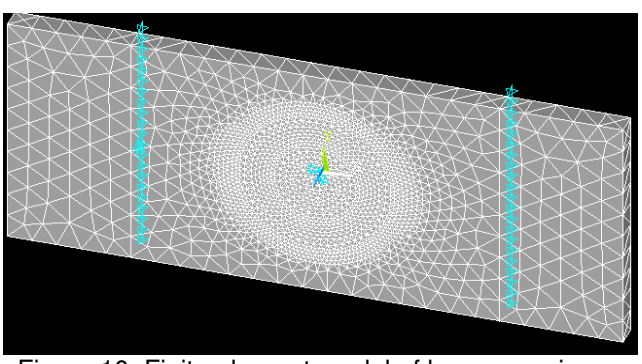

Figure 10. Finite element model of beam specimen for shock response characterization with boundary condition

Load applied in the experiments was by the shock coming out of a tubular section. This load was approximated to be equally distributed in the circular region of the same area. Due to the inherent problem with 3D Tet-Solid 168 element on applying uniformly distributed load [15], a nodal load was applied instead on all the nodes of the circular region. It was assumed that all the nodes are equidistant in the loading area. Load on the nodes on periphery of the circle (external nodes) was half in magnitude to that of load on nodes inside the circular region (internal nodes).

Solution was then obtained for transient analysis using explicit dynamics method. Time at the end of the load step was defined to be the time at which maximum deflection was observed in the experiments. Deformed view of the structure due to the applied load was captured and mid-point deflection was obtained to compare with the experimental results.

EXPERIMENTAL RESULTS

The energy absorbed by vinyl ester nanocomposites obtained from numerical integration of the load vs. mid-point deflection is tabulated in Table 1, and the trend shown in Figure 11. It is to be noted that specimens subjected to 70 psi peak pressure did not fail while all other specimens fragmented into pieces. Further, in case of pure vinyl ester the same specimen was used for both 70 psi as well as 120 psi peak pressure.

Table 1. Energy absorption for nanoclay and graphite platelet/ vinyl ester nanocomposites for peak pressure of 70 psi and 120 psi

Specimen	Energy absorption (J)	
	70 psi	120 psi
Pure vinyl ester	16.95	22.94
1.25% nanoclay/ VE	12.54	39.33
2.5% nanoclay/VE	11.34	45.50
1.25% graphite platelet/VE	19.43	45.53
2.5% graphite platelet/VE	9.58	62.81

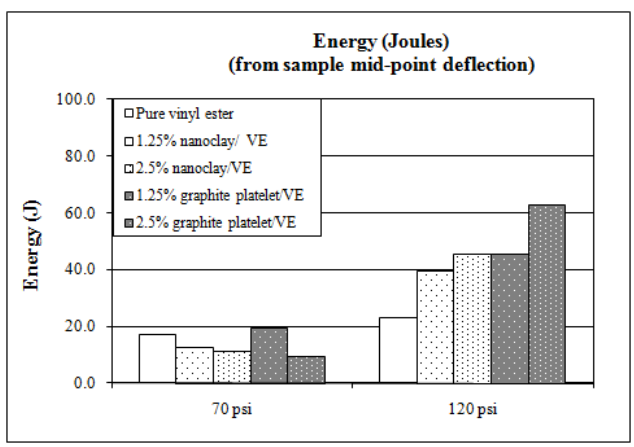

Figure 11. Energy absorption for nanoclay and graphite platelet/ vinyl ester nanocomposites for peak pressure of 70 psi and 120 psi

It was concluded that the energy absorption characteristics of vinyl ester specimens that did not fail when subjected to 70 psi peak pressure was not an appropriate measure of total energy absorption as high stiffness of material can lead to lower deflection which in turn may show lesser energy absorption. The trend of energy absorbed for the 120 psi peak pressure (where samples fragmented into pieces) is shown to be increasing with increasing reinforcement, with 2.5 wt. percent graphite platelet showing maximum improvement.

Figures 12 and 13 show the deformation of pure vinyl ester nanocomposites subjected to 70 psi and 120 psi peak pressure obtained from finite element modeling. Figures 14 and 15 show the deflection with respect to time obtained from finite element model and comparison with the experimental results.

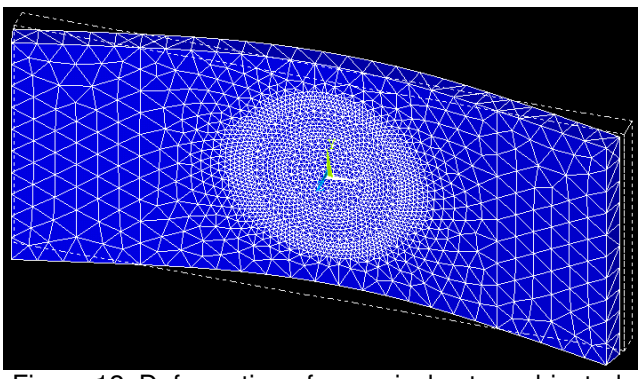

Figure 12. Deformation of pure vinyl ester subjected to 70 psi peak pressure from FEA

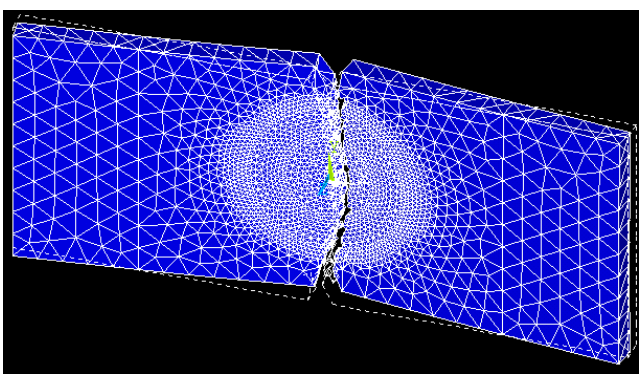

Figure 13. Deformation of pure vinyl ester subjected to 120 psi peak pressure from FEA

For 70 psi peak pressure experiments, it is observed that the FEA model of graphite platelet reinforcement showed failure occurring contrary to the experimental tests conducted and reported by University of Rhode Island [11]. The experimental deflections and those obtained from finite element model are observed to be close. Further, the post-test samples of graphite platelet received from University of Rhode Island did show some hairline fracture.

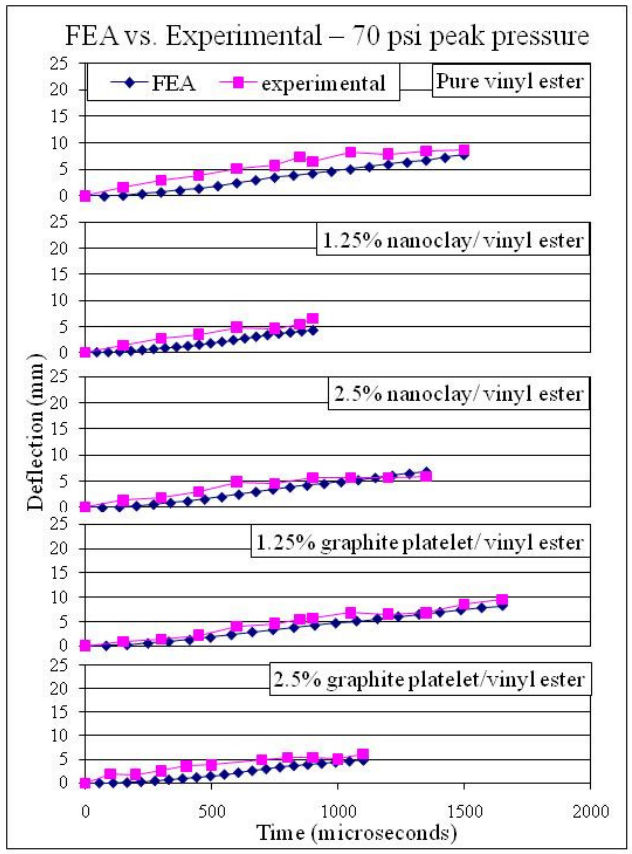

Figure 14. Deflection vs. time obtained from finite element model and shock tube experiments for nanoclay and graphite platelet/ vinyl ester subject to 70 psi peak pressure

For 120 psi peak pressure experiments, it is observed that the 2.5 wt. percent nanoclay reinforced vinyl ester does not show failure in the FEA model as opposed to the experimental tests conducted and reported by University of Rhode Island [11]. A larger variation between the experimental and finite element model deflections is observed for 2.5 wt. percent reinforcement of nanoclay and graphite platelet as shown in Figure 15. It is suspected that the pressure profile curve recorded for these cases are erroneous. It is also noted that brominated 510A-40 vinyl ester resin was used for defining the material model in finite element analysis instead of the non-brominated derakane 411-350 vinyl ester resin which was actually tested in shock tube. This might also be the reason for discrepancy as 2.5 wt. percent reinforcement of nanoclay and graphite platelet are showing inferior properties with brominated 510A-40 vinyl ester resin. Variation in

deflection of pure vinyl ester is also attributed to the reuse of same sample that was used for 70 psi peak pressure testing in the subsequent 120 psi peak pressure testing.

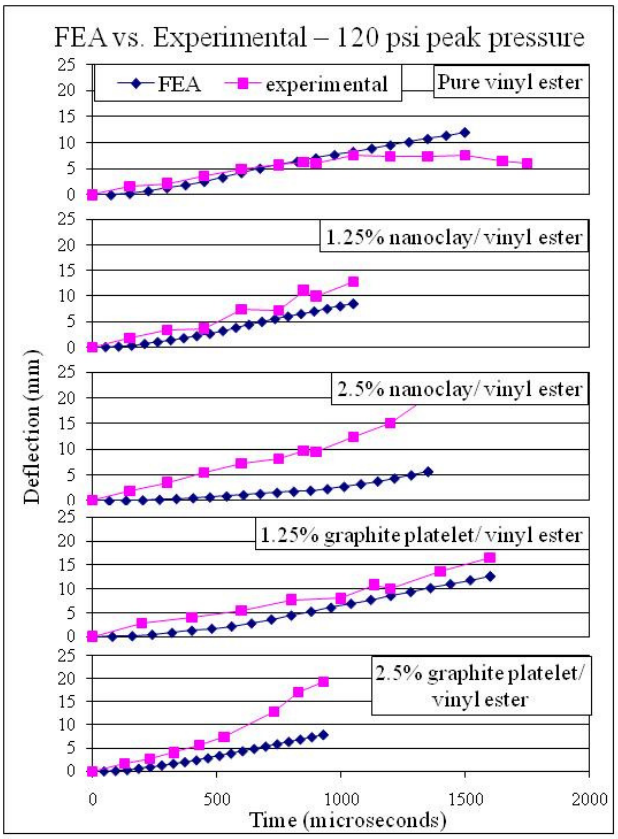

Figure 15. Deflection vs. time obtained from finite element model and shock tube experiments for nanoclay and graphite platelet/ vinyl ester subject to 120 psi peak pressure

CONCLUSION

Energy absorption under shock testing is shown to be increasing for nanoclay and graphite platelet reinforced vinyl ester nanocomposites tested at a strain rate of 1400 per second (120 psi peak pressure). Graphite platelet reinforced vinyl ester nanocomposites also showed very good improvement in material response under shock testing obtained using dynamic approach.

For most of the cases, a good agreement with experimental deflection-time obtained from shock tube tests and finite element model was observed. Discrepancies in the results are attributed to the brominated 510A-40 vinyl ester resin used to define the material model, instead of derakane 411-350 vinyl ester resin which was actually used in the specimens that were subjected to shock tube testing. Shock tube experiments on brominated 510A-40 vinyl ester resin nanocomposites are underway to resolve these discrepancies.

ACKNOWLEDGEMENT

The authors would like to acknowledge the support received from the Department of Civil Engineering at the University of Mississippi, and funding received under a subcontract from the Department of Homeland Security-sponsored Southeast Region Research Initiative (SERRI) at the Department of Energy's Oak Ridge National Laboratory. Partial support for this research by ONR Grant # N00014-07-1-1010, Office of Naval Research, Solid Mechanics Program (Dr. Yapa D.S. Rajapakse, Program Manager) is also acknowledged.

Authors would also like to acknowledge the support of Dr. Larry Drzal, Michigan State University for providing the nano samples, and Dr. Arun Shukla, University of Rhode Island for performing the shock tube tests.

REFERENCES

[1] Schmidt, D., Shah, D. and Giannelis, E.P., 2002, "New Advances in Polymer/Layered Silicate Nanocomposites", Current Opinion in Solid State and Materials Science, 6(3), pp. 205–212.

[2] Ray, S.S. and Okamoto, M. , 2003, "Polymer/layered Silicate Nanocomposite: A Review from Preparation to Processing", Prog. Polymer Sci., 28, pp. 1539–1641.

[3] Bhat G., Hegde1 R. R., Kamath M.G., and Deshpande B., 2008, "Nanoclay Reinforced Fibers and Nonwovens", Journal of Engineered Fibers and Fabrics, 3(3), pp. 22-34.

[4] Alexandre M., Dubois P., 2000, "Polymer-layered silicate nanocomposites: preparation, properties and uses of a new class of materials", Material Science and Engineering; 28, pp. 1-63.

[5] Shen, J.W., Chen, X.M. and Huang, W.Y., 2003, "Structure and Electrical Properties of Grafted Polypropylene/Graphite Nanocomposites Prepared by Solution Intercalation", Journal of Applied Polymer Science, 88, pp. 1864–1869.

[6] Yasmin, A., Luo, J. and Daniel, I.M., 2006, Processing of Expanded Graphite Reinforced Polymer Nanocomposites, Composites Science and Technology, 66(9), pp. 1182–1189.

[7] Asma Yasmin, Isaac Daniel., 2004, "Mechanical and thermal properties of graphite platelet/ epoxy composites," Polymer 45, 24, pp. 8211-8219.

[8] Peng Xiao, Min Xiao, Gong K., 2001, "Preparation of exfoliated graphite/ polystyrene composite by polymerization-filling technique" Polymer, 42, pp. 4813-4816.

[9] Fukushima H., and Drzal L.T, 2004, "Graphite nanoplatelets as reinforcement for polymers: structural and

electrical properties" Proc. 17th International Conference on American Society for composites, September 9-11, 2004.
[10] University of Rhode Island website, http://www.advance.uri.edu/pacer/october2004/story10.htm, accessed on December 13, 2007 at 13:00 hours.
[11] Arun Shukla, September 2007, "Shock Testing of Reinforced Vinyl Ester Materials", Internal report, Department of Mechanical Engineering, University of Mississippi, University, MS.
[12] DPlot Version 2.2.1.1, Copyright © 2001-2008 by Hydesoft Computing, LLC.
[13] ANSYS LS-DYNA User's Guide. ANSYS Release 10.0.002184 © SAP IP, Inc.
[14] Swasti Gupta., 2009, "Energy Absorption Characteristics of MWCNT/ Nylon 6,6; and Nanoclay and Graphite Platelet/ Vinyl Ester Nanocomposites," MS thesis, University of Mississippi, University, MS.
[15] E-mail communication between Dr. Ahmed Al-Ostaz and Mr. Bill Bulat for incident number 826775 dated November 12, 2008.